TECHNISCHE UNIVERSITÄT WIEN

Diploma Thesis

An Analytical Pressure and Flow Model for Leaf Seals

carried out for the purpose of obtaining the degree of
Master of Science (MSc or Dipl.-Ing. or DI)
submitted at Technische Universität Wien
Faculty of Mechanical and Industrial Engineering

by

Gregor Franz NICHT

Mat.Nr.: 0867982
Wolfenreith 4/2, 3122 Gansbach, Austria

under the supervision of

Ao.Univ.Prof. Dipl.-Ing. Dr.techn. Reinhard Willinger

Institute for Energy Systems and Thermodynamics

February, 2018

Affidavit

I declare in lieu and oath, that I wrote this thesis and performed the associated research myself, using only literature cited in this volume. If text passages from sources are used literally, they are marked as such.
I confirm that this work is original and has not been submitted elsewhere for any examination, nor is it currently under consideration for a thesis elsewhere.

Vienna, February 2018 Signature

Acknowledgements

At the beginning I have to thank *Ao.Univ.Prof. Dipl.-Ing. Dr.techn. Reinhard Willinger* for his excellent support during the writing of this thesis. He also made it possible, that parts of this thesis will be presented at the ASME Turbo Expo 2018 in Oslo, Norway. He always took time for answering questions and giving feedback, especially during the more strenuous times before submission deadlines for this conference.

I want to express great gratitude to my parents, *Maria Nicht* and *Franz Nicht*, who supported me unconditionally throughout my entire life and gave me the possibility to study in Vienna.

I also want to thank *Philip Swoboda* and *Maximilian Zechmeister* for their friendship, forged in our common study time of mechanical engineering at the Technische Universität Wien.

Abstract

Leafs seals are an advanced sealing technology to separate high and low pressure parts in turbomachinery, consisting of small metal sheet elements arranged in a housing around the shaft. During operation the seal should be non-contacting to minimize wear and friction. The static pressure on the surface of a single leaf appears to be the main parameter. The higher axial stiffness in comparison to brush seals allows greater differences in pressure and a hang-up effect can be averted. Assessing the discharge behavior of the sealing is important, because leakage is resulting in less efficient turbomachinery.

In this thesis a new approach for an analytical calculation of the pressure distribution inside the seal is presented. It is based on a leakage flow model inside the side plate gaps. Furthermore the flow is assumed to be laminar and incompressible using simple pipe flow correlations with specified hydraulic diameters. The complete seal geometry is parameterized. The results in pressure distribution, leakage flow and static pressure on a single leaf (Lift Up, Blow Down) are compared with data published in literature. A good qualitative match was found, so in a second step, variations of the seal design were calculated. The influence of upstream and downstream side plate gap width ratios, heights of rotor side plate gap, numbers of leaves for constant rotor diameter and interleaf gap width gradients are investigated. For validation of the model, the results are compared as far as possible to published data. Also calculations are made for patented designs using leaves with non-rectangular cross-section to estimate, if further and more detailed research is reasonable. The static pressure distribution derived is used for a deflection calculation of the leaves using Euler-Bernoulli beam theory.

The analytical model provides a simple approach for the investigation of leaf seals regarding pressure distribution and seal-leakage with qualitative good results.

KEYWORDS: leaf seal, internal air system, compliant plate seal

Kurzfassung

Lamellendichtungen sind eine fortschrittliche Dichtungsbauart für Turbomaschinen. Diese Dichtungen bestehen aus in Umfangsrichtung angeordneten Metallblättchen, welche in einem Gehäuse befestigt sind. Während des Betriebes soll die Dichtung berührungslos arbeiten damit weder Reibung noch Verschleiss auftritt. Die statische Druckverteilung an der Lamellenoberfläche hat darauf einen entscheidenden Einfluß. Die höhere Steifigkeit der Lamellen in axialer Richtung im Vergleich zu den Borsten von Bürstendichtungen ermöglicht den Einsatz bei größeren Druckdifferenzen. Zusätzlich kann der Hang-Up Effekt verhindert werden. Der Leckagemassenstrom sollte so gering wie möglich sein um eine Wirkungsgradeinbuße zu vermeiden.

In dieser Arbeit wird ein analytisches Modell zur Berechnung der Druckverteilung in Lamellendichtungen vorgestellt. Dazu wird die Strömung durch die Dichtung abschnittsweise betrachtet und mittels Methoden der Rohrhydraulik für laminare und inkompressible Strömungen modelliert. Die Geometrie der gesamten Dichtung wird zur einfacheren Variation parametrisiert. Die Ergebnisse der statischen Druckverteilung, des Leckagemassenstroms und des statischen Drucks auf eine einzelne Lamelle (Lift Up, Blow Down) werden mit bisher publizierten Daten verglichen. Unterschiedliche Variationen einer exemplarischen Dichtung werden analysiert um den Einfluss von Hochdruck- und Niederdruckspaltweite, Seitenplattenspaltweite, Lamellenanzahl und Lamellenspaltverlauf auf den Leckagemassenstrom zu zeigen. Weiters werden Berechnungen für ein patentiertes Lamellendesign vorgenommen. Zur Berechnung der Lamellenbiegung wird das Euler-Bernoulli Balkenmodel verwendet.

Das entwickelte analytische Modell ermöglicht die Beschreibung und Berechnung der Druckverteilung und des Leckagemassenstroms in Lamellendichtungen.

Contents

1 Introduction **1**

1.1 Motivation . . . 1

1.2 Scope and Outline of Thesis . . . 2

2 Technology of Leaf Seals **4**

2.1 Design . . . 4

2.2 Flow Characteristics . . . 6

2.3 Leaf Behavior . . . 9

2.3.1 Static Pressure Distribution . . . 9

2.3.2 Hydrodynamic Forces . . . 11

2.3.3 Contact Forces and Stiffness . . . 13

2.4 Heat Transfer . . . 13

2.5 Leakage . . . 14

2.6 Compliant Plate Seals . . . 15

3 Analytic Model of Pressure and Leakage **18**

3.1 Pressure Loss in the Side Plate Areas . . . 19

3.2 Mixing . . . 21

3.3 Pressure Distribution . . . 22

3.4 Leakage Mass Flow Rate . . . 26

3.4.1 Interleaf Gap . . . 27

3.4.2 Leaf Pack . . . 27

3.5 Parameter Study . . . 29

4 Results and Comparison of Pressure and Leakage **34**

4.1 Control of Radial Velocity and Reynolds number . . . 35

4.2 Pressure Distribution . . . 38

4.3 Leakage Mass Flow Rate . . . 43

4.3.1 Reynolds Number of Axial Flow . . . 44

4.3.2 Variations of MHI Design . . . 44

5 Deflection of Leaves **50**

5.1 Static Pressure Distribution . . . 50

5.1.1 Lift Up . . . 52

5.1.2 Blow Down . . . 53

5.2 Eccentric Rotor 54
5.3 Couette Flow 56

6 Results of Deflection Calculations 58
6.1 Load on the Leaves 58
6.2 Deflection 60
6.3 Eccentric Rotor 62
6.4 Couette Flow 62

7 Conclusion and Outlook 65
7.1 Conclusions 65
7.2 Limitations of the Model 66
7.3 Recommendations for Further Research 66

A Results and Comparison of Pressure and Leakage - Further Figures i
A.1 Comparison of Radial Velocities i
A.2 Comparison of Static Pressure Distributions ii
A.3 Comparison of Radial Velocities for Seal Variations iv

Nomenclature

Latin Symbols

A_i	leaf pack - rotor contact area	$[m^2]$
A_{IL}	interleaf gap area	$[m^2]$
$A_{SP,i}$	inner side plate gap cross section in radial direction	$[m^2]$
$A_{SP,o}$	outer side plate gap cross section in radial direction	$[m^2]$
A_z	mounting force	$[N]$
c	interleaf gap width at tip	$[m]$
c	velocity	$[\frac{m}{s}]$
c_1	model pipe inlet velocity	$[\frac{m}{s}]$
c_2	model pipe outlet velocity	$[\frac{m}{s}]$
c_a	axial velocity in the leaf pack	$[\frac{m}{s}]$
c_{HP}	high-pressure side plate gap inflow velocity	$[\frac{m}{s}]$
c_{LB}	axial velocity at the leaf base	$[\frac{m}{s}]$
c_{LP}	low-pressure side plate gap outlet velocity	$[\frac{m}{s}]$
c_r	radial velocity in the side plate gaps	$[\frac{m}{s}]$
$c_{r,max}$	maximum radial velocity in the side plate gaps	$[\frac{m}{s}]$
$c_{r,norm}$	normalized radial velocity in the side plate gaps	$[-]$
$c_{Ro,LP}$	radial velocity in the low-pressure side plate gap at the outer radius	$[\frac{m}{s}]$
$c_{Ro,HP}$	radial velocity in the high-pressure side plate gap at the outer radius	$[\frac{m}{s}]$
d_H	hydraulic diameter	$[m]$
E	Young's modulus	$[Pa]$
e	rotor excursion maximum	$[m]$
F_s	shear force due to Couette flow	$[N]$
$F_{s,Leaf}$	shear force due to Couette flow for a single leaf	$[N]$
$F_{s,Leaf,\perp}$	shear force due to Couette flow for a single leaf perpendicular to the length axis	$[N]$
f	factor for $f_D = f_F$	$[-]$
f_D	drain factor	$[-]$
f_F	influx factor	$[-]$
g_r	radial gap width due to hydrodynamic forces	$[m]$
h	leaf pack height	$[m]$
h_{ex}	leaf pack height for eccentric rotor	$[m]$
I	moment of inertia	$[m^4]$

i	side plate tip gap height	$[m]$
i_{ex}	side plate tip gap height for eccentric rotor	$[m]$
l	radial length of side plates for $l_{HP} = l_{LP}$	$[m]$
l_{HP}	radial length of the high-pressure side plate	$[m]$
l_{LP}	radial length of the low-pressure side plate	$[m]$
M	bending momentum	$[Nm]$
M_A	mounting momentum	$[Nm]$
M_s	torque due to Couette flow	$[Nm]$
m	interleaf gap width a base	$[m]$
$\dot{m}_L$	leakage mass flow rate of the a single interleaf gap	$[\frac{kg}{s}]$
$\dot{m}_{LT}$	leakage mass flow rate in the look through area	$[\frac{kg}{s}]$
$\dot{m}_{SP}$	leakage mass flow rate in the side plate area	$[\frac{kg}{s}]$
$\dot{m}_{tot}$	total leakage mass flow rate of the sealing	$[\frac{kg}{s}]$
N_z	rotor interference force	$[N]$
n	exponent of the velocity distribution	$[-]$
n	revolutions	$[min^{-1}]$
n_L	number of leaves	$[-]$
p	pressure	$[Pa]$
p_0	upstream pressure	$[Pa]$
p_1	downstream pressure	$[Pa]$
p_{HP}	pressure on the high-pressure side of the leaf pack	$[Pa]$
p_{LP}	pressure on the low-pressure side of the leaf pack	$[Pa]$
p_m	average pressure on the leaf	$[Pa]$
p_M	average pressure for physical fluid properties	$[Pa]$
$p_{SP,HP}$	pressure in the high-pressure side plate gap	$[Pa]$
$p_{SP,LP}$	pressure in the low-pressure side plate gap	$[Pa]$
Δp	pressure difference	$[Pa]$
Δp_{in}	inlet pressure loss	$[Pa]$
Δp_{LB}	pressure loss at the leaf base	$[Pa]$
$\Delta p_{Leafpack}$	pressure difference over the leaf pack	$[Pa]$
Δp_{mix}	mixing loss	$[Pa]$
Δp_{out}	outlet pressure loss	$[Pa]$
$\Delta p_{SP,HP}$	pressure loss in the high-pressure side plate gap	$[Pa]$
$\Delta p_{SP,LP}$	pressure loss in the low-pressure side plate gap	$[Pa]$
Δp_{tot}	pressure difference over the sealing	$[Pa]$
Q	shear force	$[N]$
q	leaf load	$[\frac{N}{m}]$
R	specific gas constant for air	$[\frac{J}{kgK}]$
R_i	inner sealing radius	$[m]$
R_o	outer sealing radius	$[m]$
Re	Reynolds number	$[-]$
s	width of rectangular duct	$[m]$
s	interleaf gap width	$[m]$

s_{BG}	interleaf gap width using equation from [25]	$[m]$
s_{cor}	tilting factor to correct the interleaf gap	$[-]$
s_{HP}	high-pressure side plate gap width	$[m]$
s_{LB}	interleaf gap width at the leaf base	$[m]$
s_{LP}	low-pressure side plate gap width	$[m]$
T	operating temperature	$[K]$
u	relative velocity	$[\frac{m}{s}]$
v	side plate ratio	$[m]$
v	beam shortening in beam direction	$[m]$
v_{rad}	beam shortening in radial direction	$[m]$
w_L	leaf width	$[m]$
w_{BD}	deflection for Blow Down design	$[m]$
$w_{BD,1}$	deflection for Blow Down design, system 1	$[m]$
$w_{BD,2}$	deflection for Blow Down design, system 2	$[m]$
w_{LU}	deflection for Lift Up design	$[m]$

Greek Symbols

α	lay angle	$[\circ]$
α_{cor}	corrected lay angle	$[\circ]$
$\alpha_{cor,ex}$	corrected lay angle for eccentric rotor	$[\circ]$
β	attachment angle	$[\circ]$
ϵ	rotor excursion	$[m]$
ζ_1	inlet resistant coefficient	$[-]$
ζ_2	outlet resistant coefficient	$[-]$
η	dynamic viscosity	$[Pas]$
Θ	angle from rotational axis	$[\circ]$
κ	leaf scale factor	$[-]$
λ	pipe friction coefficient	$[-]$
ν	kinematic viscosity	$[\frac{m^2}{s}]$
ρ	density	$[\frac{kg}{m^3}]$
τ	shear stress	$[\frac{N}{m^2}]$
χ	normalized pipe length	$[-]$
χ_s	normalized side plate height using x_s	$[-]$
χ_s^*	normalized side plate height using x_s^*	$[-]$
ψ	radial widening	$[-]$
ω	angular velocity	$[\frac{rad}{s}]$

Subscripts

$drain$	model pipe with continuous drain
$influx$	model pipe with continuous influx

Radial Coordinates

Due to the different parts of the model, four radial coordinates are used. Their connections are simple mathematical equations.

$r \in [0, R_o]$	starts at the rotational axis, direction from inner to outer	$[m]$
$x_r \in [0, i + l]$	starts at the sealing's inner radius R_i, direction from inner to outer	$[m]$
$x_s \in [0, l]$	starts at the side plates inner diameter, direction from inner to outer	$[m]$
$x_s^* \in [0, l]$	starts at the sealing's outer radius R_o, direction from outer to inner	$[m]$

The equations for the conversion of the coordinates are:

$$r = x_r + R_i \tag{1}$$

$$x_s = x_r - i \tag{2}$$

$$x_s + x_s^* = l \tag{3}$$

Abbreviations

CFD	Computational Fluid Dynamics
FE	Finite Elements
MHI	Mitsubishi Heavy Industries

Chapter 1

Introduction

1.1 Motivation

Mitigating the impact of man-made climate change and therefore the reduction of carbon dioxide emissions is one of the biggest challenges in the 21^{st} century. To reach this goal, fossil fuels have to replaced. Also the efficiency of existing technologies, such as turbomachines have to be increased, due to their importance and widespread use. They can be found in industrial plants, power plants and aircrafts.

Avoiding losses in the internal air system of gas turbines is an important way to increase efficiency. Hendricks et al. [24] conducted test on a T-700 gas turbine. The results showed that unnecessary compressor discharge gives a penalty of $3 - 5\%$ in fuel consumption.

The most common seals used in turbomachines are labyrinth seals, which use a cascade of annular orifices for the reduction of kinetic energy. For a minimum leakage the gaps should be as small as possible, however, non contact operation has to be ensured for all operational conditions. The demand for a reduction in losses gave advent to other sealing technologies.

The first one of these sealing technologies to be implemented in gas turbines are brush seals. These seal design was first proposed in the 1950's. However, the state of technology prevented successful use before the late 1980's. Brush seals are made out of a pack of bristles canted at an angle to the rotor and a backing plate, which prohibits axial deflection. In comparison to labyrinth seals, brush seals are in contact with the rotor during operation, therefore they are prone to wear. Brush seals reduce leakage up to 70% in comparison with a staged labyrinth seal with four fins. Additionally, the axial sealing length decreases, which helps in reducing the weight of the gas turbine. The static pressure distribution in the bristle pack presses the bristles against the rotor, an effect called *Blow Down*. Other problems are the so called *Hang Up* and *Blow Over*. The first one describes the effect of bristles pressing against the backing plate, resulting in a non-compliant operation during rotor excursions. The later one occurs for high-pressure differences over the seal. Due to the small axial rigidity of the bristles, they get bended in the direction of the flow and can break resulting in the destruction of the seal. Detailed studies are available, e.g. Neef et al. [7] or Pröstler [19].

In 2003 Watanabe et al. [8] (Mitsubishi Heavy Industries, MHI) presented the development of a high efficiency steam turbine. A cross-sectional view is shown in Fig. 1.1.

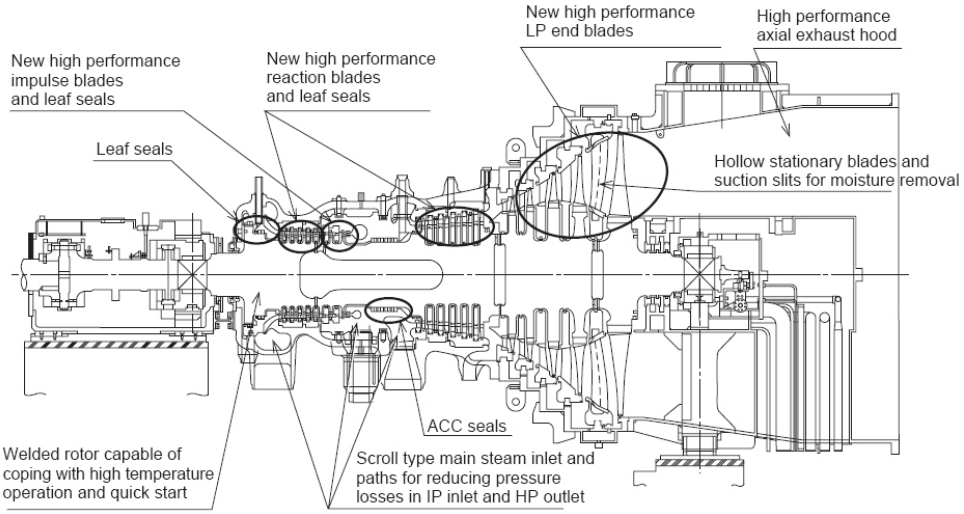

Figure 1.1: High Efficiency Steam Turbine [8]

Apart form other improvements, the authors presented a new seal design, called *leaf seal*. This seal contains metal leaves instead of bristles. Therefore the negative effects of brush seals can be avoided. Especially the need for a contacting plate on the low-pressure side is eliminated, due to axial rigidity of the leaves. This also allows for much higher pressure differences over the seal. In 2004 Nakane et al. [23] published an in depth study of a an experimental gas turbine, M501G, to date still the only documented turbine using leaf seals in operation, together with the complete sealing geometry, showing the potential of this technology. Since then most of the research work published is done at Oxford University in cooperation with Rolls Royce.

In 2011 Deo [5] from General Electric Global Research published a derivative of the leaf seal, called compliant plate seal. Although similar in construction, the operational behaviour is claimed to be outstanding.

1.2 Scope and Outline of Thesis

Almost two decades into research, leaf seals are still in prototype state. No comprehensive literature on them is available, therefore the first chapter is a summary of all papers and articles published until the submission of this thesis.

Based upon the pressure distributions published in the thesis of Bischelmaier [25], an analytical model will be developed. The aim is to find qualitative as well as quantitate correlations, which could lead to a to date non published approach. The leaf seal is therefore split up into different parts in such a way, that for each one the pressure and flow properties can be described using pipe flow correlation. To assess the behaviour of the model a parameter study will be appended. The results are compared with the data form [25]

In a next step leakages will be calculated and compared with the data from Nakane et al. [23], Ortner [2] and Bischelmaier [25]. Also variations in seal design will be made.

After this the focus shifts to leaf deflection and operational behaviour. Therefore the leaf is seen as a cantilever beam using Euler-Bernoulli beam theory. The effect of the static pressure distribution will be calculated and the magnitude of other forces will be assessed.

At the end there will be a summary of the thesis and propositions are made for the improvement of the model presented to lessen the effects of simplifications made and lift some restrictions. Also ideas for upcoming theses and further research are presented.

Chapter 2

Technology of Leaf Seals

This chapter is a summary of the literature regarding leaf seals published until the date of submission of this thesis. The aim is to give an overview of construction, physical properties, leakage and operational behaviour of this seal type.

At the end of the chapter compliant plate seals are presented. These seal design is very similar to leaf seals and it is claimed to perform better during transient conditions.

2.1 Design

A leaf seal consists of different parts: the leaf pack, the side plates or cover plates and the housing, [23], as is shown in Fig. 2.1. A photograph of an actual leaf seal is shown in Fig. 2.2[1].

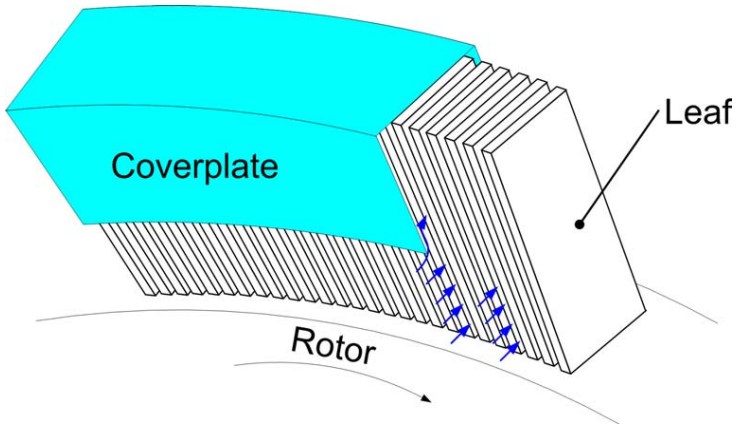

Figure 2.1: Isometric view of a leaf seal [17]

The leaf pack is made out of thin, flexible metal leaves. These are arranged around the rotor at a certain angle and fixed, usually welded, to the housing. A typical design has side plates both on the upstream and downstream side of the seal. The side plates can either be in contact with the leaf pack or at a certain distance. The geometric properties are shown in Fig. 2.3. The lay angle is in a range form 30 to 62°, [23], [10] and [20]. The inner sealing diameter and number of leaves are only published in two works, with a diameter of $350mm$ and 8581 leaves in [23] and a

[1]Please note, that in comparison to [23] in [10] the lay angle is measured at the outside diameter, however, in this thesis the nomenclature from [23] is used.

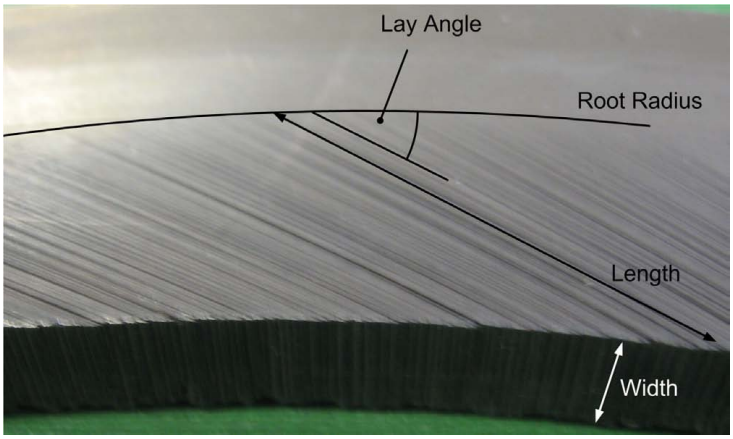

Figure 2.2: Photograph of a leaf seal [10]

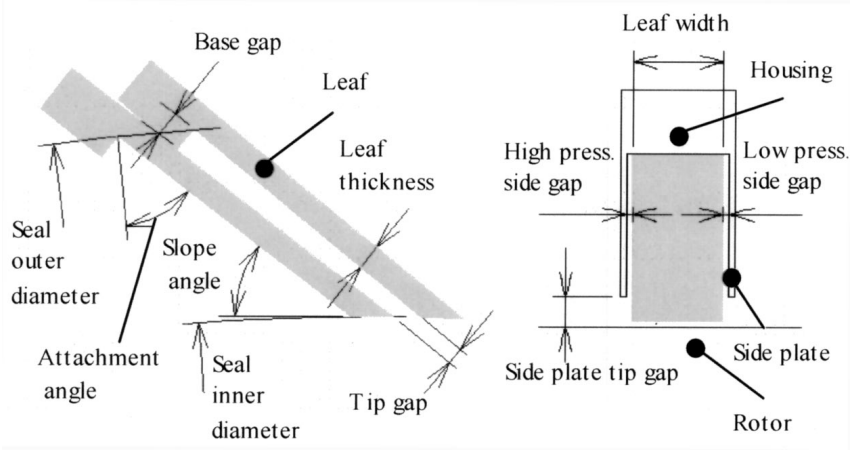

Figure 2.3: Geometric properties of a leaf seal [23]

diameter of 280mm and 4400 leaves in [20]. The outer sealing diameter and the leaf thickness was published by Nakane et al. [23] with 390mm for the diameter and 70μm as leaf thickness.

The side plate tip gap heights are in a range of 1.5mm, [23], to 3mm, [11]. Configurations with equal and unequal side plate tip gap heights on the upstream and downstream side are published. For the side plate gap widths values between 0.05mm, [23], and 0.50mm, [17], either in a symmetric composition or a non-symmetric one are found.

The published data shows a wide array of possible geometric properties. This could be due to the prototype character of this seal design.

2.2 Flow Characteristics

Nakane et al. [23] consider the flow inside the leaf pack as laminar. This is due to the small size of the flow area. This assumption is confirmed by the works of other authors, for example Franceschini et al. [17]. These authors used CFD software for simulation and found the Reynolds number in the leaf pack around 100. However, the authors did not publish their exact seal design. Qualitative assumptions of the flow field in a leaf seal are also published in [23]. These are shown in Fig. 2.4 for the three possibilities of side plate gap widths. For equal side

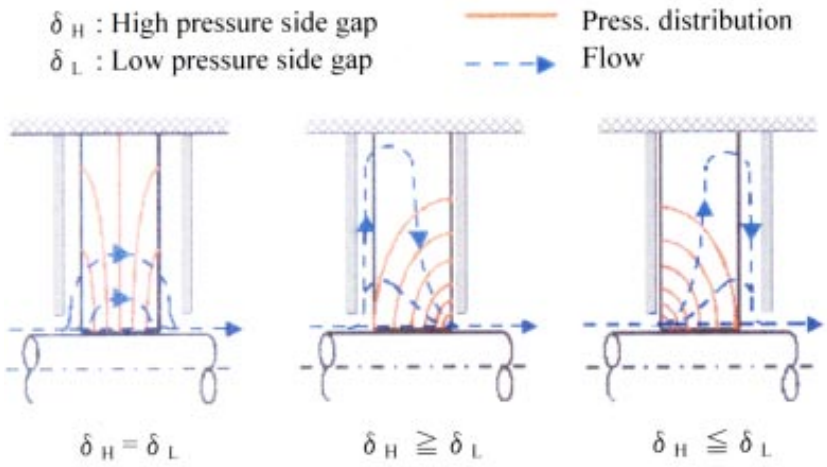

Figure 2.4: Axial flow fields of leaf seals [23]

plate gap widths the flow is assumed symmetrical. For a bigger high-pressure side plate gap width the flow in this gap is outbound, in the leaf pack inbound and vice versa for a bigger low-pressure side gap width. Due to the lay angle of the leaves, radial flows in the leaf pack always have circumferential velocity components.

Ortner [2] investigated the MHI leaf seal design using CFD. The author used laminar flow models for the simulation. The results show a linear pressure drop in the look-through area, the part of the seal between rotor and the side plate tips. The almost parabolic velocity distribution along the circumferential direction in the leaf pack has a slight displacement towards the undersides of the leaves.

Franceschini et al. [15] conducted a large scale experiment on leaf seal flow. Although the authors only tested one design, no high-pressure side plate and a leaf contacting low-pressure side plate, it is very useful to gain a better understanding of the flow field. The test rig was equipped with $20mm$ wide and $90mm$ long acrylic strips attached at an angle of about $45°$. The spacing between the strips was $10mm$. The test was made with a pressure difference of $400Pa$. The flow field is illustrated in Fig. 2.5. The authors identified seven distinct flow features, as

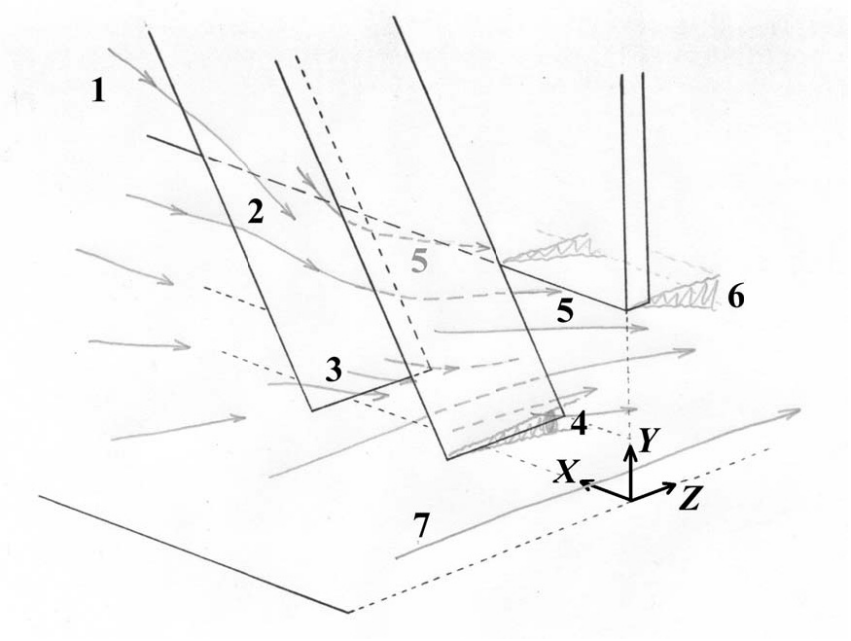

Figure 2.5: Flow field of a leaf seal [15]

shown in Fig. 2.5, [15] word-for-word:

1. Downward fluid motion approaching leading edge
2. Flow turning to align with strips
3. Swirl induced by the inclination of the strips
4. Flow separation vertically beneath the strips
5. Flow exiting strips with swirl
6. Separation under backing plate and flow contraction
7. Flow near floor aligned with axial direction

CFD simulations of the test were made correspondingly.

Jahn et al. [16] too simulated the flow field of a leaf seal with only a downstream side plate. The CFD simulations show another induced velocity component at the leaf tip. It is directed upwards due to the high flow resistance of the very narrow interleaf gap width.

Fico et al. [3] published flow field data of a seal (see Tab. 2.1 in the next section, light Blow Down). These plots are shown in Fig. 2.6.

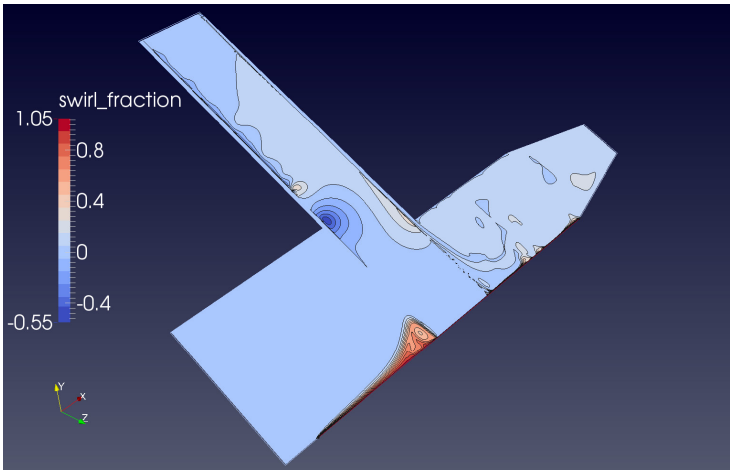

a: Swirl

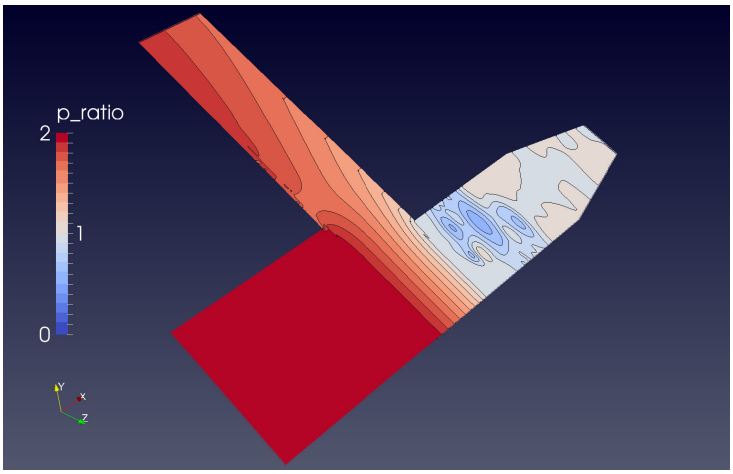

b: Pressure ratio

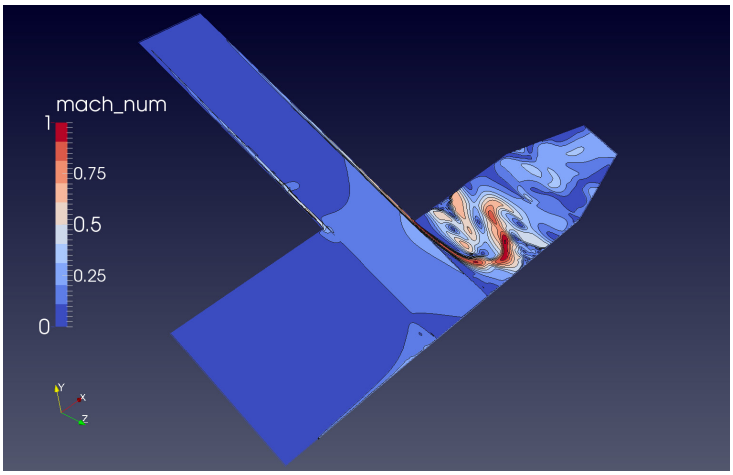

c: Mach number

Figure 2.6: Simulated flow fields [3]

The swirl generated by the rotor only has an effect upstream of the leaf pack and seems to have no impact on the leaf pack. The flow gains a negative swirl component in the outward direction,

the high-pressure side, and a positive in inward direction, the low-pressure side. This change in flow direction seems to take place mostly in the area near the entry and exit of the leaf pack.

2.3 Leaf Behavior

The biggest uncertainty regarding leaf seals are the forces acting on the leaves and therefore assure good performance for all operational parameters. This is due to the difficulty of measuring physical qualities responsible, like pressure distribution and flow field, inside the leaf seal. Nakane et al. [23] published a drawing, shown in Fig. 2.7, differing three forces: a rotor interference force, a hydrodynamic lifting force and a force generated by differential pressure. These

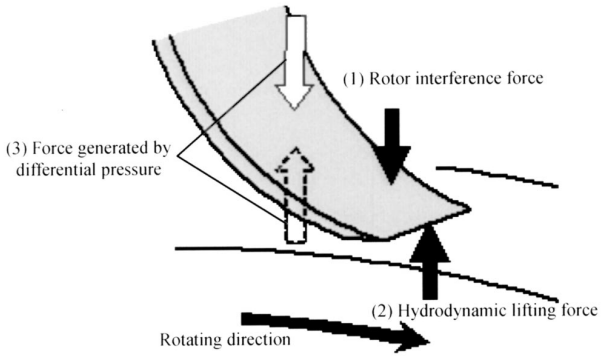

Figure 2.7: Forces on the leaves [23]

and other in literature assumed forces are presented in the next sections.

Jahn et al. [20] described three forces interacting with the rotor: the stiffness of the leaf pack, pressure and inertia.

Lift Up und *Blow Down* are effects coined during the research of brush seals. These terms are applied in a similar manner to leaf seals. Lift Up causes the leaf to move away from the rotor, depended on the context, either due to a single force, a physical phenomenon, e.g. inertia change, or the total resultant force acting on the leaf. Blow Down describes the opposite effect, causing the leaf to press against the rotor.

2.3.1 Static Pressure Distribution

If a pressure difference is applied on a leaf seal and gas flows through the sealing, there will be a radial pressure distribution in the leaf pack. Depending on the side plate gap widths, these distribution has a positive or negative gradient. Therefore the side plate gap widths are the main design parameter (Nakane et al. [23]). This can be seen in Fig. 2.4. Since the leaves are attached at an angle, there are different pressures on the upside and downside surface for a point along the middle axis of the leaf, which is shown in Fig. 2.8.

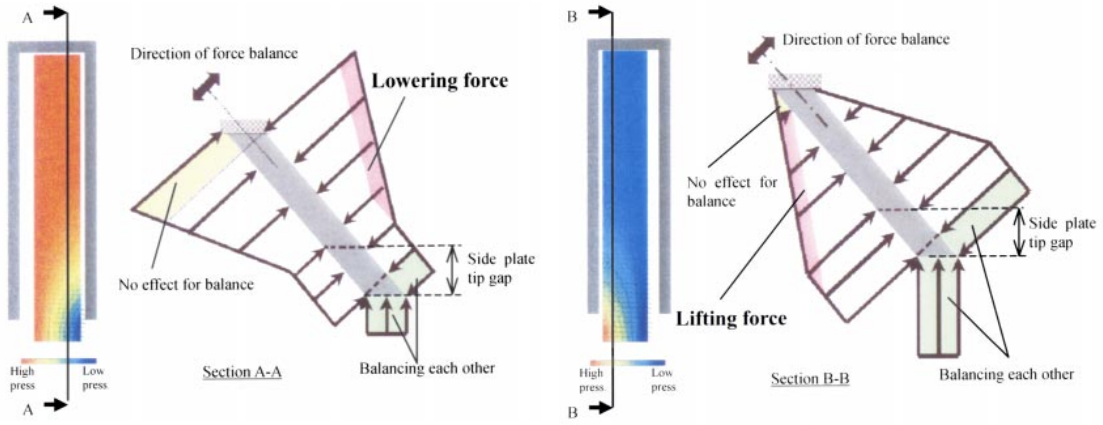

a: Blow Down

b: Lift Up

Figure 2.8: Blow Down and Lift Up due to static pressure distribution [23]

This phenomenon is well documented in literature, e.g. [2] and [16]. However, the assumption of a neutral behaviour for symmetrical side plate gaps, as implicitly stated in Fig. 2.4, seems to be wrong. Bischelmaier [25] made CFD simulations modelling the leaf pack as porous medium and found a Blow Down pressure distribution for equal side plate gaps. In [3] the authors mention a small Blow Down for such a configuration. Therefore it is necessary to include this unequal behaviour in the analytical model presented later.

Looking at the clearances in Tab. 2.1 it is interesting to note the change between a Blow Down and Lift Up configuration only by the change of side plate tip gaps values. The authors

Configuration	Clearances in mm			
	high-pressure side		low-pressure side	
	side gap	tip gap	side gap	tip gap
Light Blow Down	0.25	3	0.25	2
Strong Blow Down	0.35	3	0.15	3
Light Lift Up	0.25	2	0.25	3

Table 2.1: Gap clearances taken from [11]

do not state, if this is due to a change in static pressure distribution or momentum change. However, the authors write, the light Lift Up configuration was manufactured in a way to generate aerodynamic Blow Down. Therefore, the assumption can be made that the authors nomenclature only takes the static pressure distribution into account.

Pekris et al. [13] conducted tests with coned rotors. The seal was designed to perform neutral or with a light Lift Up for low pressure differences and with Blow Down for pressure differences over $2bar$. This would mean that not only the side plate clearances and tip clearances but also the pressure level has to be taken into account to predict the behaviour of the leaves.

2.3.2 Hydrodynamic Forces

Flow through the leaf seal and a circumferential velocity of the rotor are the two possible causes for hydrodynamic forces. However, which forces are acting is still unclear. In this section all proposed ones are presented.

Hydrodynamic Lift

Nakane et al. [23] firstly described the existence of a hydrodynamic lifting force. The authors tested the seal in a test stand and used an electrical circuit to measure if the seal is contacting. At a rotational speed of $n = 1500min^{-1}$ this circuit was interrupted, from this velocity on the operation was non contacting. This constitutes the presence of a hydrodynamic lifting force, however, the authors undertook no approach in their paper to clarify, which kind of force this could be.

Jahn et al. [14] investigated this behaviour and approximated the gap between the leaf tips and the rotor as a saw tooth profile, this can bee seen in Fig. 2.9. The authors ruled out air riding for gaps narrower than $0.3\mu m$ due the roughness of the rotor surface and for gaps wider than $2\mu m$, due to the decrease in lifting force.

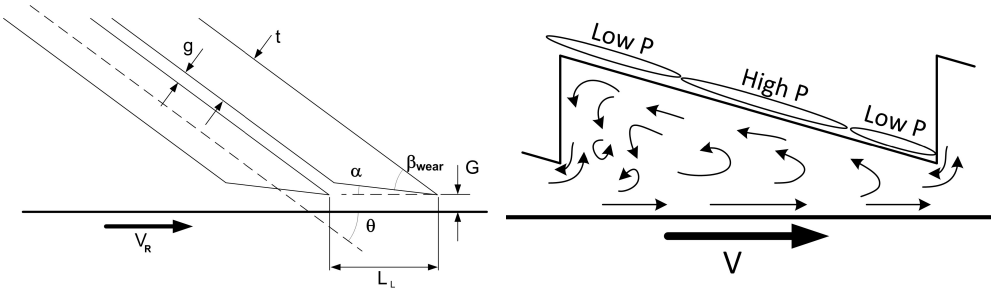

a: Geometry

b: Drawing of pressure distribution

Figure 2.9: Hydrodynamic lift model 1 [14]

For the CFD simulation the tip gap of the leaves were neglected. The flow under the leaf tips has an axial and circumferential component. The Reynolds number is around 100. The results are shown in Fig. 2.10. The authors stated, that the viscous recirculation under the tip is almost independent of ambient pressure and the axial flow.

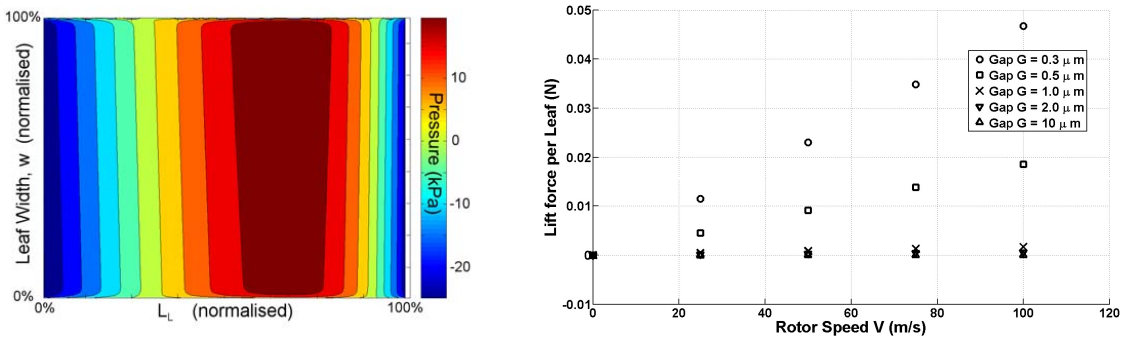

a: Simulated pressure distribution

b: Lifting forces

Figure 2.10: Hydrodynamic lift model 2 [14]

The CFD results were validated with laboratory test. The lift forces per leaf calculated are in the same order of magnitude as the forces calculated in this thesis.

Pekris et al. [11] used an approach with tapered channel flow. The authors considered the taper in axial direction and modelled the under tip region as 1-dimensional laminar flow of a Newtonian fluid. CFD results show forces per leaf in the same order of magnitude as the forces calculated in this thesis. The force increases with higher rotational speed. The authors made the calculations correspondingly to laboratory experiments. Three seal designs were used, a strong and light Blow Down configuration and a light Lift Up one. The gap data is shown in Tab. 2.1. Although the rotor was thin walled and therefore widened for higher rotational speeds, the derived torque decrease for the Blow Down seals. Therefore a non-contact operation was achieved.

Another cause of a hydrodynamic lifting force could be shear stress. This is mentioned in [11], however, any significant distribution is denied.

Momentum

Franceschini et al. [15] identified the momentum change of the leakage flow during entry and exit of the leaf pack as important contributor to leaf behaviour. The authors used a momentum balance to explain the effect for a seal design with no high-pressure side plate and a contacting low-pressure side plate. This is shown in Fig. 2.11. The change in swirl between inlet and

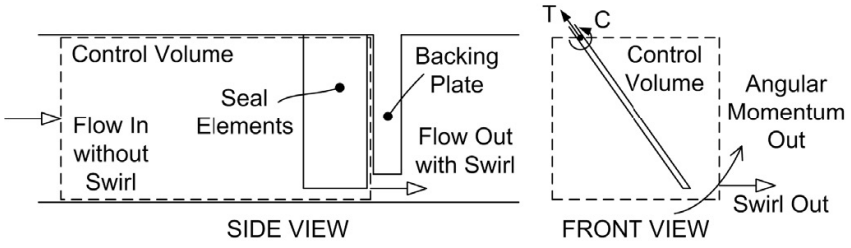

Figure 2.11: Momentum balance [15]

outlet could only be caused by the leaves, due to their lay angle. The reacting force causes

Blown Down. The large scale experiment showed the anticipated behaviour. Corresponding CFD analysis was used, also to make further variations. The Blow Down is proportional to the inlet velocity squared. Inlet swirl could either decrease or increase the Blow Down - for more vertical leaves, the Blow Down decreases.

In [11] the same effect was described to generate an aerodynamic Blow Down for the light Lift Up configuration (see Tab. 2.1).

2.3.3 Contact Forces and Stiffness

The leafs could be subjected to contact forces at four different possibilities. The leaf could be designed with contacting high-pressure and low-pressure side plates. If Lift Up or hydrodynamic air riding are not big enough and the leaf is designed with radial interference the leaves will have contact with the rotor. The last possibility is interleaf contact due to leaf deformation. The reasons could be either Lift Up or Blow Down or rotor excursion.

Contact, especially between leaves, also have a big impact of leaf pack stiffness. Jahn et al. [16] proposed an analytical model, taking aerodynamic and mechanical forces into account, for leaf stiffness and leaf torque. For high pressure differences the model has accurate predictions, however, for higher pressure differences the measured pack stiffness is higher than the calculated one. The authors explain this with interleaf contact, because this possibility is not included in the model.

Jahn et al. [20] described the phenomenon of non resetting forces during rotor excursion, observed during laboratory experiments. The authors called this negative stiffness. As explanation, the authors proposed an analytical model for the leaf pack stiffness, taking three different effects into the account: the mechanical stiffness of the seal, the static pressure distribution and the momentum change of the leakage mass flow. Franceschini et al. [17] provided an update to this model and used a laboratory setup for validation. The authors found a match between the prediction of the model and the behaviour of the seal. In 2016 Jahn et al. [16] published new results regarding negative stiffness. The low-pressure side plate tip gap height has a big impact on the relative contribution of the momentum change effecting the leaf pack stiffness. For higher pressure differences, the authors observed a deviation between the predicted results of the analytical model and the measured ones. The stiffness was higher than expected, due to interleaf contact.

2.4 Heat Transfer

Most recent publication focus on heat transfer. Pekris et al. [1] modeled the heat transfer using one dimensional heat conduction along the leaf in radial direction, one dimensional convection along the leaf in axial direction and the energy balance for the leaf. The interleaf gap was assumed to be a rectangular duct with laminar flow. This model was validated using the Oxford test facility. Overall the correlation was good, however, some deviation occurred for high-pressure differences. The power split of friction heat between leaf and rotor was $50 - 60\%$.

Even for a temperature rise in the model of up to $400K$, the rotor does not exceed ambient temperature by much. This is due to the construction of leaf seals, acting as very effective heat exchangers with high temperature gradients.

Pelegrin-Garcia et al. [9] built a static test rig for research into heat transfer. It uses a heater mesh to create a temperature gradient. The authors made use of a 2D axisymmetric CFD mesh to simulate the test rig and modelled the leaf pack as porous medium, an approach for leaf seals developed at the Technische Universität Wien by Bischelmaier [25]. Some correlation was found upstream, downstream of the seal, measurements and simulation results matched.

2.5 Leakage

Nakane et al. [23] published measured and simulated leakage of the MHI seal design, shown in Fig. 2.12. The authors did not use normalized values, therefore making comparisons easier. The leakage is of similar magnitude than of brush seals and significant lower than for a straight

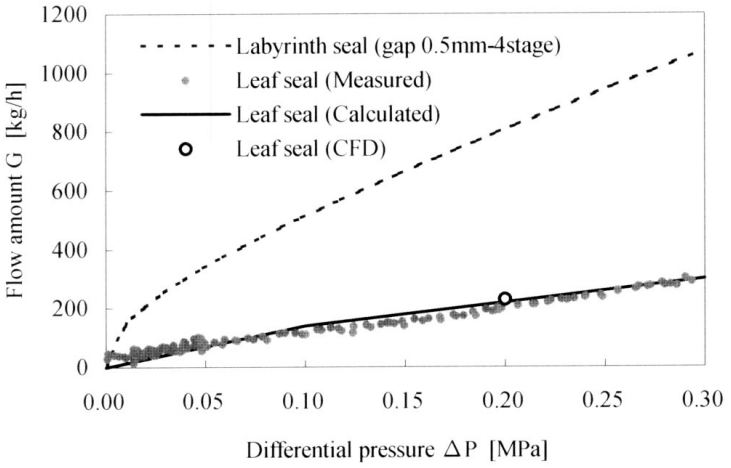

Figure 2.12: Leakage of MHI seal [23]

labyrinth seal with four tips.

Pekris et al. [11] tested a leaf geometry with different side plate clearances (see Tab. 2.1). For the results, the authors used the effective clearance and normalized it to the highest value measured, as shown in Fig. 2.13. The effective clearance is the height of in ideal annular orifice to allow for the same leakage under the same conditions as the seal. It is use to compare different seals. The smallest leakage was achieved with a strong Blow Down configuration.

Ortner [2] modeled the leaf seal using one dimensional gas dynamic and electrical circuit analogy. The author split the seal in different sections, and calculated the pressure loss due to friction using pipe flow correlation, shown in Fig. 2.14a.

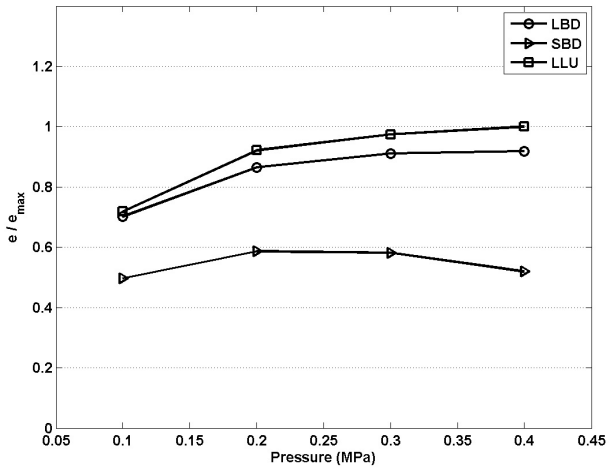

Figure 2.13: Effective clearance of leaf seal [11]

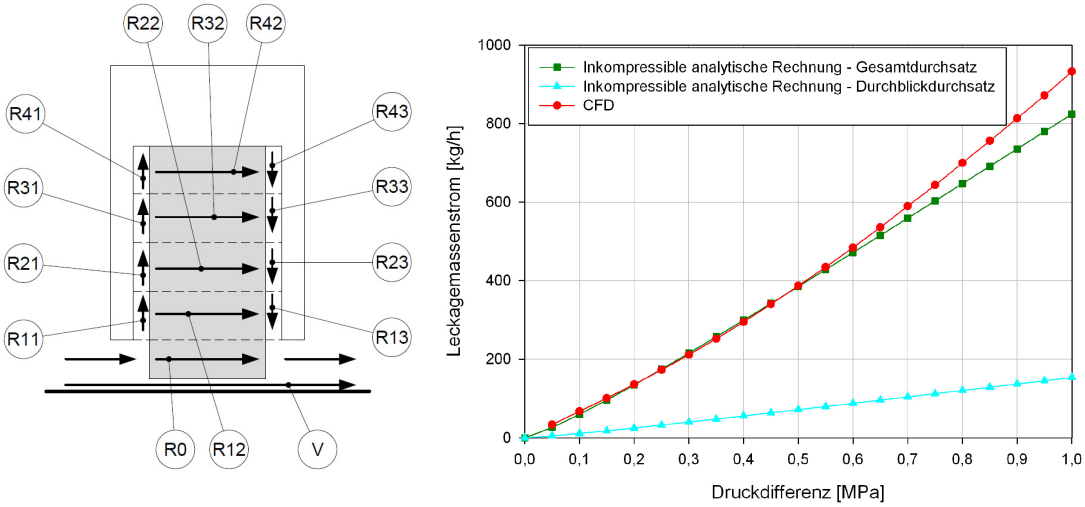

a: Axonometric projection

b: Leakage mass flow rate

Figure 2.14: One dimensional gas dynamic model [2]

The calculated leakage mass flow rate matches for small pressure differences with the authors CFD simulation, Fig. 2.14b.

The rotational velocity has little impact on the leakage performance. This effect is published in multiple papers, e. g. [11] and [13].

2.6 Compliant Plate Seals

Deo [5] proposed this new seal design similar to leaf seals. As shown in Fig. 2.15 the main difference is an intermediate plate and U-shaped leaves, called compliant plates.

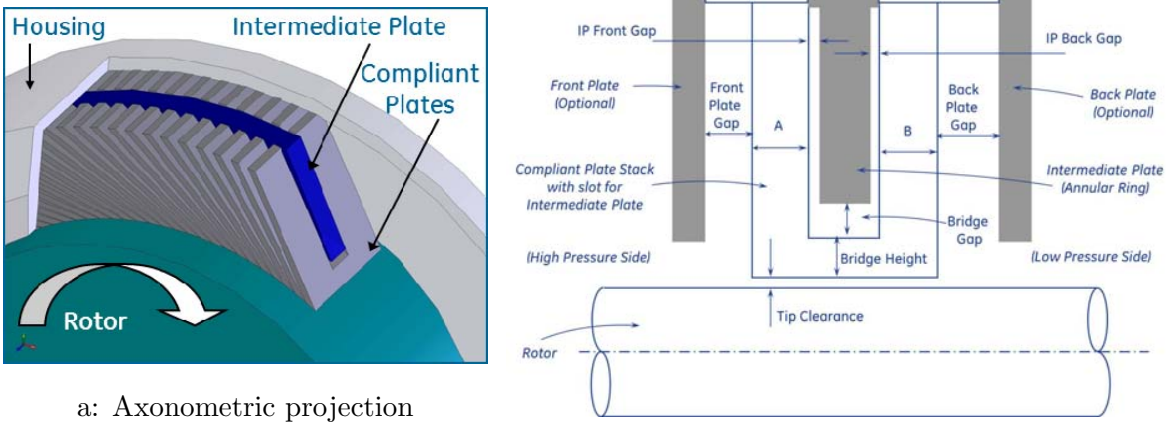

a: Axonometric projection

b: Cross section

Figure 2.15: Compliant plate seal [5]

The aim of this design is to have only static pressure feedback on the compliant plates for a stable tip clearance and get rid of uncertain hydrodynamic effects. This is achieved by "coupling" - a Blow Down and Lift Up leaf together, shown in Fig. 2.16.

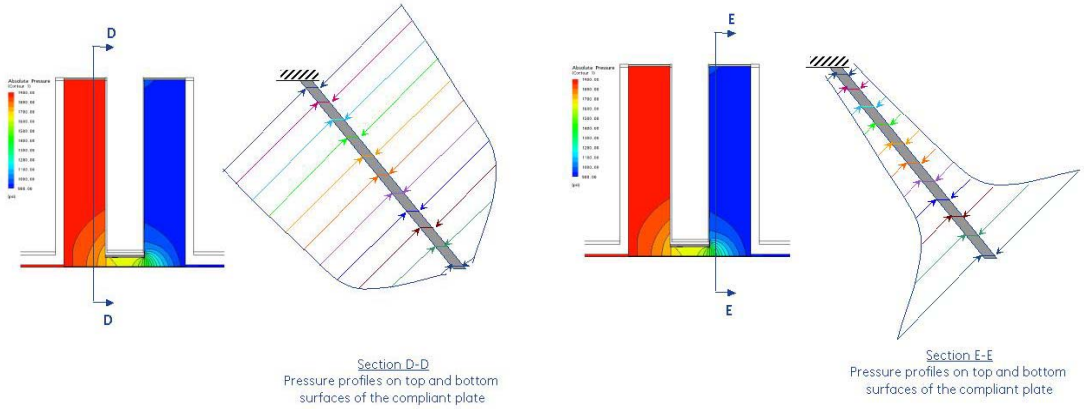

a: Blow Down side

b: Lift Up side

Figure 2.16: Compliant plate pressure distribution [5]

Any rotor eccentricity and therefore change in tip clearance will change the mass flow, pressure distribution and the magnitude of the Lift Up and Blown Down resulting in a new stable condition guaranteeing non-contact operation, shown in Fig. 2.17. The advantages would be less wear, less rotor and leaf heating, therefore making the replacement of expensive material with cheaper substitutes possible, reduced maintenance and no performance loss over time (Deo [5]). Deo et al. [6] conducted experiments with such a seal and found this behaviour to be insensitive to a lot of conditions, e. g.:

- Rotational speed ($0 - 10000\ \mathrm{min}^{-1}$) and direction (forward and reverse)
- Manufacturing deviations
- Reverse pressurization

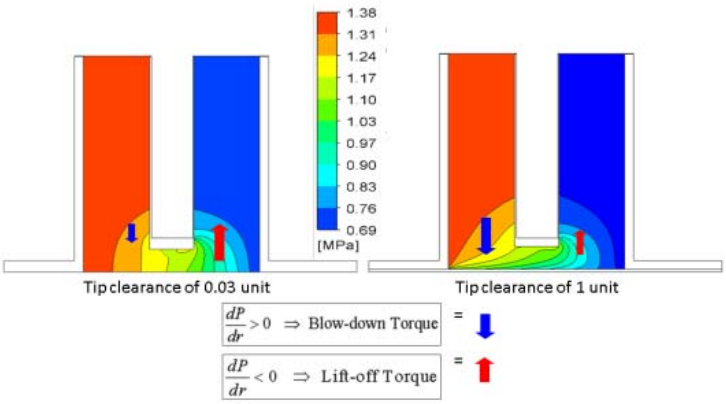

Figure 2.17: Self correcting behaviour of compliant plate seals [4]

- Assembly clearances
- Rotor excursion up to $1mm/rev$
- Wide ratios of intermediate plate front gap to intermediate plate back gap, between 0.25 and 4

It is also stated, that the front plate and back plate gaps have little influence, even for a large value of $1.25mm$ and leakage is independent of the rotational velocity.

In [4] and [5] CFD analysis of this seal were made to validate the effects found.

The authors made the verification of their statements possible as almost the complete geometric parameters are presented in [6].

Chapter 3

Analytic Model of Pressure and Leakage

In this chapter the analytic model for a leaf seal will be presented. Therefore, the seal is split into different modelling sections: the inlet, the outlet, the look-through area, the high-pressure side plate gap, the low-pressure side plate gap and the leaf pack. The calculations for different velocity gradients inside the side plates are presented.

Fig. 3.1 is a drawing of the seal with all measures and coordinates used. The radial interference is assumed to be zero.

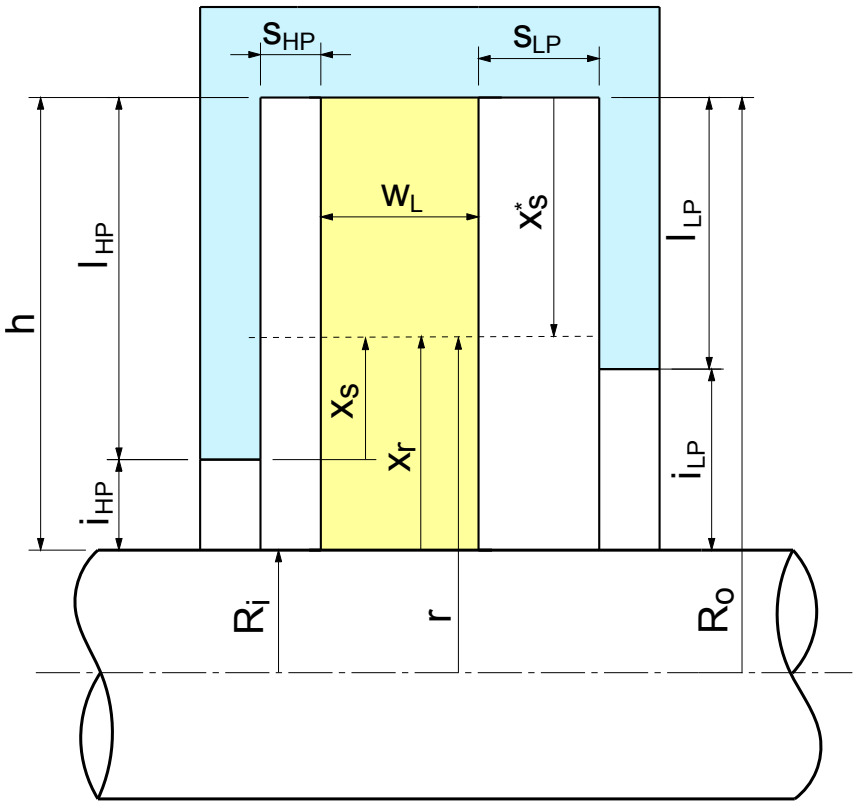

Figure 3.1: Drawing of the seal

In this calculation, the independence of mixing and friction losses is assumed. Therefore these losses can be calculated separately.

The flow is considered laminar and incompressible. The density ρ and the dynamic viscosity η are constant. The pipe friction correlation

$$-\frac{dp}{dx} = \lambda \frac{1}{d_H} \rho \frac{c^2}{2} \overset{(3.2)}{\Longleftrightarrow} \frac{12\eta c}{s^2} \tag{3.1}$$

is used, to calculate the pressure loss. For a rectangular duct where the width is much larger than the height the right side of Eqn. (3.1) can be transformed as follows:

$$\lambda \frac{1}{d_H} \varrho \frac{c^2}{2} = \frac{96}{Re} \frac{1}{d_H} \varrho \frac{c^2}{2} = \frac{96\nu}{c d_H} \frac{1}{d_H} \varrho \frac{c^2}{2} = \frac{96\eta}{2s} \frac{1}{2s} \frac{c}{2} = \frac{12\eta c}{s^2} \tag{3.2}$$

Here s is the side plate gap width and c the flow velocity.

3.1 Pressure Loss in the Side Plate Areas

The pressure variation in the area between the side plates and the leaf pack is assumed to be due to:

1. Friction
2. Change in mass flow [27]
3. Change of cross section
4. Mixing losses on the low-pressure side

The effect of point 3. is left unconsidered, due to the small ratio

$$\psi = \frac{A_{SP,o}}{A_{SP,i}} = \frac{2R_o \pi s}{2(R_i + i)\pi s} = \frac{R_o}{R_i + i} \tag{3.3}$$

between the inner radius and the outer radius. For the MHI seal the value is $\psi = 1.1048$.

In [27] a linear velocity distribution is assumed. For the ease of variation, here two polynomial distributions with variable exponent are used, one for drain and one for influx. Both use c_1 as inlet and c_2 as outlet velocity. Therefore the drain distribution is

$$c_{drain}(\chi) = c_{2,drain} + (c_{1,drain} - c_{2,drain})(1 - \chi)^n \tag{3.4}$$

and the distribution for the influx is

$$c_{influx}(\chi) = c_{1,influx} + (c_{2,influx} - c_{1,influx})\chi^n. \tag{3.5}$$

Eqn. (3.5) is only valid for an unvaried axial flow or a symmetrical, two dimensional flow in the leaf pack. However, in this paper only the assumption of an unvaried axial flow is used. These velocity distributions are shown in Fig. 3.2 for different exponents using the drain factor

$$f_D = \frac{c_{2,drain}}{c_{1,drain}} \tag{3.6}$$

and the influx factor

$$f_F = \frac{c_{1,influx}}{c_{2,influx}}. \tag{3.7}$$

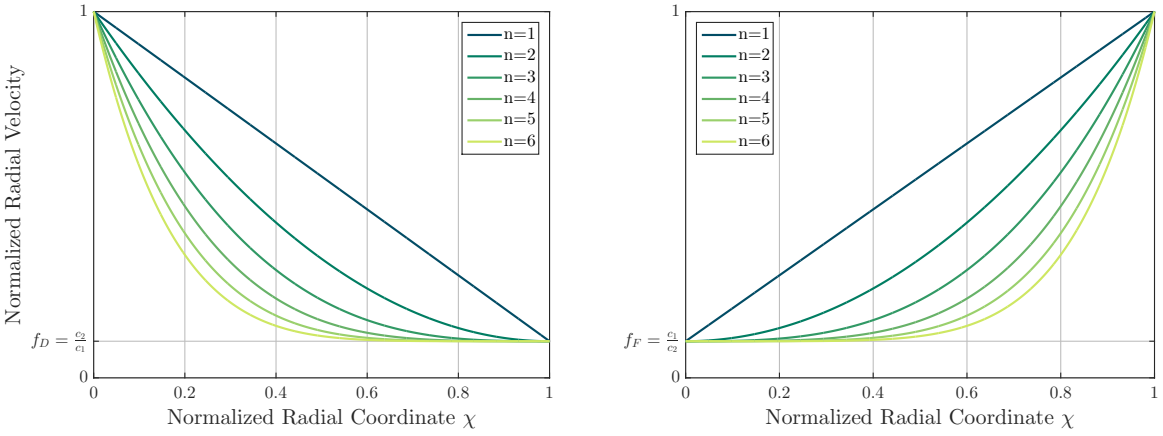

a: Drain b: Influx

Figure 3.2: Assumed velocity distributions

Eqn. (3.4) and Eqn. (3.5) use

$$\chi = \frac{x}{l} \tag{3.8}$$

as normalized pipe length. For further calculations also the differential correlation $d\chi = \frac{dx}{l}$ is used. The conditions for the inlet and outlet velocities are

$$c_{2,drain} < c_{1,drain} \tag{3.9}$$

and

$$c_{2,influx} > c_{1,influx}. \tag{3.10}$$

From now on, for the ease of reading, the subscripts *drain* and *influx* of the velocities are omitted. Eqn. (3.4) and Eqn. (3.5) are each inserted in Eqn. (3.1), giving

$$-dp_{drain} = \frac{12\eta}{s^2}\left[c_2 + (c_1 - c_2)(1-\chi)^n\right] dx = \frac{12\eta}{s^2}\left[c_2 + (c_1 - c_2)(1-\chi)^n\right](l\,d\chi) \tag{3.11}$$

and

$$-dp_{influx} = \frac{12\eta}{s^2}\left[c_1 + (c_2 - c_1)\chi^n\right] dx = \frac{12\eta}{s^2}\left[c_1 + (c_2 - c_1)\chi^n\right](l\,d\chi) \tag{3.12}$$

As boundary conditions for the differential equation

$$p_{drain}(\chi = 0) = p_{0,drain} \tag{3.13}$$

and

$$p_{influx}(\chi = 0) = p_{0,influx} \tag{3.14}$$

are used. The pressure difference for a pipe with drainage is

$$p_{0,drain} - p_{drain}(\chi) = \Delta p_{drain}(\chi) = \frac{12\eta l}{s^2}\left[c_2\chi - (c_1 - c_2)\frac{(1-\chi)^{n+1}}{n+1} + \frac{c_1 - c_2}{n+1}\right] \tag{3.15}$$

and for a pipe with influx

$$p_{0,influx} - p_{influx}(\chi) = \Delta p_{influx}(\chi) = \frac{12\eta l}{s^2}\left[c_1\chi + (c_2 - c_1)\frac{\chi^{n+1}}{n+1}\right]. \tag{3.16}$$

Eqn. (3.15) and Eqn. (3.16) are rewritten using this factors from Eqn. (3.13) and Eqn. (3.14),

$$\begin{aligned}\Delta p_{drain}(\chi) &= \frac{12\eta l}{s^2}\left[c_2\chi - (c_1 - c_2)\frac{(1-\chi)^{n+1}}{n+1} + \frac{c_1 - c_2}{n+1}\right] = \\ &= \frac{12\eta l}{s^2}c_1\left[f_D\chi + \frac{1-f_D}{n+1}\left[1-(1-\chi)^{n+1}\right]\right] =\end{aligned} \tag{3.17}$$

and

$$\begin{aligned}\Delta p_{influx}(\chi) &= \frac{12\eta l}{s^2}\left[c_1\chi + (c_2 - c_1)\frac{\chi^{n+1}}{n+1}\right] = \\ &= \frac{12\eta l}{s^2}c_2\left[f_F\chi + (1-f_F)\frac{\chi^{n+1}}{n+1}\right].\end{aligned} \tag{3.18}$$

3.2 Mixing

For a pipe with influx, not only pressure loss due to flow resistance occurs, also losses due to mixing effects have to be taken into account.

The velocity distribution for the pipe with influx Eqn. (3.5) is transformed, using the influx factor

$$\begin{aligned}c_{influx}(\chi) &= c_1 + (c_2 - c_1)\chi^n = \\ &= c_2\left(f_F + (1-f_F)\chi^n\right)\end{aligned} \tag{3.19}$$

and the differential

$$\begin{aligned}\frac{dc}{dx} &= \frac{dc_{influx}}{l d\chi} = \\ &= c_2 n(1-f_F)\frac{\chi^{n-1}}{l}\end{aligned} \tag{3.20}$$

is calculated. Eqn. (3.19) and Eqn. (3.20) are inserted in the differential equation taken from [18]

$$\begin{aligned}-\frac{dp_{mix}}{dx} &= \rho c_{influx}\frac{dc_{influx}}{dx} = \\ &= \rho c_2^2\frac{n(1-f_F)}{l}\left[f_F\chi^{n-1} + (1-f_F)\chi^{2n-1}\right]\end{aligned} \tag{3.21}$$

and solved using the boundary condition

$$p_{mix}(\chi = 0) = 0. \tag{3.22}$$

Eqn. (3.21) will only be valid, if the flow direction of the mixed in part is perpendicular to the flow direction of the main flow. Therefore, the pressure loss due to mixing is

$$\Delta p_{mix} = -\rho c_2^2 (1 - f_F) \left[f_F \chi^n + \frac{1 - f_F}{2} \chi^{2n} \right]. \tag{3.23}$$

For the case of an inlet velocity $c_1 = 0$, the influx factor f_F also equals 0 and the pressure loss due to influx for the whole pipe is

$$\Delta p_{mix}(\chi = 1) = -\rho \frac{c_2^2}{2} \tag{3.24}$$

for every assumed distribution. The pressure loss in Eqn. (3.24) is equal to the dynamic pressure of the outlet flow.

3.3 Pressure Distribution

The total pressure drop

$$\Delta p_{tot} = \rho \frac{c_{HP}^2}{2} + \Delta p_{in} + \Delta p_{SP,HP}(\chi_s = 1) + \Delta p_{LB} + \Delta p_{SP,LP}(\chi_s^* = 1) + \Delta p_{out} \tag{3.25}$$

of the whole seal can be split in six parts. The inlet

$$\Delta p_{in} = \zeta_1 \frac{c_{HP}^2}{2} \rho \tag{3.26}$$

and outlet losses

$$\Delta p_{out} = \zeta_2 \frac{c_{LP}^2}{2} \rho \tag{3.27}$$

are calculated using resistance coefficients and the reference velocities c_{HP} and c_{LP}. The term $\rho \frac{c_{HP}^2}{2}$ is necessary, because the upstream pressure is the total pressure p_0 whereas the downstream p_1 is the static pressure.

For the high-pressure side c_{HP} is used as inlet velocity. Therefore the loss is

$$\Delta p_{SP,HP}(\chi_s) = \frac{12 \eta l_{HP}}{s_{HP}^2} c_{HP} \left[f_D \chi_s + \frac{1 - f_D}{n + 1} \left[1 - (1 - \chi_s)^{n+1} \right] \right]. \tag{3.28}$$

For the low-pressure side plate gap, the mixing losses are added, giving

$$\begin{aligned} \Delta p_{SP,LP}(\chi_s^*) &= \Delta p_{SP,LP,pipe}(\chi_s^*) + \Delta p_{SP,LP,mix}(\chi_s^*) = \\ &= \frac{12 \eta l_{LP}}{s_{LP}^2} c_{LP} \left[f_F \chi_s^* + (1 - f_F) \frac{\chi_s^{*n+1}}{n + 1} \right] + \rho c_{LP}^2 (1 - f_F) \left[f_F \chi_s^{*n} + \frac{1 - f_F}{2} \chi_s^{*2n} \right] \end{aligned} \tag{3.29}$$

and the loss at the base of the leaf

$$\Delta p_{LB} = \frac{12 \eta w c_{LB}}{s_{LB}^2} \tag{3.30}$$

is calculated using the laminar duct flow correlation.

For the case of equal side plate height, the flow lengths in the high-pressure side plate gap and in the low-pressure side plate gap

$$l_{HP} = l_{LP} = l \tag{3.31}$$

are equal, the mass balance divided by the circumference of the side plate gaps

$$c_{HP} s_{HP} = c_{LP} s_{LP} \tag{3.32}$$

for only axial flow in the leaf pack, connects the reference values. This simplification and the nomenclature can be seen in Fig. 3.3.

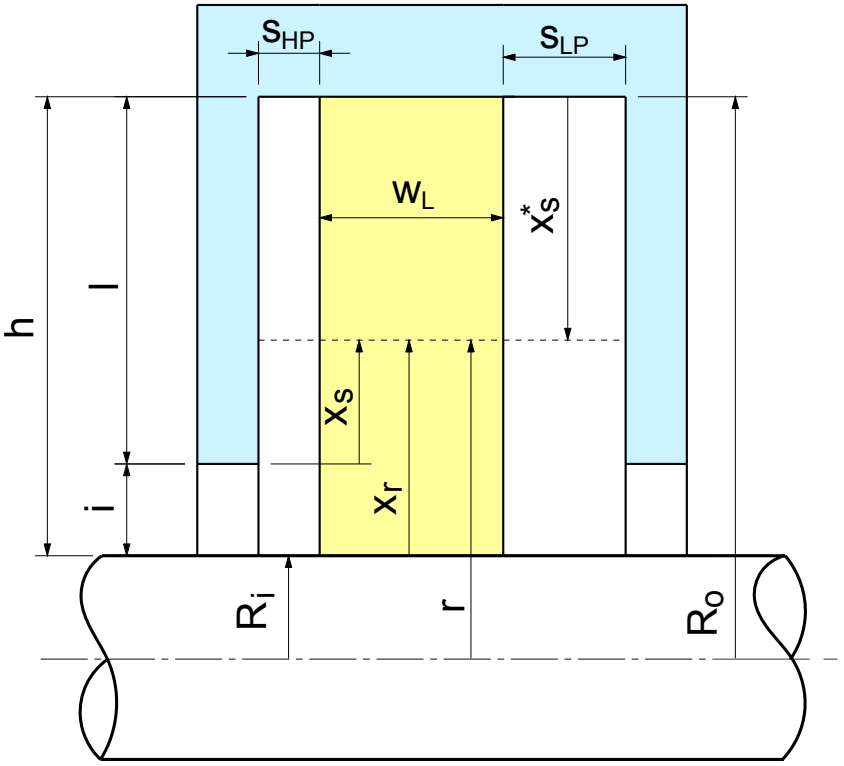

Figure 3.3: Drawing of the Simplified Seal

The mass balance on the outer radius divided by the circumference

$$\begin{aligned} c_{R_o,HP} s_{HP} &= f_D c_{HP} s_{HP} = \\ &= c_{LB} s_{LB} = \\ &= c_{R_o,LP} s_{LP} = \\ &= f_F c_{LP} s_{LP} = \\ &= f_F \frac{c_{HP} s_{HP}}{s_{LP}} s_{LP} = \\ &= f_F c_{HP} s_{HP} \end{aligned} \tag{3.33}$$

connects the velocity at the leaf base c_{LB} and the high-pressure side reference velocity c_{HP} and the feed factor with the drain factor

$$f_D = f_F = f, \tag{3.34}$$

which are equal for this case. The dependencies form Eqns. (3.31-3.34) are used to rewrite Eqns. (3.26-3.30). Inserted in Eqn. (3.25), this is a quadratic equation

$$Ac_{HP}^2 + Bc_{HP} + C = 0 \tag{3.35}$$

with

$$A = \frac{\rho}{2} + \zeta_1\frac{\rho}{2} + \zeta_2\frac{\rho}{2}\left(\frac{s_{HP}}{s_{LP}}\right)^2 + \rho(1-f)\left(\frac{s_{HP}}{s_{LP}}\right)^2\left(f + \frac{1-f}{2}\right) \tag{3.36}$$

and

$$B = \frac{12\eta l}{s_{HP}^2}\left(f + \frac{1-f}{n+1}\right) + \frac{12\eta l}{s_{LP}^2}\frac{s_{HP}}{s_{LP}}\left(f + \frac{1-f}{n+1}\right) + \frac{12\eta w}{s_{LB}^2}\frac{f s_{HP}}{s_{LB}} \tag{3.37}$$

and

$$C = -\Delta p_{tot} \tag{3.38}$$

for c_{HP}. This velocity must be positive, therefore a unique solution can be found.

For the case of a velocity at the leaf base equal to 0, further simplifications can be made. For this case, the factor f is also 0. The quadratic equation for c_{HP}

$$Ac_{HP}^2 + Bc_{HP} + C = 0 \tag{3.39}$$

with

$$A = \frac{\rho}{2} + \zeta_1\frac{\rho}{2} + \zeta_2\frac{\rho}{2}\left(\frac{s_{HP}}{s_{LP}}\right)^2 + \frac{\rho}{2}\left(\frac{s_{HP}}{s_{LP}}\right)^2 \tag{3.40}$$

and

$$B = \frac{12\eta l}{(n+1)s_{HP}^2} + \frac{12\eta l}{(n+1)s_{LP}^2}\frac{s_{HP}}{s_{LP}} \tag{3.41}$$

and

$$C = -\Delta p_{tot} \tag{3.42}$$

can be solved without any further assumptions. All other variables are physical properties or geometric values.

With the knowledge of c_{HP} the pressure levels in the side plate areas are calculated. The pressure distribution in the high-pressure side plate gap

$$\begin{aligned} p_{SP,HP}(\chi_s) &= p_0 - \frac{c_{HP}^2}{2}\rho - p_{in} - \Delta p_{SP,HP}(\chi_s) = \\ &= p_0 - \frac{c_{HP}^2}{2}\rho - \zeta_1\frac{c_{HP}^2}{2}\rho - \frac{12\eta l}{s_{HP}^2}c_{HP}\left[f\chi_s + \frac{1-f}{n+1}\left[(1-(1-\chi_s)^{n+1}\right]\right] \end{aligned} \tag{3.43}$$

and in the low-pressure side plate gap

$$\begin{aligned} p_{SP,LP}(\chi_s^*) &= p_0 - \frac{c_{HP}^2}{2}\rho - p_{in} - \Delta p_{SP,HP}(\chi = 1) - \Delta p_{LB} - \Delta p_{SP,HP}(\chi_s^*) = \\ &= p_0 - \frac{c_{HP}^2}{2}\rho - p_{in} - \frac{12\eta l}{s_{HP}^2} c_{HP} \left[f + \frac{1-f}{n+1} \right] - \frac{12\eta w f s_{HP}}{s_{LB}^3} c_{HP} - \\ &\quad - \frac{12\eta l s_{HP}}{s_{LP}^3} c_{HP} \left[f\chi_s^* + (1-f)\frac{\chi_s^{*n+1}}{n+1} \right] - \\ &\quad - \rho c_{HP}^2 \frac{s_{HP}^2}{s_{LP}^2}(1-f) \left[f\chi_s^{*n} + \frac{1-f}{2}\chi_s^{*2n} \right] \end{aligned} \tag{3.44}$$

are then calculated. In Fig. 3.3 the geometric link

$$x_s + x_s^* = l \tag{3.45}$$

can be seen. It is used to transform the normalized length

$$\chi_s^* = \frac{x_s^*}{l} = \frac{l - x_s}{l} = 1 - \chi_s \tag{3.46}$$

of the side plates. For the calculation of the leakage mass flow rate the pressure difference over the leaf pack

$$\begin{aligned} \Delta p_{\text{Leafpack},SP}(\chi_s) &= p_{HP}(\chi_s) - p_{LP}(\chi_s^*) = \\ &= p_{HP}(\chi_s) - p_{LP}(1-\chi_s) = \\ &= p_0 - \frac{c_{HP}^2}{2}\rho - p_{in} - \frac{12\eta l}{s_{HP}^2} c_{HP} \left[f\chi_s + \frac{1-f}{n+1}\left[1 - (1-\chi_s)^{n+1}\right] \right] - \\ &\quad - p_0 + \frac{c_{HP}^2}{2}\rho + p_{in} + \frac{12\eta l}{s_{HP}^2} c_{HP} f + \frac{12\eta w f s_{HP}}{s_{LB}^3} c_{HP} + \\ &\quad + \frac{12\eta l s_{HP}}{s_{LP}^3} c_{HP} \left[f\,(1-\chi_s) + (1-f)\frac{(1-\chi_s)^{n+1}}{n+1} \right] - \\ &\quad - \rho c_{HP}^2 \left(\frac{s_{HP}}{s_{LP}} \right)^2 (1-f) \left[f(1-\chi_s)^n + \frac{1-f}{2}(1-\chi_s)^{2n} \right] = \\ &= 12\eta l c_{HP} \left[\frac{1}{s_{HP}^2} + \frac{s_{HP}}{s_{LP}^3} \right] \left[f(1-\chi_s) + \frac{1-f}{n+1}(1-\chi_s)^{n+1} \right] + \frac{12\eta w f s_{HP}}{s_{LB}^3} c_{HP} + \\ &\quad + \rho c_{HP}^2 \left(\frac{s_{HP}}{s_{LP}} \right)^2 (1-f) \left[f(1-\chi_s)^n + \frac{1-f}{2}(1-\chi_s)^{2n} \right] \end{aligned} \tag{3.47}$$

is necessary. For the deflection due to static pressure, the average of the upstream side plate pressure and the downstream side plate pressure

$$\begin{aligned} p_{m,SP}(\chi_s) &= \frac{p_{SP,HP}(\chi_s) + p_{SP,LP}(\chi_s^*)}{2} = \\ &= \frac{p_{SP,HP}(\chi_s) + p_{SP,LP}(1-\chi_s)}{2} = \\ &= p_0 - \frac{c_{HP}^2}{2}\rho - p_{in} - \frac{6\eta l}{s_{HP}^2} c_{HP} \left[f(1+\chi_s) + \frac{1-f}{n+1}\left[2-(1-\chi_s)^{n+1}\right]\right] - \\ &\quad - \frac{6\eta l s_{HP}}{s_{LP}^3} c_{HP} \left[f(1-\chi) + \frac{1-f}{n+1}(1-\chi_s)^{n+1}\right] - \frac{6\eta w f s_{HP}}{s_{LB}^3} c_{HP} - \\ &\quad - \rho\frac{c_{HP}^2}{2}\left(\frac{s_{HP}}{s_{LP}}\right)^2 (1-f)\left[f(1-\chi_s)^n + \frac{1-f}{2}(1-\chi_s)^{2n}\right] \end{aligned} \tag{3.48}$$

is used. For the case of a drain factor and an influx factor equal to zero, Eqn. (3.47) and Eqn. (3.48) can again be simplified to

$$\begin{aligned} \Delta p_{\text{Leafpack},SP}(\chi_s, f=0) = \frac{12\eta l}{n+1} c_{HP} \left[\frac{1}{s_{HP}^2} + \frac{s_{HP}}{s_{LP}^3}\right](1-\chi_s)^{n+1} + \\ + \rho c_{HP}^2 \left(\frac{s_{HP}}{s_{LP}}\right)^2 \left[\frac{(1-\chi_s)^{2n}}{2}\right] \end{aligned} \tag{3.49}$$

and

$$\begin{aligned} p_{m,SP}(\chi_s, f=0) = p_0 - \frac{c_{HP}^2}{2}\rho - p_{in} - 6\eta l c_{HP}\left[\frac{2-(1-\chi_s)^{n+1}}{s_{HP}^2(n+1)} + \frac{s_{HP}(1-\chi_s)^{n+1}}{s_{LP}^3(n+1)}\right] - \\ - \rho\frac{c_{HP}^2}{2}\left(\frac{s_{HP}}{s_{LP}}\right)^2 \left[\frac{(1-\chi_s)^{2n}}{2}\right]. \end{aligned} \tag{3.50}$$

For the part of the seal between the rotor and the side plate tips, called look through area, the pressure difference is

$$\Delta p_{\text{Leafpack},LT} = \Delta p_{tot} - \frac{c_{HP}^2}{2}\rho - \Delta p_{in} - \Delta p_{out} \tag{3.51}$$

and the average pressure is

$$p_{m,LT} = \frac{\Delta p_{tot} - \frac{c_{HP}^2}{2}\rho - \Delta p_{in} - \Delta p_{out}}{2} + p_1. \tag{3.52}$$

The pressure difference for the look through area is an approximation connecting the pressure variation in series. However, simulated pressure and flow velocity distributions, e.g. in [2], show a much more complex behaviour.

3.4 Leakage Mass Flow Rate

For the calculation of the leakage mass flow rate, information regarding the interleaf gap width is connected with the pressure difference acting on the leaf pack.

3.4.1 Interleaf Gap

For the calculation of the leakage mass flow rate, the interleaf gap width in dependency from the radial coordinate is necessary. The Eqns. (3.53-3.56) derived in [25], are used.

The interleaf gap width is approximated by:

$$s_{BG}(r) = 2\left(\frac{c}{2} + \sin\delta\sqrt{2R_i r\cos\left(\frac{1-\frac{R_i}{r}}{\tan\alpha}\right) + R_i^2}\right) \tag{3.53}$$

The gap opening angle

$$\delta = \arcsin\frac{m}{l(R_o)} \tag{3.54}$$

is calculated exactly by using the equations for the centre angle ϕ

$$\tan\alpha\sin\phi(r) - \cos\phi(r) = -\frac{R_i}{r} \tag{3.55}$$

and for the leaf length

$$l(r,\phi) = \sqrt{(r\sin\phi(r))^2 + (r - (R_i + r((1-\cos(\phi(r))))))^2} \tag{3.56}$$

at the outer radius R_o.

The leaf gap width has to be modified by tilting it into circumferential direction using a simple linear model:

$$s_{cor}(x_r) = \frac{1}{\sin\left(\alpha - \frac{\beta-\alpha}{h}x_r\right)} \tag{3.57}$$

This is due to s_{BG} being perpendicular on the axis of symmetry of the interleaf gap, as can be seen in Fig. 3.4. The leaf gap width function used for the leakage mass flow rate calculation is

$$\begin{aligned} s(x_r) &= s_{cor}(x_r)s_{BG}(x_r) = \\ &= \frac{2}{\sin\left(\alpha - \frac{\beta-\alpha}{h}x_r\right)}\cdot \\ &\quad\cdot\left(\frac{c}{2} + \sin\delta\sqrt{2R_i(x_r+R_i)\cos\left(\frac{1-\frac{R_i}{(x_r+R_i)}}{\tan\alpha}\right) + R_i^2}\right) \end{aligned} \tag{3.58}$$

combining Eqn. (3.53) and Eqn. (3.57). Please note the coordinate change from r to x_r.

3.4.2 Leaf Pack

The pressure difference, which is driving the fluid through the leaf pack has two sections. The borders of the inner one are the rotor diameter and the height of the side plate tip gap. The

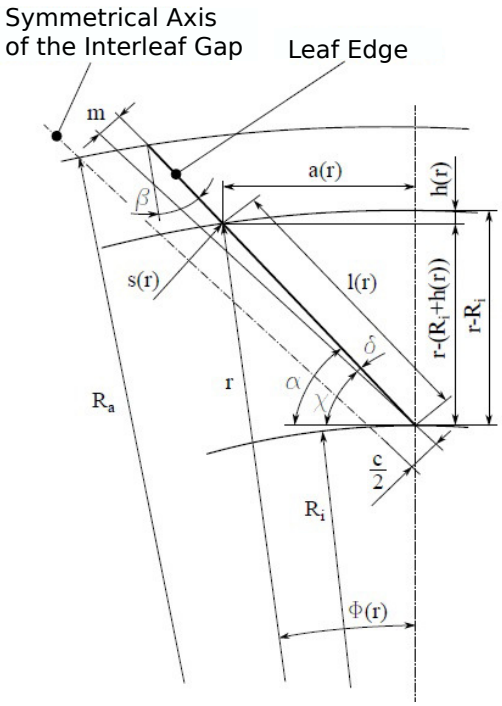

Figure 3.4: Geometrical properties of leaf gap [25]

outer one is the area bordered by the side plates.

$$\Delta p(x_r) = \begin{cases} p_0 - \frac{c_{HP}^2}{2}\rho - \Delta p_{in} - \Delta p_{out} - p_1 & , \quad x_r \leq i \\ 12\eta l c_{HP}\left[\frac{1}{s_{HP}^2} + \frac{s_{HP}}{s_{LP}^3}\right]\cdot & \\ \cdot\left[f\left(1 - \frac{x_r - i}{l}\right) + \frac{1-f}{n+1}\left(1 - \frac{x_r - i}{l}\right)^{n+1}\right] + & \\ + \frac{12\eta w f s_{HP}}{s_{LB}^3} c_{HP} + & , \quad x_r > i \\ + \rho c_{HP}^2 \left(\frac{s_{HP}}{s_{LP}}\right)^2 (1-f)\cdot & \\ \cdot\left[f\left(1 - \frac{x_r - i}{l}\right)^n + \frac{1-f}{2}\left(1 - \frac{x_r - i}{l}\right)^{2n}\right] & \end{cases} \tag{3.59}$$

The inner difference is the upstream pressure reduced by the inlet pressure drop and the downstream pressure. Pleas note that in Eqn. (3.59) the pressure difference in the look through part of the leaf pack is not dependent upon the radial coordinate. The pressure difference for the side plate gaps is taken from Eqn. (3.47). This equation's variable is transformed using

$$\chi_s = \frac{x_s}{l} = \frac{x_r - i}{l}. \tag{3.60}$$

For the pressure drop in the leaf pack, again the correlation in Eqn. (3.2) is used. The length in this case is the width of the leaves w_L.

$$\Delta p = \frac{12\eta w_L c(x_r)}{s^2(x_r)} \tag{3.61}$$

Eqn. (3.59) and Eqn. (3.61) combined result in the axial velocity.

$$c_a(x_r) = \begin{cases} (p_0 - \frac{c_{HP}^2}{2}\rho - \Delta p_{in} - \Delta p_{out} - p_1)\frac{s^2(x_r)}{12\eta w_L} & , \quad x_r \leq i \\ c_{HP}s^2(x_r)\frac{l}{w_L}\left[\frac{1}{s_{HP}^2} + \frac{s_{HP}}{s_{LP}^3}\right]\cdot & \\ \quad \cdot\left[f\left(1 - \frac{x_r - i}{l}\right) + \frac{1-f}{n+1}\left(1 - \frac{x_r - i}{l}\right)^{n+1}\right] + & \\ \quad + \frac{s^2(x_r) f s_{HP}}{s_{LB}^3} c_{HP} + & , \quad x_r > i \\ \quad + \frac{\rho c_{HP}^2 s^2(x_r)}{12\eta w_L}\left(\frac{s_{HP}}{s_{LP}}\right)^2 (1-f)\cdot & \\ \quad \cdot\left[f\left(1 - \frac{x_r - i}{l}\right)^n + \frac{1-f}{2}\left(1 - \frac{x_r - i}{l}\right)^{2n}\right] & \end{cases} \tag{3.62}$$

The leakage mass flow rate is the integral across the sealing height.

$$\begin{aligned} \dot{m}_L &= \int_0^h c(x_r)s(x_r)dx_r = \\ &= \int_0^i \frac{(p_0 - \frac{c_{HP}^2}{2}\rho - \Delta p_{in} - \Delta p_{out} - p_1)s^2(x_r)}{12\eta w_L} s(x_r)dx_r + \\ &\quad + \int_i^h \left[c_{HP}s^2(x_r)\frac{l}{w}\left(\frac{1}{s_{HP}^2} + \frac{s_{HP}}{s_{LP}^3}\right)\left[f\left(1 - \frac{x_r - i}{l}\right) + \frac{1-f}{n+1}\left(1 - \frac{x_r - i}{l}\right)^{n+1}\right] + \right. \\ &\quad + \frac{s^2(x_r) f s_{HP}}{s_{LB}^3} c_{HP} + \\ &\quad \left. + \frac{\rho c_{HP}^2 s^2(x_r)}{12\eta w_L}\left(\frac{s_{HP}}{s_{LP}}\right)^2 (1-f)\left[f\left(1 - \frac{x_r - i}{l}\right)^n + \frac{1-f}{2}\left(1 - \frac{x_r - i}{l}\right)^{2n}\right] s(x_r)\right] dx_r = \\ &= \underbrace{\int_0^i \frac{(p_0 - \frac{c_{HP}^2}{2}\rho - \Delta p_{in} - \Delta p_{in} - p_1)s^3(x_r)}{12\eta w_L} dx_r}_{\dot{m}_{LT}} + \\ &\quad + \int_i^h \left[c_{HP}s^3(x_r)\frac{l}{w}\left(\frac{1}{s_{HP}^2} + \frac{s_{HP}}{s_{LP}^3}\right)\left[f\left(1 - \frac{x_r - i}{l}\right) + \frac{1-f}{n+1}\left(1 - \frac{x_r - i}{l}\right)^{n+1}\right] + \right. \\ &\quad + \frac{s^3(x_r) f s_{HP}}{s_{LB}^3} c_{HP} + \\ &\quad \left. + \underbrace{\frac{\rho c_{HP}^2 s^3(x_r)}{12\eta w_L}\left(\frac{s_{HP}}{s_{LP}}\right)^2 (1-f)\left[f\left(1 - \frac{x_r - i}{l}\right)^n + \frac{1-f}{2}\left(1 - \frac{x_r - i}{l}\right)^{2n}\right]}_{\dot{m}_{SP}}\right] dx_r \end{aligned} \tag{3.63}$$

3.5 Parameter Study

To assess the model presented, a normalized sealing is used to make variations on different parameters. This is only made for the pressure distribution, as for the leakage mass flow rate

additional information about the leaf pack is necessary.

In Fig. 3.5 variations in exponent, resistance coefficients, mixing and leaf base flow for a ratio of $v = \frac{s_{HP}}{s_{LP}} = 1$ are shown. For an increasing exponent the pressure curves become steeper. If the mixing losses are added, as shown in Fig. 3.5b, the pressure at the leaf base will shift to higher values. This effect will not be seen, if the outlet resistance coefficient ζ_2 is set to 0 (Fig. 3.5f). For a flow at the leaf base of $f = 0.05$ the pressure difference at the leaf base is higher for increasing exponents (Fig. 3.5c and 3.5d).

In Fig. 3.6 the ratio v is changed and all other parameters are kept constant. The exponents only have an impact on the curve gradients. Starting with a normalized static pressure of 0.4 with $v = 1$, the pressure level increases together with v and decreases in the same way. The pressure loss at the leaf base increases with decreasing v, as seen in Fig. 3.6c and Fig. 3.6d. The outlet loss has only a small impact on the pressure distribution, shown in Fig. 3.6e and Fig. 3.6f.

In Fig. 3.7 different values of f are plotted. Again higher exponents increase the steepness of the pressure distribution. The pressure difference acting on the leaf pack increases with increasing f and with decreasing inlet loss and therefore decreasing resistance coefficient ζ_1.

without mixing loss

with mixing loss

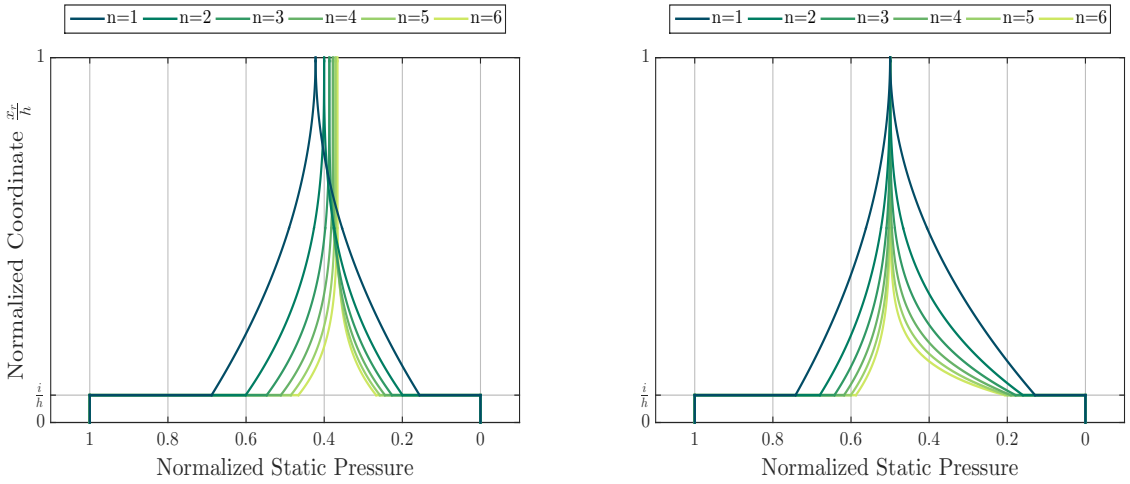

a: $\zeta_2 = 1,\ f = 0$

b: $\zeta_2 = 1,\ f = 0$

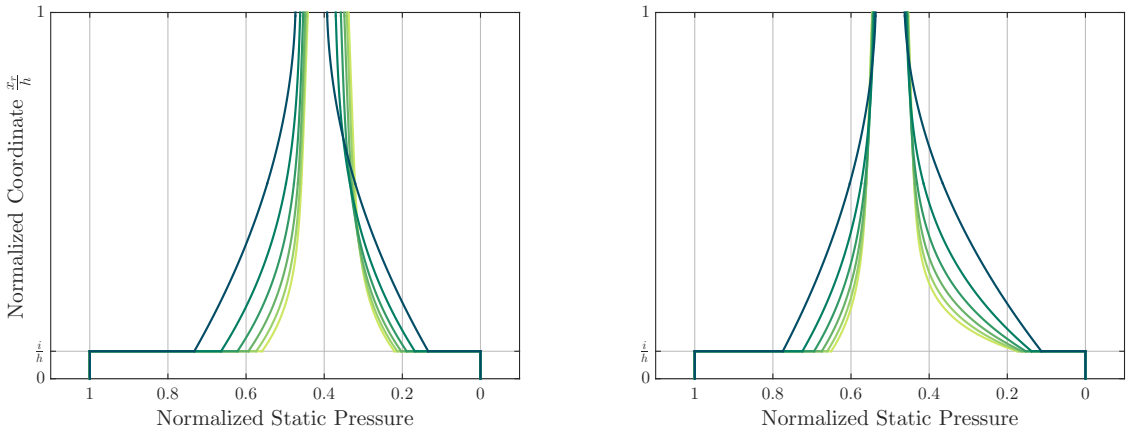

c: $\zeta_2 = 1,\ f = 0.05$

d: $\zeta_2 = 1,\ f = 0.05$

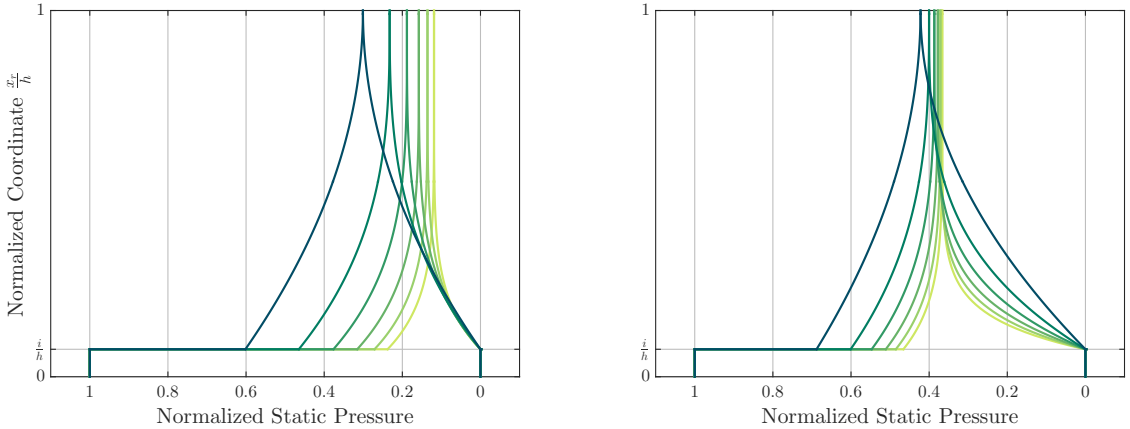

e: $\zeta_2 = 0,\ f = 0$

f: $\zeta_2 = 0,\ f = 0$

Figure 3.5: Parameter study 1, $\frac{s_{HP}}{s_{LP}} = 1,\ \zeta_1 = 1$

$n = 2$ $n = 4$

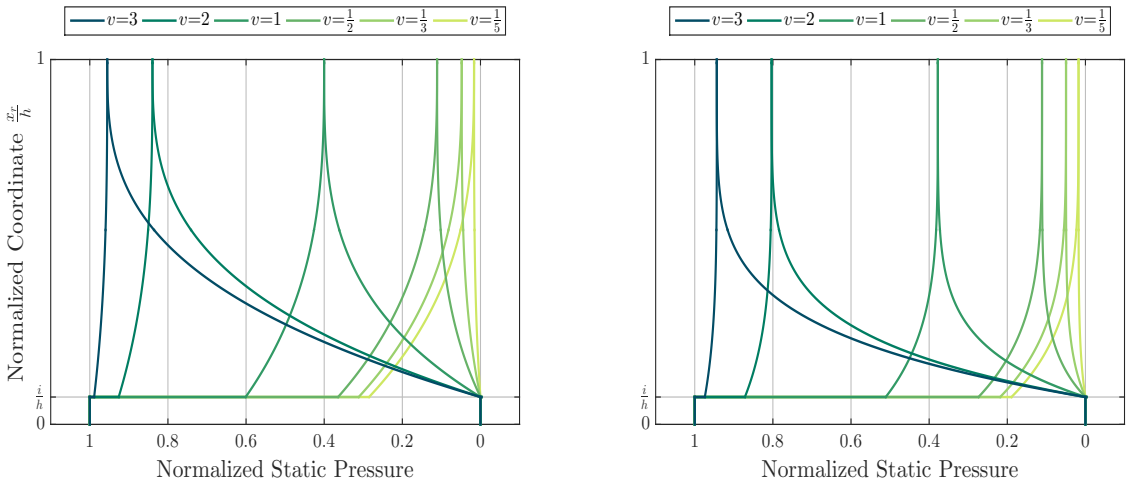

a: $\zeta_2 = 0,\ f = 0$ b: $\zeta_2 = 0,\ f = 0$

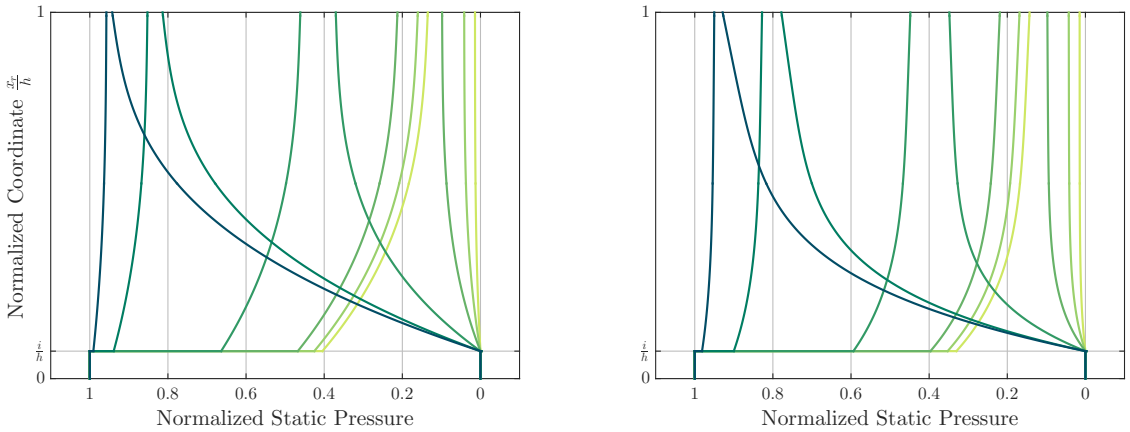

c: $\zeta_2 = 0,\ f = 0.05$ d: $\zeta_2 = 0,\ f = 0.05$

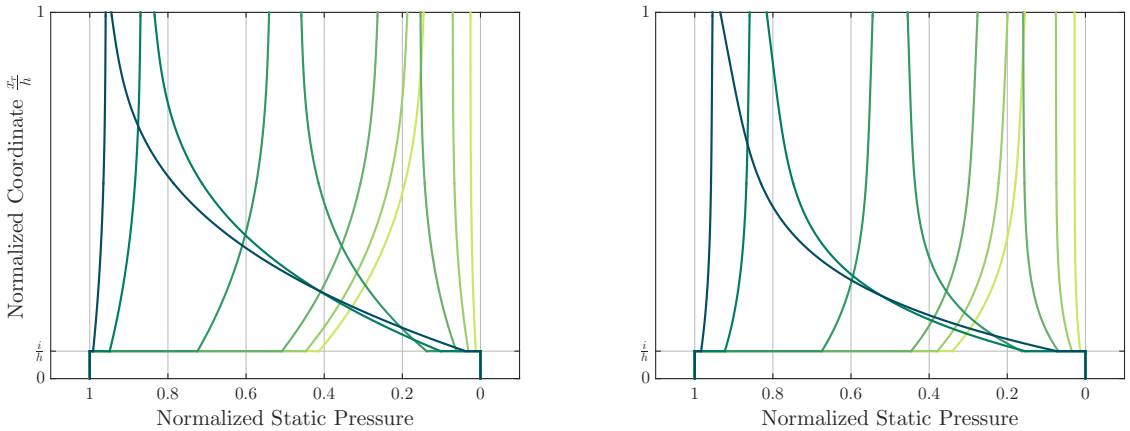

e: $\zeta_2 = 1,\ f = 0.05$ f: $\zeta_2 = 1,\ f = 0.05$

Figure 3.6: Parameter study 2, $\zeta_1 = 1$, with mixing losses

$n = 2$ $n = 4$

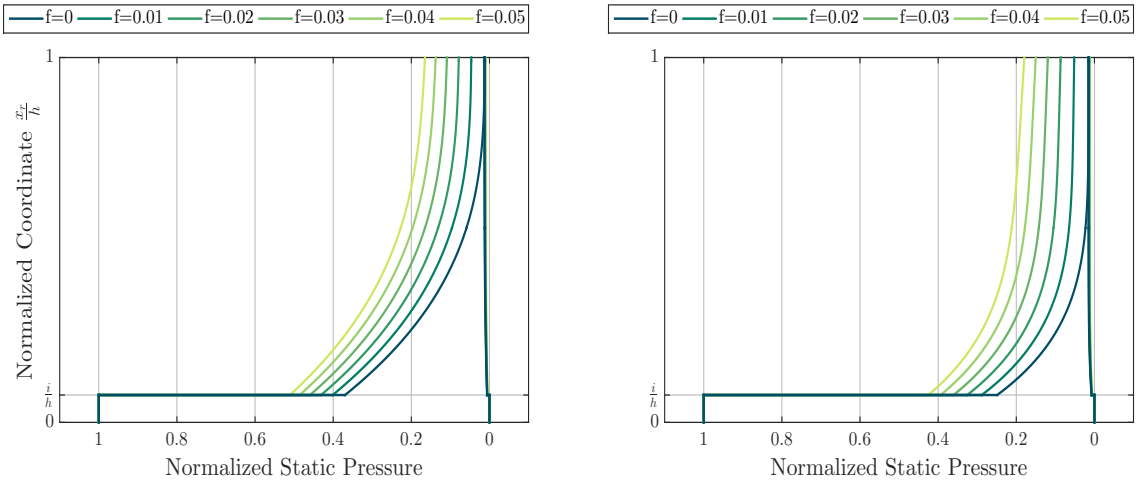

a: $\zeta_1 = 0$ b: $\zeta_1 = 0$

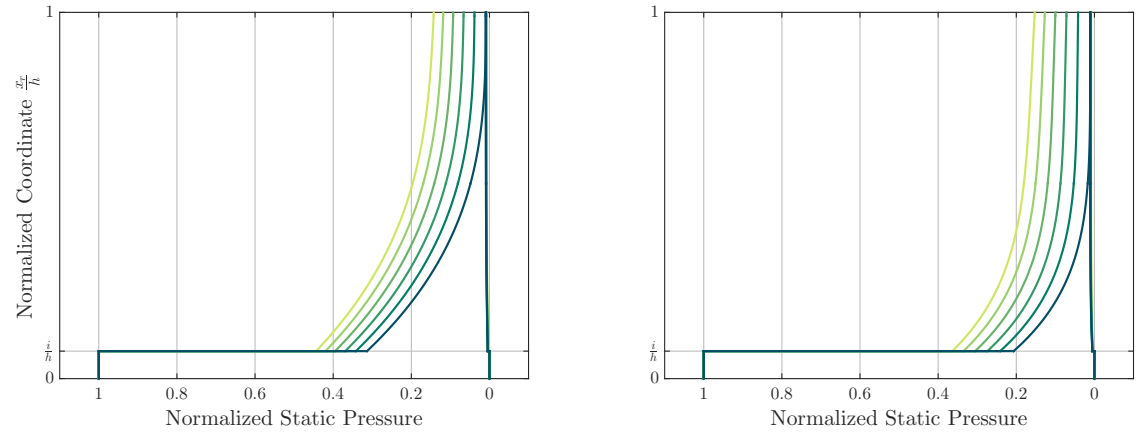

c: $\zeta_1 = 0.5$ d: $\zeta_1 = 0.5$

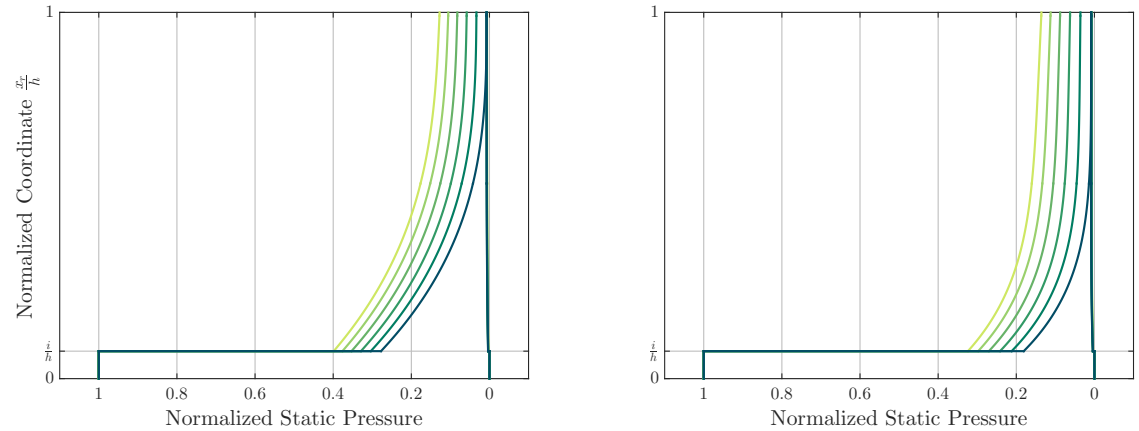

e: $\zeta_1 = 1$ f: $\zeta_1 = 1$

Figure 3.7: Parameter study 3, $\zeta_2 = 1$, $\frac{s_{HP}}{s_{LP}} = 1$, with mixing losses

Chapter 4

Results and Comparison of Pressure and Leakage

In this chapter, the calculations are made for the seal design presented in [2]. The parameters are shown in Tab. 4.1. The value of the inlet resistance coefficient $\zeta_1 = 0.4$ is within the range

Geometric Parameters			
Seal outer radius	R_o	195	mm
Seal inner radius	R_i	175	mm
Slope angle	α	37.5	$^\circ$
Attachment angle	β	45.4	$^\circ$
Seal width	w	5	mm
Leaf thickness	d	70	μm
Tip gap width	c	8	μm
Base gap width	b	30	μm
Number of leaves	n	8581	$-$
Side plate tip gap height	i	1.5	mm
High pressure side gap width	s_{HP}	0.05	mm
Low pressure side gap width	s_{LP}	0.15	mm
Radial interference	w	0.6	mm
Sealing height[1]	h	20	mm
Side plate height[1]	l	18.5	mm
Flow Parameters			
Outlet pressure	p_1	1	bar
Inlet pressure	p_0	1∼4	bar
Temperature	T	293.15	K

Table 4.1: Parameters taken from [2]

of an annular orifice, [22], although the exact value is depending upon the Reynolds number. The outlet resistance is included in the model. However, the pressure distribution published in [25] show a very small pressure drop at the outlet. Therefore the outlet coefficient is set to $\zeta_2 = 0$.

As in [2], air is used as fluid. The physical properties density, using the equation of state

[1]These are derived parameters, which are not given in [2], however can easily be calculated.

for ideal gases,

$$\rho = \frac{p}{RT} \tag{4.1}$$

with

$$R = 287.058 \frac{J}{kgK} \tag{4.2}$$

is calculated with the average pressure

$$p_m = \frac{p_1 + p_0}{2} \tag{4.3}$$

and dynamic viscosity

$$\eta = 1.458 \cdot 10^{-6} \frac{T^{3/2}}{T + 110.4K}. \tag{4.4}$$

is calculated using a formula taken from [22]. The reference pressure for Eqn. (4.4) is $1bar$.

Beside the prior mentioned assumption, also the following are made:

- No fluid structure interaction
- No leaf deflection
- No variations in leaf to leaf geometry due to manufacturing

4.1 Control of Radial Velocity and Reynolds number

To test the velocity gradient hypothesis in the side plate gaps, the mass balance

$$c_r(x_s) s_{HP} \rho 2 R_i \pi = \dot{m}_{SP} - \int_i^{x_s} c_a(\delta) s(\delta) \rho n d\delta \tag{4.5}$$

is used. In this equation c_{HP} is not used, because it is mainly a reference speed for the calculation of the pressure distribution. It has only a small correlation to the leakage, since no information about the leaf pack is found in its derivation of the pressure distribution model. The radial velocity in the side plate gap is therefore

$$c_r(x_s) = \frac{1}{s_{HP} \rho 2 R_i \pi} \left(\dot{m}_{SP} - \int_i^{x_s} c_a(\delta) s(\delta) \rho n d\delta \right). \tag{4.6}$$

This velocity is then set into relation to its maximum value. Only the high-pressure side is taken into account, since the low-pressure side has the same gradient only modified by the ratio of the side plate gap widths and the mixing term. The normalized velocity

$$c_{r,norm}(x_s) = \frac{c_r(x_s)}{c_{r,max}} \tag{4.7}$$

can then be compared with the assumed distribution. In Fig. 4.1 a sample control plot is shown, for different exponents the plots are shown in Fig. A.1 and Fig. A.2. For higher exponents the difference between assumption and control calculation gets less.

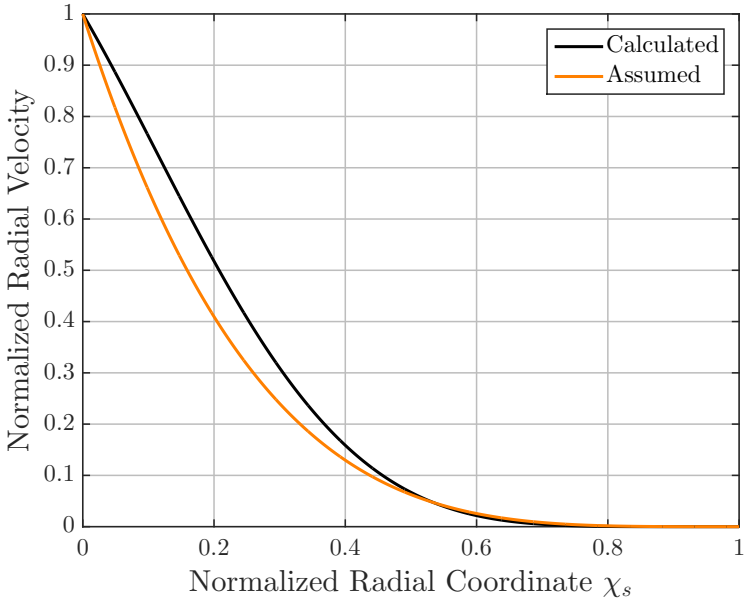

Figure 4.1: Assumed and calculated radial velocities for $n = 4$ and $f = 0$

Using the radial velocity in the side plate area, the Reynolds number

$$Re_r(x_s) = \frac{\rho c_r(x_s) 2 s_{HD}}{\eta} \tag{4.8}$$

is calculated. These are shown in Fig. 4.2 and in Tab. 4.2 the maximum Reynolds numbers for different exponents are listed.

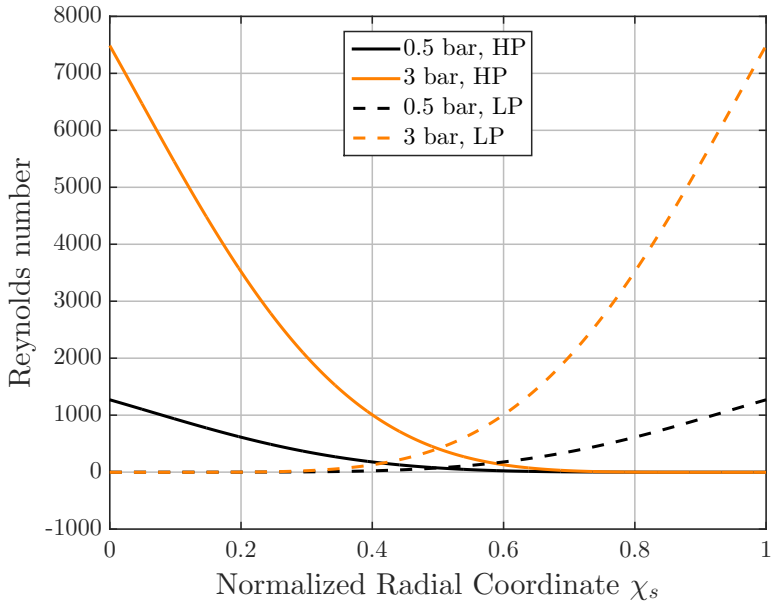

Figure 4.2: Reynolds number distributions in the side plate areas for $n = 4$ and $f = 0$

The values for the high-pressure side plate gap and the low-pressure side plate gap are identical, because the Reynolds number uses the side plate gap width as specific length. The high-pressure side and low-pressure side are linked with the mass balance and therefore the radial velocity in

Exponent	Re_r	
n	$0.5bar$	$3bar$
1	5161	43144
2	2887	20352
3	1807	11341
4	1220	7068
5	871	4766
6	648	3405

Table 4.2: Comparison of radial Reynolds numbers

the side plate gaps are linked with the side plate gap widths.

The critical Reynolds number for rectangular ducts is between 2000 and 4000, [22], in comparison to 2320 for pipes. However, in comparison to common rectangular duct on one side, there is the leaf pack and therefore no smooth surface. Also, the drain and influx are deviations of the common pipe model. Especially for higher pressure differences and the influx side, the assumption of laminar flow is very uncertain.

In [2] are plots of interleaf gap velocities for two pressure differences and two sealing heights in the middle of the leaf pack. These plots show a parabolic distribution and the maximum can be determined. Ortner writes, these distributions are slightly shifted to the right side, meaning the underside of the leaf. Also, the velocity graphs show higher velocities for the inflow and outflow of the leaf pack. Unfortunately, these graphs only show the magnitude of the velocities and not the vectors. Therefore, these plots can not be used, to estimate the ratios between the axial, radial and circumferential components of the velocity vector. However, the parabolic values are still used for comparison.

First, a division by 2 of the velocities simulated in [2] is necessary, to make it comparable with the analytical model. This is the factor between average and maximum speed for a parabolic velocity distribution, [22]. The velocities in Tab. 4.3 are calculated for the MHI design using the coefficient

$$f = 0. \tag{4.9}$$

For both pressure differences and all exponents, the calculated velocities in the look through area ($x_r = 0.75mm$) are far higher than those computed using CFD. In the leaf pack ($x_r = 14mm$) the velocities nearly match for the exponents $n = 3$ and 4. One reason for this deviations can be the flow deflection at the leaf tip described in [16]. This reduces the leakage mass flow rate at the tip compared to the assumption of unvarying axial flow in the whole leaf pack.

$\Delta p_{tot}[bar]$	$x_r[mm]$	$c_r[\frac{m}{s}]$			
		CFD [2]	$n=1$	$n=2$	$n=3$
0.5	0.75	$5,0/2=2.5$	9.0466	8.4578	7.8430
0.5	14	$0,79/2=0.395$	5.7101	1.7181	0.5121
6	0.75	$47,5/2=23.75$	54.7214	42.3000	35.0705
6	14	$4,4/2=2.2$	34.5395	7.8496	1.9466
		CFD [2]	$n=4$	$n=5$	$n=6$
0.5	0.75	$5,0/2=2.5$	7.2616	6.7360	6.2701
0.5	14	$0,79/2=0.395$	0.1524	0.0454	0.0136
6	0.75	$47,5/2=23.75$	30.3704	27.0773	24.6440
6	14	$4,4/2=2.2$	0.0.5125	0.1403	0.0394

Table 4.3: Comparison of axial velocities for $f=0$

4.2 Pressure Distribution

The plots of static pressure distributions calculated with the analytic model can be compared with the plots in [25]. These plots use the static pressure $0.01mm$ within the porous media on the upstream side and $0.01mm$ before the exit on the downstream side. The comparisons of the analytical plots and the results from [25] are shown in Fig. 4.3 and Fig. 4.4.

In the case of $0.5bar$ differential pressure, the analytic model has some correlation with the porous media model using exponents $n=2$ to 5. The overall trend matches, however pressure differences of the leaf pack show a much higher gradient. For considerations regarding the leakage mass flow rate, as discussed in the next section, this could lead to an underestimation of the leakage mass flow rate at the leaf base. For incompressible flows only the pressure differential is important, the absolute pressure has no influence.

For higher exponents, the pressure loss on the high-pressure side is higher and on the low-pressure side lower, resulting in a lower static pressure at the leaf base and a lower average pressure. This could mean that for the calculation of the deflection due to the static pressure distribution, the use of smaller exponents is more appropriate.

Variations of the inlet resistance coefficient show almost no effect on pressure on the leaf base. For a pressure differential of $3bar$ the model is far less compliant. One reason is the compressible behaviour of the porous media approach, which can not be reproduced with the analytic model. Another problem is the dependency of the pressure losses in the side plate gaps on the upstream and downstream side. Eqn. (3.28) and Eqn. (3.29) without the mixing term on the low-pressure side and $f=0$ can be used to calculate the ratio

$$\frac{\Delta p_{SP,LP}(1)}{\Delta p_{SP,HP}(1)} = \frac{\frac{s_{HP}}{s_{LP}^3}}{\frac{1}{s_{HP}^2}} = \left(\frac{s_{HP}}{s_{LP}}\right)^3 = v^3 \tag{4.10}$$

of the pressure losses. Due to the model prerequisites, the ratio is the same for every exponent. Further the inlet resistance is dependent upon the pressure difference, which has direct influ-

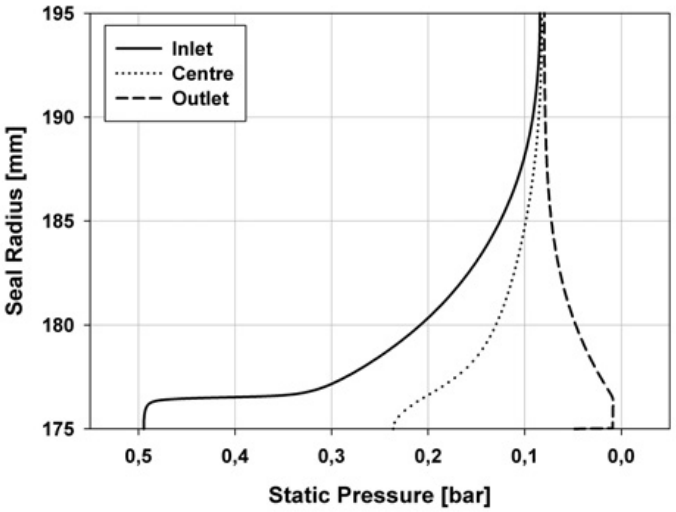

a: Porous media [25]

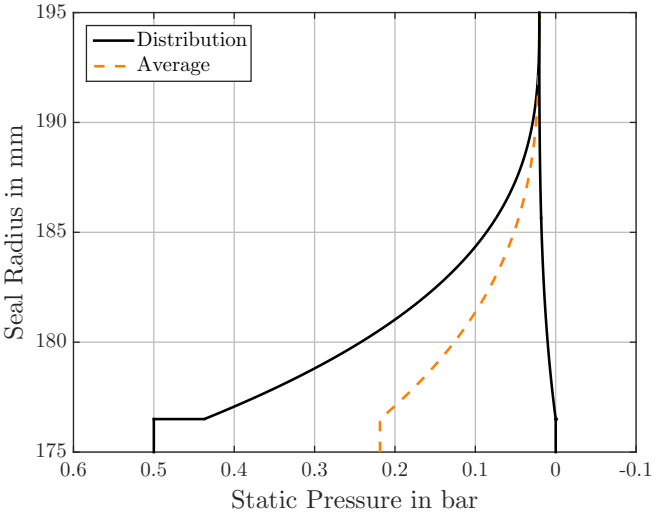

b: $n = 2$ and $f = 0$

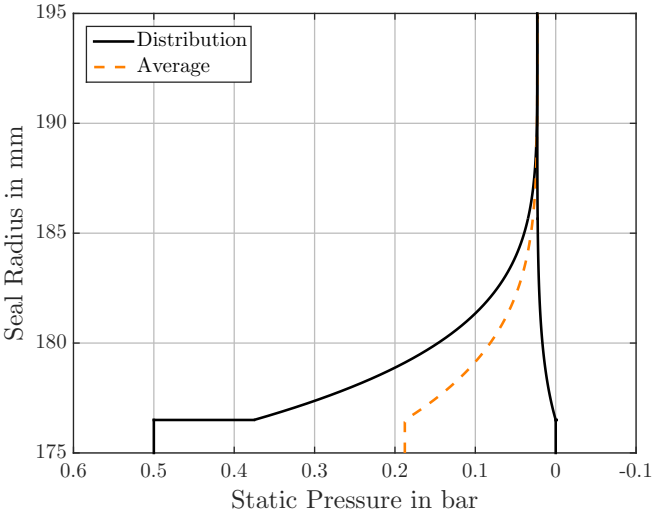

c: $n = 4$ and $f = 0$

Figure 4.3: Comparison of pressure distributions, $0.5bar$ pressure difference

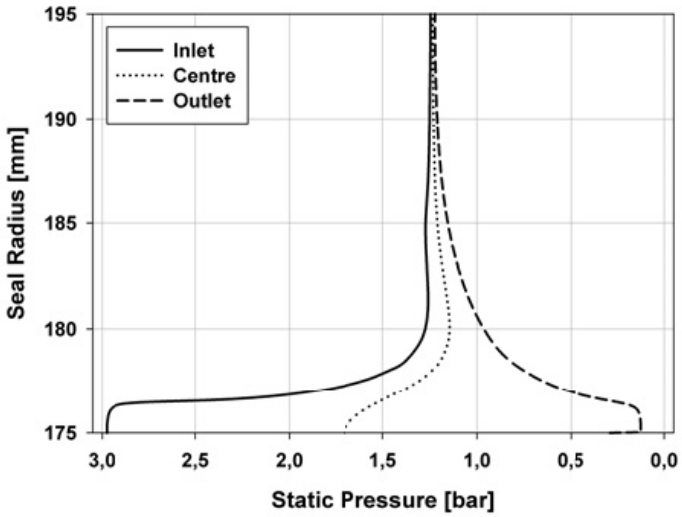

a: Porous media [25]

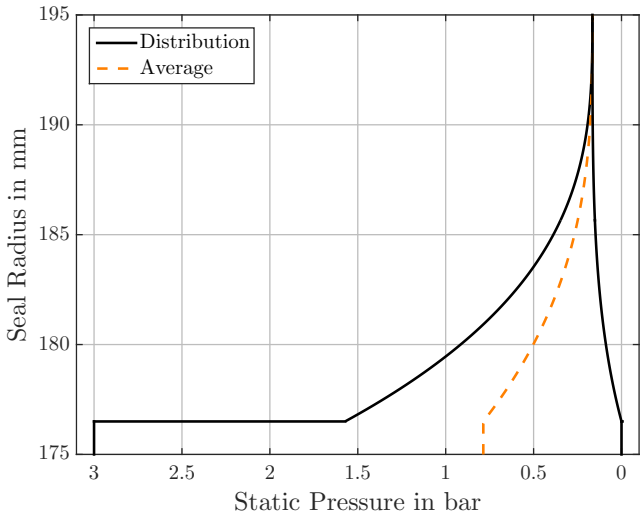

b: $n = 2$ and $f = 0$

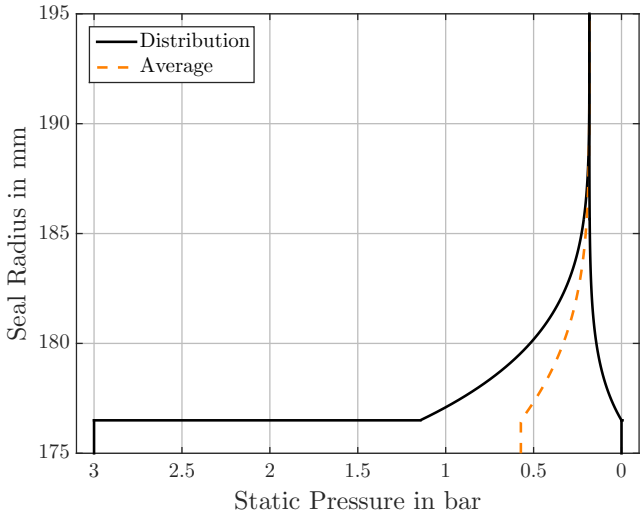

c: $n = 4$ and $f = 0$

Figure 4.4: Comparison of pressure distributions, 3*bar* pressure difference

ence on the inlet velocity. This is in accordance with tables in [22], where the coefficients are dependent upon the Reynolds number.

A manual fitting for the analytical model with exponent $n = 4$ and $f = 0$ for the $3bar$ model has the best correlation with

$$\zeta_1 = 0,\ \zeta_2 = 2 \tag{4.11}$$

shown in Fig. 4.5.

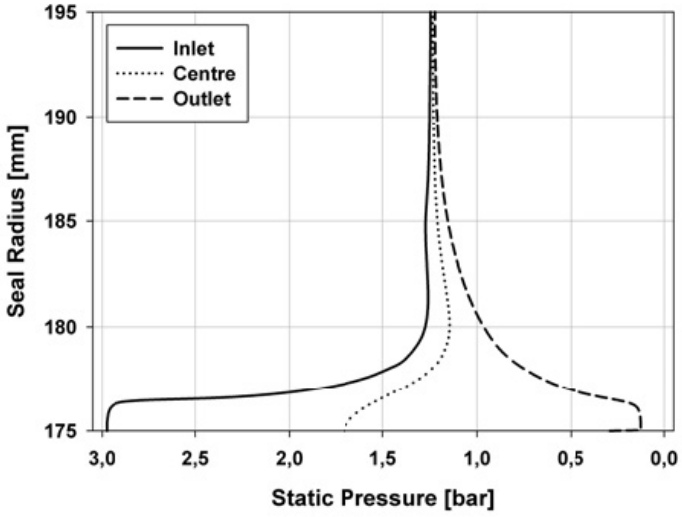

a: Porous media [25]

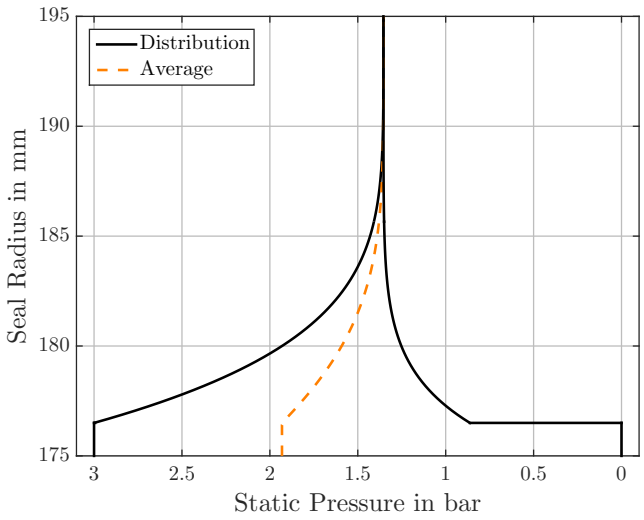

b: Fitted with $n = 4$ and $f = 0$

Figure 4.5: Comparison of pressure distribution, $3bar$ pressure difference, fitted model

This approach is not pursued, because the aim of this thesis is to find an analytical model. Therefore, as little empirical values as possible should be used. Also, this would bring more uncertainty, because there is not much data to compare with.

In [25] variations of the MHI-seal only regarding the side plate gap widths are made. These

side plate gap widths are listed in Tab. 4.4. For each one, the drain/influx factor was adjusted

Model	$s_{HP}[mm]$	$s_{LP}[mm]$	Ratio $\frac{s_{LP}}{s_{HP}}$
I	0.10	0.10	1.00
II	0.10	0.15	1.50
III	0.15	0.05	0.33
IV	0.20	0.15	0.75

Table 4.4: Gap widths, taken from [25]

using the pressure distribution calculated in [25]. These figures can be seen in Fig. A.3 and Fig. A.4. Only for Model 3 a good match is found, shown in Fig. 4.6. For the others the pressure loss on the downstream side is too small. Again, the coupling of the upstream and downstream pressure loss is a disadvantage.

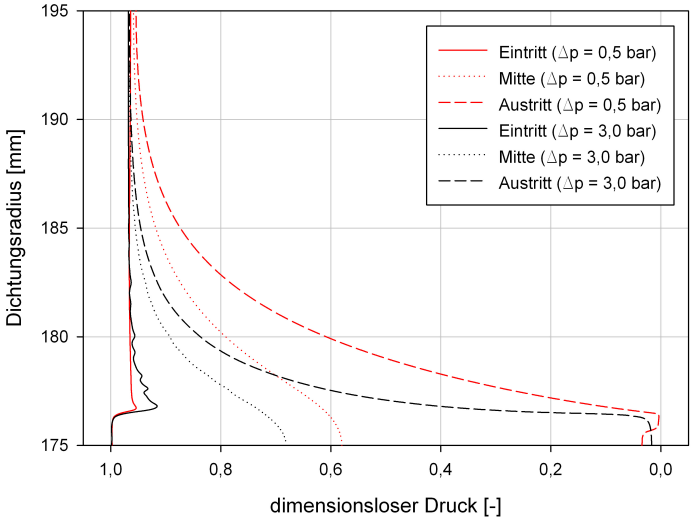

(a) Porous media [25]

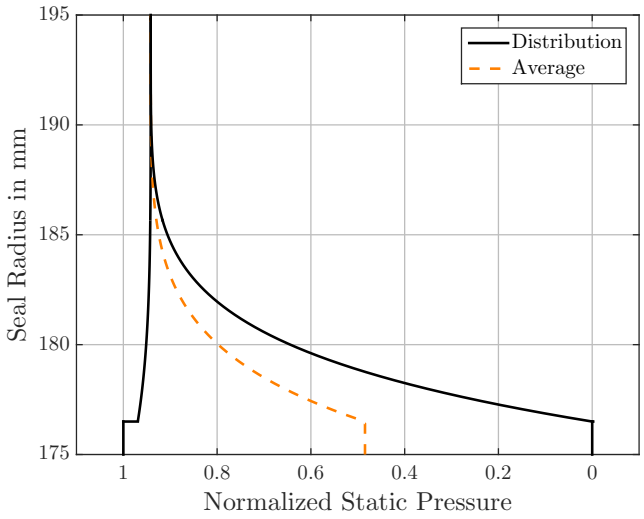

(b) Analytical, $n = 4,\ f = 0,\ \Delta p = 0.5bar$

Figure 4.6: Pressure distributions of Model 3

4.3 Leakage Mass Flow Rate

For validating the leakage mass flow rate, more sources are available. For better comparison, the leakage mass flow rate from Eqn. (3.63) is multiplied by the number of leaves n_L

$$\dot{m}_{tot} = \dot{m}_L n_L \tag{4.12}$$

and scaled to $[\frac{kg}{h}]$, as this dimension is used by most authors. In Fig. 4.7 the analytical data, the measured data from [23] and the simulation results from [2] and [25], are shown.

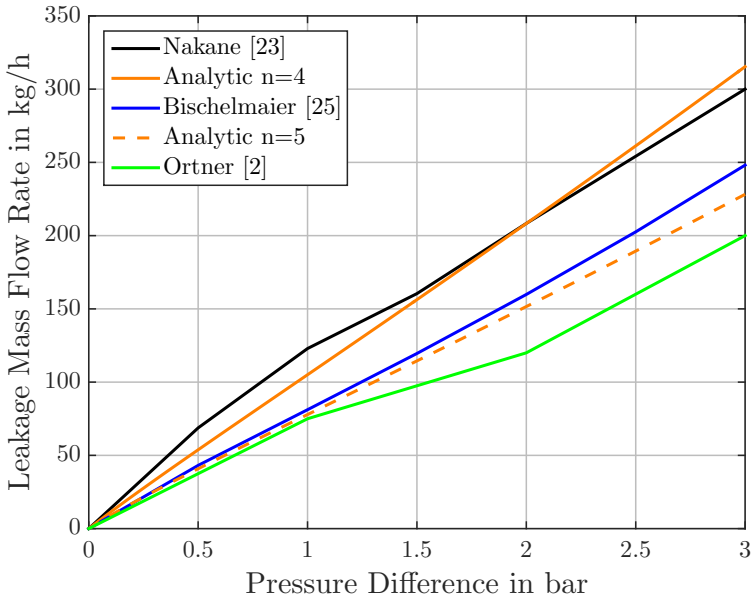

Figure 4.7: Comparison of leakages

The analytical leakage mass flow rate is shown for an exponent of 4 and 5. For $n = 4$ there is good agreement with the publication of Nakane et al. [23], for $n = 5$ with the simulations from [25]. The distribution between the portion of the leakage mass flow flowing through the look-through area and the side plate gaps is listed in Tab. 4.5. For higher exponents the leakage mass

	$\Delta p_{tot} = 0.5bar$			$\Delta p_{tot} = 3bar$		
n	$\dot{m}_{tot}$ in $\frac{kg}{h}$	$\dot{m}_{LT}$ in %	$\dot{m}_{SP}$ in %	$\dot{m}_{tot}$ in $\frac{kg}{h}$	$\dot{m}_{LT}$ in %	$\dot{m}_{SP}$ in %
1	196.6	4.63	95.37	1643.0	4.60	95.37
2	114.5	7.43	92.57	809.0	7.57	92.43
3	75.3	10.48	89.52	475.4	10.81	89.19
4	53.8	13.58	86.42	315.4	14.13	85.87
5	40.9	16.59	83.41	228.2	17.35	82.65
6	32.6	19.38	80.62	176.3	20.31	79.69

Table 4.5: Total leakage, percentage in the look-through area and the side plate area

flow rate for the analytical model shifts towards the look-through area. This is in accordance with the pressure distributions. The distribution between the look-through and the side plate gaps changes with the exponent n - however, the pressure difference has almost no influence.

4.3.1 Reynolds Number of Axial Flow

Also, the flow in leaf pack is considered laminar, therefore this assumption has to be checked. As formula for the Reynolds number

$$Re_a(x_s) = \frac{\rho c_a(x_r) 2s(x_r)}{\eta} \tag{4.13}$$

is used. For this axial Reynolds number as well the gap width is a function of the radius.

Again, the limit for laminar flow is between a Reynolds number of 2000 and 4000. Therefore, as Fig. 4.8 shows, the assumption of laminar flow inside the leaf pack is correct. The peak of the Reynolds number curves moves from a little bit under the midst of the leaf pack with increasing exponents to the border between the look-through area and the side plate gaps.

4.3.2 Variations of MHI Design

To investigate the influence of different geometric parameters, variations of the original design are made. For every variation the radial velocity is controlled to assess the results. For a better overview and simpler comparison, the control plots of all designs are shown in the appendix in Fig. A.1 and Fig. A.2. In these figures it can also be seen, that for all variations $f = 0$ is assumed.

Side Plate Gap Width Ratios

The ratio of the side plate gap width is defined as

$$v = \frac{s_{HP}}{s_{LP}} \tag{4.14}$$

First, the high-pressure gap width was kept constant, only the ratios of v were changed. The calculated leakage mass flow rates are shown in Fig. 4.9. Even for wider low-pressure side gap widths than the original design, the leakage mass flow rate does not change significantly. Narrower gap widths leakage mass flow rates are only plotted to assess the trend of the formula. As previously discussed, the model can not be used to calculate the actual leakage mass flow rate for this side plate gap width ratios.

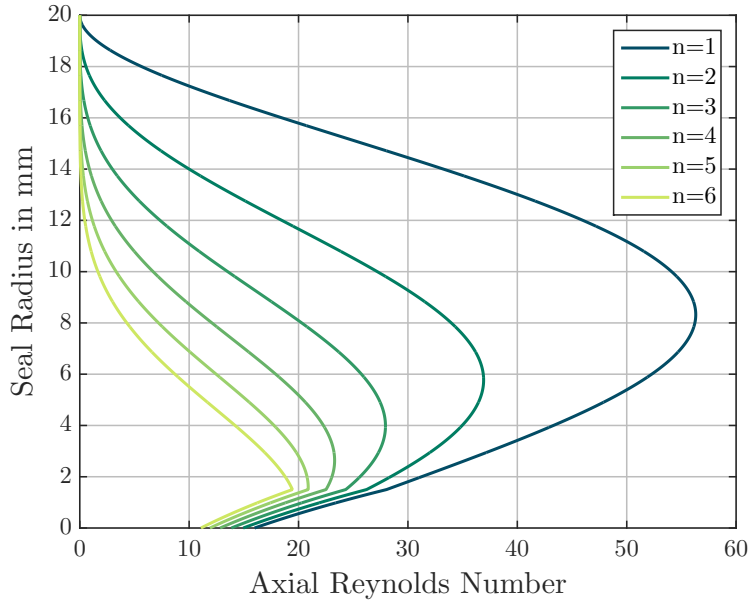

a: $\Delta p = 0.5bar$

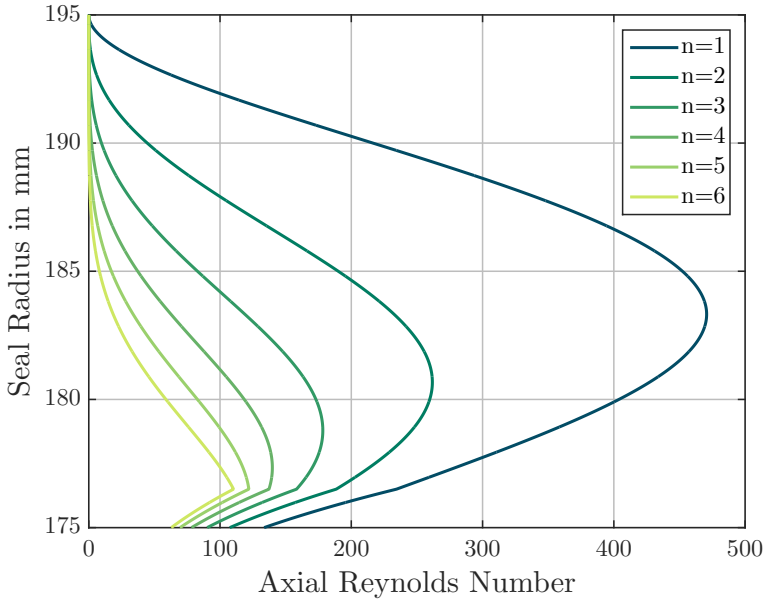

b: $\Delta p = 3bar$

Figure 4.8: Axial Reynolds numbers for pressure differences of $0.5bar$ and $3bar$

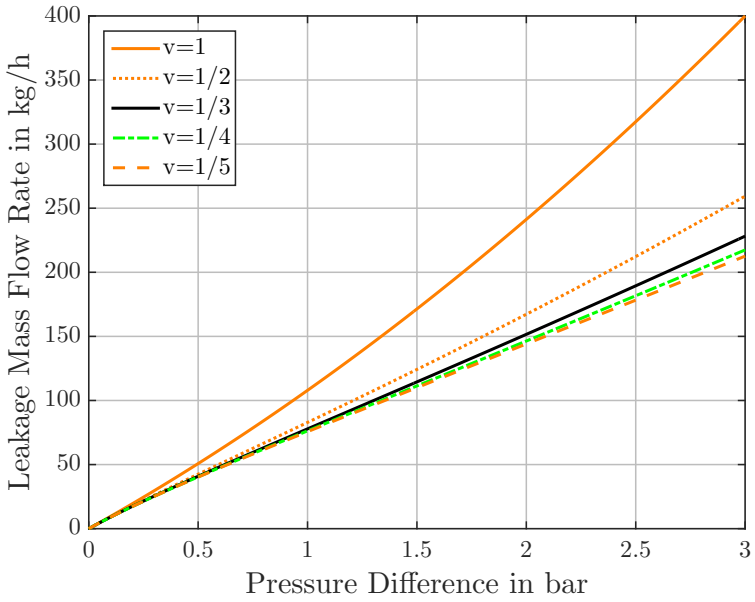

Figure 4.9: Variation of low pressure side plate width, $s_{HP} = 0.05mm = const.$, $n = 4$

The variation of the high-pressure side plate gap width with constant s_{LP} is shown in Fig. 4.10. Again, the ratio of $v = 1$ is plotted to assess the trend of the analytical function, it has the lowest leakage mass flow rate. For increasing as well as decreasing v the leakage mass flow rates increase. For low pressure differences, the MHI configuration has a higher leakage mass flow rate. At around $0.75bar$ (respectively $1.5bar$) this changes, and the leakage mass flow rate becomes the lowest next to $v = 1$.

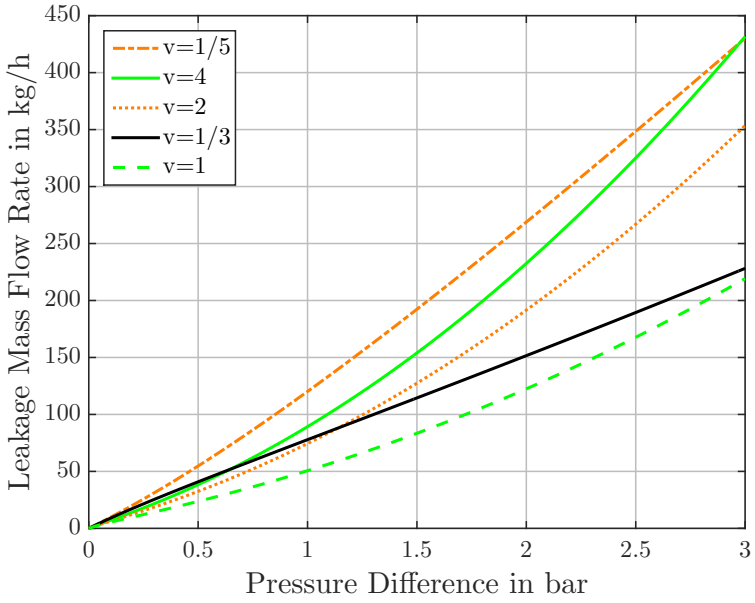

Figure 4.10: Variation of high pressure side plate width, $s_{LP} = 0.15mm = const.$, $n = 4$

Side Plate Tip Gap Height

The side plate tip gap height i is altered in $0.5mm$ steps. The results are shown in Fig. 4.11. For narrower gap widths, the leakage mass flow rate decreases, for wider an increase has been

calculated. For pressure differences higher than $0.5bar$, the ratios are almost constant. Disregarding other, linked effects, the side plate tip gap height should be as narrow as possible, yet, still ensuring non contact during rotor transients.

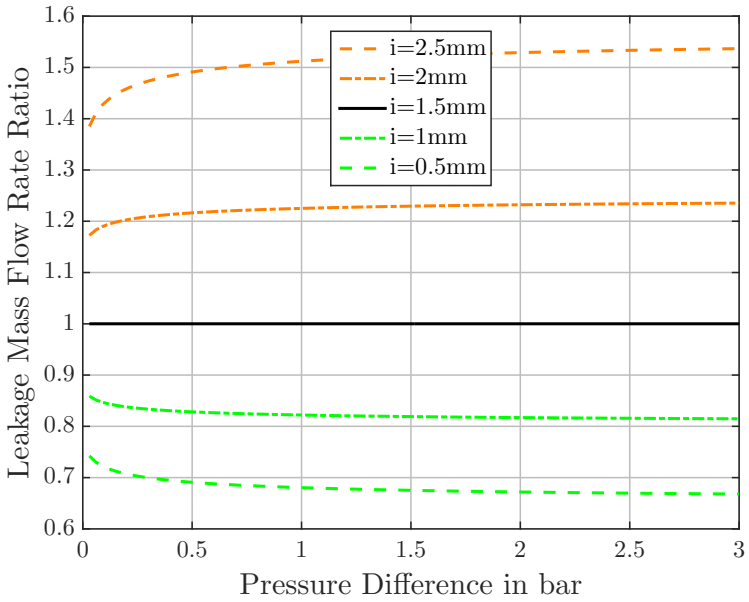

Figure 4.11: Variation of side plate tip gap height, $n = 4$

Number of Leaves

It is assumed, that the geometry of the leaves and leaf gaps are scaled by a factor of κ in the circumferential direction. Therefore the variation can be done analytically.

The dependency of the leakage mass flow rate

$$\dot{m}_{tot} \sim s^3 n \tag{4.15}$$

for the whole seal is of cubic form for the gap and of linear for the number of leaves. The leakage mass flow rate of the modified seal

$$\dot{m}_{mod} \sim s_{mod}^3 n_{mod} = \left(\frac{s}{\kappa}\right)^3 n\kappa = \frac{s^3 n}{\kappa^2} \tag{4.16}$$

is multiplied with $\frac{1}{\kappa^2}$. Therefore, a higher number of leaves with narrower gaps is one way to decrease leakage mass flow rate. However, thinner leaves lose radial rigidity and are more prone to larger deflections.

Tapered Leaves

In [26] a great number of different seal and leaf designs are patented. One of them are tapered leaves. For an assessment, the interleaf area

$$A_{IL} = \int_0^h s(x_r) dx_r = 0.5854 mm^2 \tag{4.17}$$

of the MHI design is calculated. For a gradually tapered leaf, this area is distributed equally over the sealing height, leading to a constant gap width of

$$s_{const} = \frac{A_{IL}}{h} = 0.02927mm \tag{4.18}$$

For the staged leaf design, a gap gradient in saw tooth shape with three peaks is chosen. The cross section A_{IL} and the tip gap

$$s(x_r = 0) = 0.0131mm \tag{4.19}$$

remain the same. The decision for linear growth of the gap is based upon the near linear growth of the original gaps. The maximum gap width

$$s\left(x_r = \frac{h}{3}\right) = s\left(x_r = \frac{2h}{3}\right) = \frac{2A_{IL}}{h} - s(x_r = 0) = 0.04544mm \tag{4.20}$$

is derived from the trapezoidal shape.

The resulting leakage mass flow rates are shown in Fig. 4.12.

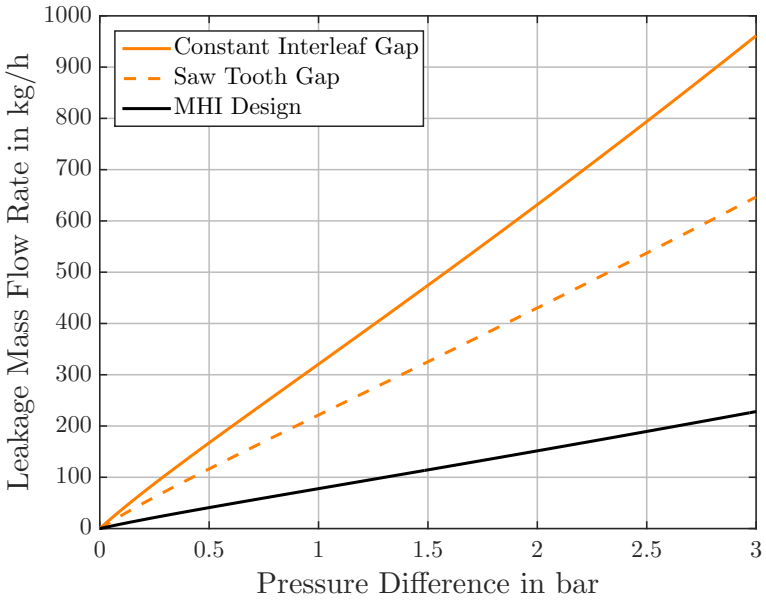

Figure 4.12: Comparison of interleaf gap variation leakage mass flow rates, $n = 4$

For both variations, the leakage mass flow rate is much higher. This is due to the cubic dependency from the leaf gap width and the wider gap at the leaf base, which can best be seen in Fig. 4.13. Based on this calculation, this leaf design can only be recommended, if the cross section is reduced accordingly. Especially at the leaf tip, the gap width should be as small as possible, if no other conditions, e. g. no interleaf gap contact for Lift Up configurations, have to be met.

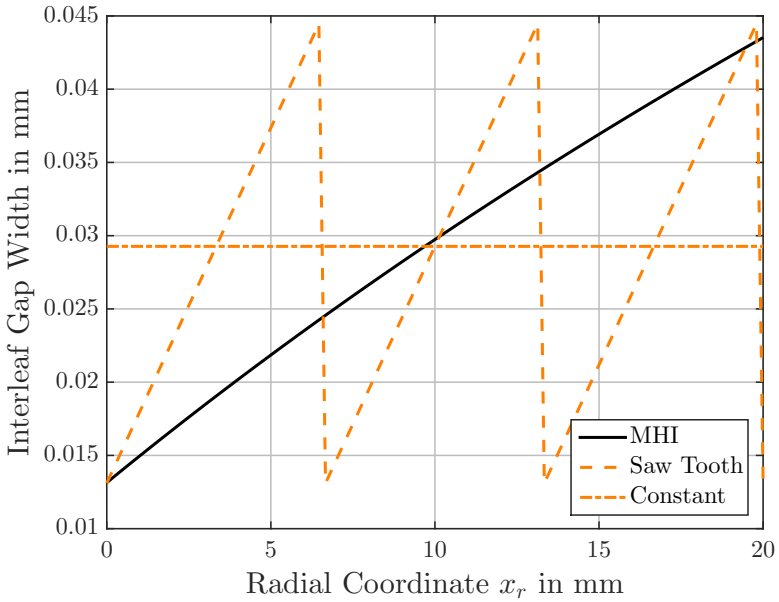

Figure 4.13: Comparison of interleaf gap width distribution

Variations from [25]

Leakage mass flow rate calculations are made for this variations. As discussed for the pressure distribution, only for Model 3 a correlation can be found. However, even for this variation the calculated leakage mass flow rate deviates increasingly for higher pressure differences, shown in Fig. 4.14.

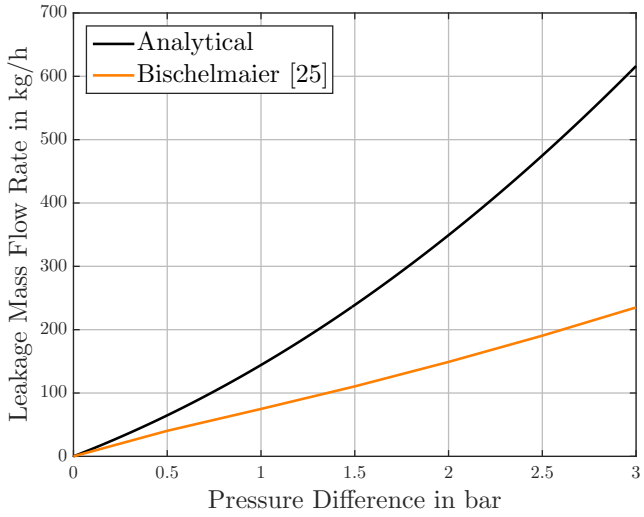

Figure 4.14: Comparison of leakage mass flow rates for Model 3

For the other variations, the ratios of the analytical value of the leakage mass flow rate to the simulated ones from [25], are even higher.

Chapter 5

Deflection of Leaves

In this chapter a deflection calculation of the leaves is presented. It uses the Euler-Bernoulli beam theory and considers the static pressure distribution and the possibility of shear stress due to Couette flow.

5.1 Static Pressure Distribution

As written in Ch. 2, the lay angle of the leaves is the condition for a deflecting force. The parametrisation of leaf geometry in cylinder coordinates is very difficult, so as an approximation the leaf pack is unrolled into a cartesian plane. For better visualization a drawing of these assumption is shown in Fig. 5.1. Again, the housing is shaded in blue, the leaf in yellow. The length of the leaf is calculated using the approximation of [12], however the angle $\phi(R_o)$ is calculated exactly using Eqn. (5.1) also found in [12].

$$\tan\alpha \sin\phi(r) - \cos\phi(r) + \frac{R_i}{r} = 0 \tag{5.1}$$

$$l(r,\phi) = \sqrt{r^2 - 2R_i r\cos\phi(r) + R_i^2} \tag{5.2}$$

$$L = l(R_o, \phi(R_o)) \tag{5.3}$$

Two different coordinates are used, one in radial direction, equal to x_r in the cylinder coordinate system and x_b in the direction of the beam model. These coordinates are linked through Eqn. (5.4).

$$x_b = L - \frac{x_r}{\sin\alpha_{\text{cor}}} \tag{5.4}$$

In Eqn. (5.4) a corrected version of the angle α is used. This is necessary, because of the unrolling into a plane, the leaves would get longer. On the other side, the equations for the averaged pressure are only valid for the original leaf pack height. Hence the adjustment in Eqn. (5.5) is used.

$$\alpha_{\text{cor}} = \arcsin\left(\frac{h}{L}\right) \tag{5.5}$$

Every point along the neutral axis has a corresponding pressure on the upper and lower surface. The thickness of the leaf constitutes for two different pressures in this point, because their radial coordinates differ by $\pm\frac{b}{2}\cos\alpha_{\text{cor}}$. Therefore, the load of the beam is the difference in pressure

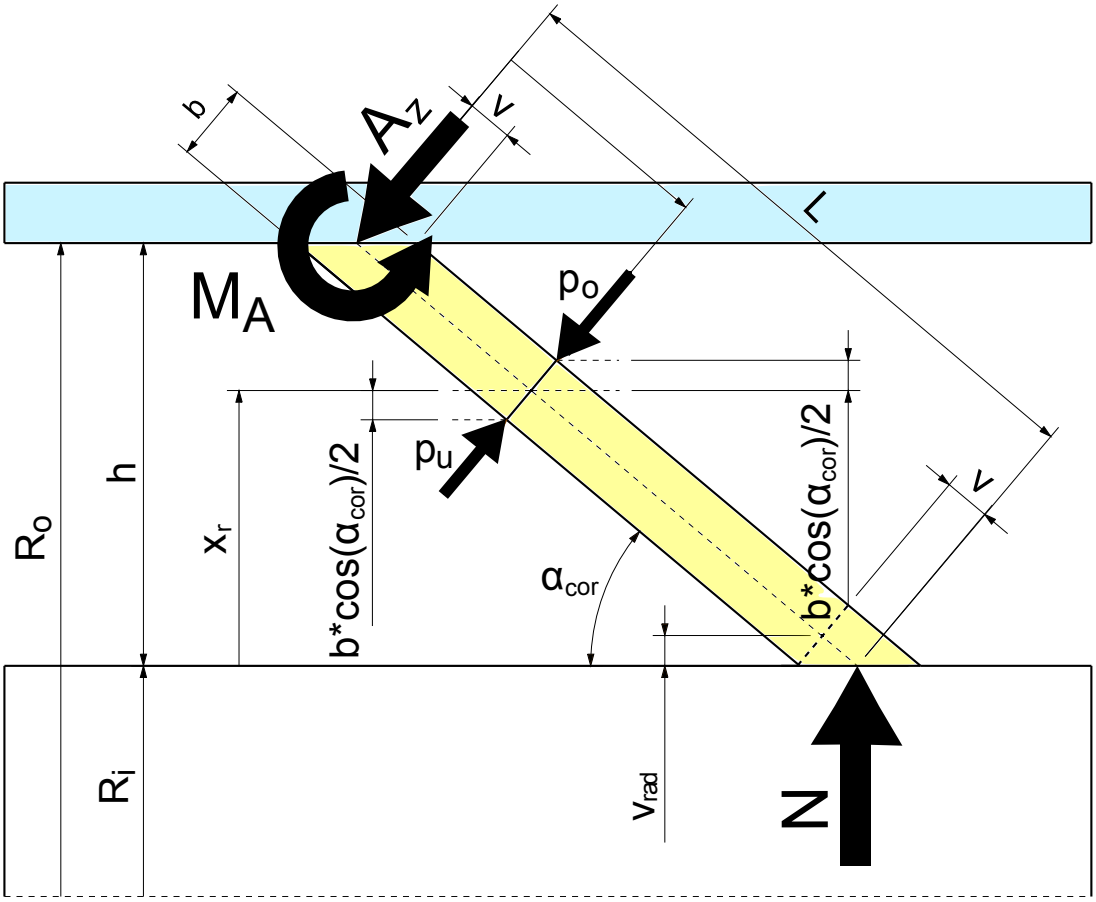

Figure 5.1: Drawing of the leaf as beam

of both sides multiplied by the width of the leaf. Eqn. (3.50) and Eqn. (3.52) are used as static pressure distribution.

$$\begin{aligned} q(x_b) &= w_L[p_o(x_b) - p_u(x_b)] = \\ &= w_L \left[p_m \left(x_r + \frac{b}{2} \cos \alpha_{\text{cor}} \right) - p_m \left(x_r - \frac{b}{2} \cos \alpha_{\text{cor}} \right) \right] \end{aligned} \tag{5.6}$$

5.1.1 Lift Up

For a Lift Up configuration of the side plate, the leaf is modelled as a cantilever beam with a single mount at the outer radius using the Euler-Bernoulli beam theory. Therefore, the contacting force N equals 0. The mounting force

$$A_z = -\int_0^L q(x_b) dx_b \tag{5.7}$$

is the integral of the load and the mounting moment is

$$M_A = -\int_0^L q(x_b) x_b dx_b. \tag{5.8}$$

The shear force

$$Q(x_b) = -A_z - \int_0^{x_b} q(x) dx \tag{5.9}$$

and the bending moment

$$\begin{aligned} M(x_b) &= \int_0^{x_b} \left(-A_z - \int_0^{x_b} q(x) dx \right) dx - M_A = \\ &= -\int_0^{x_b} A_z dx - \int_0^{x_b} q(x) d^2x - M_A = \\ &= -A_z x_b - \int_0^{x_b} q(x) d^2x - M_A \end{aligned} \tag{5.10}$$

are then calculated. The differential equation for the deflection

$$\frac{d^2 w_{LU}}{dx_b^2} = -\frac{M(x_b)}{EI} \tag{5.11}$$

is then solved using the boundary conditions

$$w_{LU}(x_b = 0) = 0, \ \frac{dw_{LU}}{dx_b}(x_b = 0) = 0 \tag{5.12}$$

for a cantilever beam fixed at one end

$$\begin{aligned} w_{LU}(x_b) &= -\frac{1}{EI} \int_0^{x_b} \int_0^{x_b} M(x) dx dx = \\ &= -\frac{1}{EI} \int_0^{x_b} \int_0^{x_b} \left(-A_z x_b - \int_0^{x_b} q(x) d^2x - M_A \right) dx = \\ &= \frac{1}{EI} \left(A_z \frac{x_b^3}{6} + \int_0^{x_b} q(x) d^4x + M_A \frac{x_b^2}{2} \right) \end{aligned} \tag{5.13}$$

5.1.2 Blow Down

For the Blow Down configuration two points of contact are assumed. The mounting at the outer radius and the rotor at the inner radius. Forces axial to leaf are considered negligible, so the Euler-Bernoulli beam theory can be used. The three assumed mounting forces are unknown, therefore the beam is statically indeterminate. Using the superposition principle, the beam system is split into two parts. System 1 consists of the mounting and distributed load, system 2 of the mounting and the rotor interference force normal to the leaf.

It has to be noted, that N_z, the component of N normal to the leaf's x axis, is reacting force, which cannot be directly observed as rotor interference force during operation. It is a substitute for the rotor interference force, the hydrodynamic lifting force and the force generated by momentum change. It is used to estimate the total amount of these forces.

The static equilibrium conditions for the beam in the direction of x_b

$$A_z - N_z + \int_0^L q(x_b) dx_b = 0 \tag{5.14}$$

and for the momentum

$$M_A + N_z L - \int_0^L q(x_b) x_b dx_b = 0. \tag{5.15}$$

For system 1 Eqn. (5.13) is used giving the deflection

$$w_{BD,1}(x_b) = \frac{1}{EI}\left(A_z \frac{x_b^3}{6} + \int_0^{x_b} q(x) d^4x + M_A \frac{x_b^2}{2}\right) \tag{5.16}$$

and for system 2 the common deflection for a mounted cantilever is

$$w_{BD,2}(x_b) = \frac{1}{EI}\frac{N_z L^3}{6}\left(3\left(\frac{x_b}{L}\right)^2 - \left(\frac{x_b}{L}\right)^3\right) \tag{5.17}$$

which can be found in engineering handbooks, e. g. [21]. The superposed deflections

$$w_{BD}(x_B) = w_{BD,1}(x_B) + w_{BD,2}(x_B) \tag{5.18}$$

are used to calculate the mounting forces and the mounting momentum and rotor interference force. The boundary condition

$$\begin{aligned} w_{BD}(x_B = L) &= \frac{g_r}{\cos\alpha_{\text{cor}}} = \\ &= \frac{1}{EI}\left(A_z \frac{L^3}{6} + \int_0^L q(x) d^4x + M_A \frac{L^2}{2} - N_z \frac{L^3}{3}\right) \end{aligned} \tag{5.19}$$

for the end of the beam is used together with Eqn. (5.14) and Eqn. (5.15) to solve the equation system. g_r is the radial gap between rotor and tip of the leaf, therefore it has to be divided by

$\cos\alpha_{\text{cor}}$ to use it in the deflection equation. The forces are then

$$A_z = -\frac{1}{2}\int_0^L q(x)dx + \frac{3}{2L}\int_0^L q(x)xdx - \frac{3}{L^3}\int_0^L q(x)d^4x + \frac{3g_rEI}{L^3\cos\alpha_{\text{cor}}} \tag{5.20}$$

and

$$N_z = \frac{1}{2}\int_0^L q(x)dx + \frac{3}{2L}\int_0^L q(x)xdx - \frac{3}{L^3}\int_0^L q(x)d^4x + \frac{3g_rEI}{L^3\cos\alpha_{\text{cor}}} \tag{5.21}$$

and the momentum is

$$M_A = \frac{L}{2}\int_0^L q(x)dx + \frac{1}{2}\int_0^L q(x)xdx - \frac{3}{L^2}\int_0^L q(x)d^4x + \frac{3g_rEI}{L^2\cos\alpha_{\text{cor}}}. \tag{5.22}$$

5.2 Eccentric Rotor

In literature regarding leaf seals, the fact of negative stiffness is discussed. As this effect occurs during rotor excursions, the analytical model is applied to an eccentric rotor.

The rotor eccentricity

$$\epsilon = e\cos\Theta \tag{5.23}$$

is approximated using a cosine function with the constant e and the angle Θ. Therefore the side plate tip height

$$\begin{aligned} i_{ex} &= i - \epsilon = \\ &= i - e\cos\Theta \end{aligned} \tag{5.24}$$

and the corrected lay angle

$$\begin{aligned} \alpha_{\text{cor,ex}} &= \arcsin\left(\frac{h_{ex}}{L}\right) = \\ &= \arcsin\left(\frac{l + i_{ex}}{L}\right) = \\ &= \arcsin\left(\frac{l + i - e\cos\Theta}{L}\right) \end{aligned} \tag{5.25}$$

are also a function of the angle Θ.

Every leaf has its tip position specified by Θ. Therefore, every point along any leaf's axis can be described by the coordinate pair (Θ, x_b). Due to the lay angle, every leaf has a certain extent into the circumferential direction, specified by the coordinate $\phi(x_b)$. Therefore for every leaf the side plate tip gap changes for every point of the coordinate x_b, this is shown in Fig. 5.2. For the ease of understanding, not all variables are shown in comparison to Fig. 5.1. This leads to a potentially different pressure distribution for every point. However, for the pressure model used in this thesis, this dependency has no influence, because in the derivation for the pressure distribution the side plate tip gap has no influence. Therefore, only the portion at the end of the beam, where no acting forces occur, differ in length.

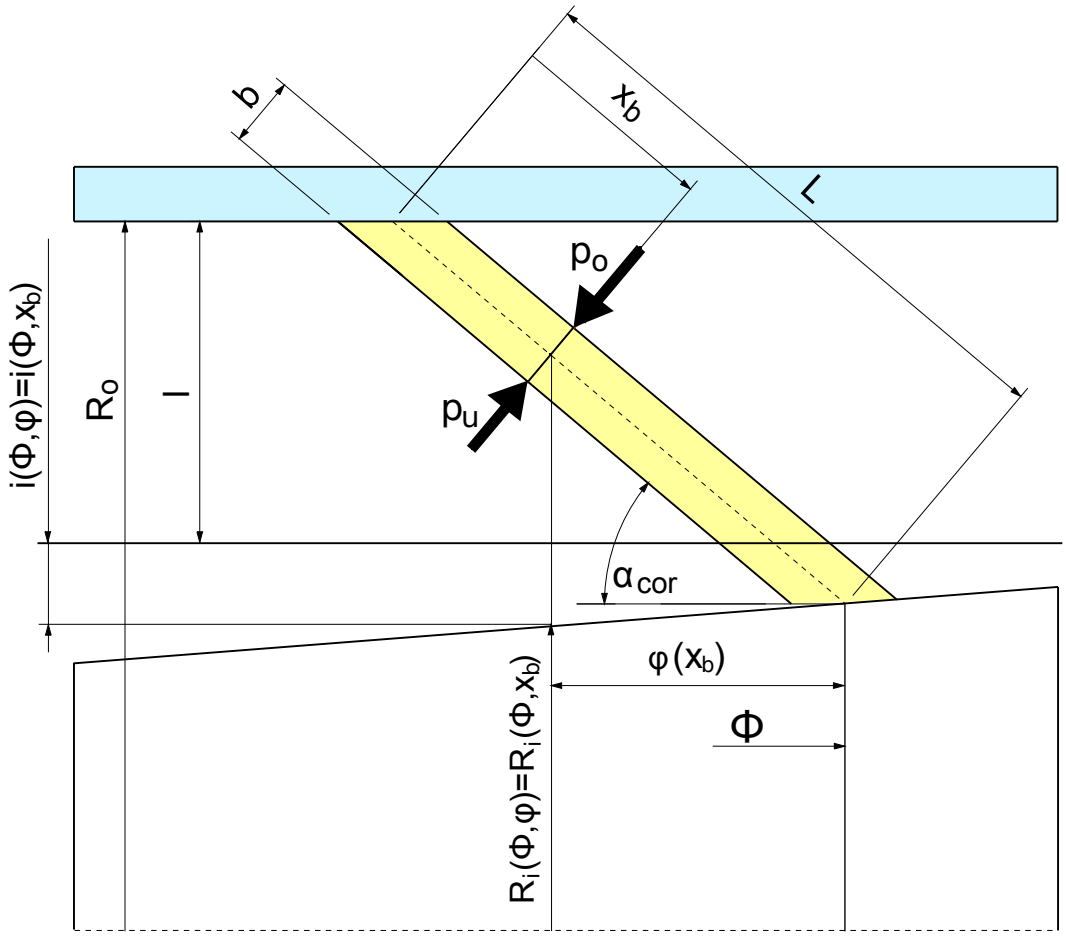

Figure 5.2: Geometrical leaf properties for eccentric rotor

5.3 Couette Flow

One approach for modeling the hydrodynamic lift force uses a laminar Couette flow. This was already undertaken at the department of Thermodynamik und Energietechnik at the Technische Universität Wien[1]. This approach is used again, however this time included into a comprehensive deflection model of the leaves. This basic calculations are made using [28].

The angular velocity of the rotor is

$$\omega = \frac{\pi n}{30}. \tag{5.26}$$

As dynamic viscosity the same value as for the pressure and leakage calculation is used. For $\frac{g_r}{R_i} \ll 1$, the shear rate can be simplified to

$$\dot{\gamma} = \frac{R_i + g_r}{g_r}\omega \approx \frac{R_i \omega}{g_r}. \tag{5.27}$$

For a Newtonian fluid the shear stress is

$$\tau = \dot{\gamma}\eta = \frac{u}{g_r}\eta = \frac{R_i\omega}{g_r}\eta = \frac{R_i \pi n}{30 g_r}\eta = \frac{F_s}{A_i} \tag{5.28}$$

with u as relative velocity, g_r the gap height, F_s the shear force and A_i the rotor surface. Therefore the shear force for the whole seal is

$$F_s = \frac{A_i R_i \pi n \eta}{30 g_r} = \frac{R_i^2 \pi^2 w_L n \eta}{15 g_r} \tag{5.29}$$

and for a single leaf, assuming no geometrical deviations,

$$F_{s,Leaf} = \frac{R_i^2 \pi^2 w_L n \eta}{15 g_r n}. \tag{5.30}$$

The torque for the whole sealing is

$$M_s = F_s R_i = \frac{R_i^3 \pi^2 w_L n \eta}{15 g_r}. \tag{5.31}$$

The component normal to the x axis of the leaf

$$F_{s,Leaf,\perp} = \frac{R_i^2 \pi^2 w_L n \eta}{15 g_r n} \sin\alpha \tag{5.32}$$

uses the non corrected angle α, because this force is derived from a cylindrical model. This force can be seen as part of N_z from the former section.

However, if all other forces contributing to N_z are neglected, a link between the radial gap and the rotational velocity can be found, $F_{s,Leaf,\perp}$ becomes N_z. Therefore Eqn. (5.21) can be

[1] personal conversation with Prof. Willinger

inserted in Eqn. (5.32), leading to a quadratic equation for the radial gap

$$Ag_r^2 + Bg_r + C = 0 \tag{5.33}$$

with

$$A = \frac{3EI}{L^3 \cos \alpha_{\text{cor}}}, \tag{5.34}$$

$$B = \frac{1}{2}\int_0^L q(x)dx + \frac{3}{2L}\int_0^L q(x)xdx - \frac{3}{L^3}\int_0^L q(x)d^4x, \tag{5.35}$$

and

$$C = \text{RPM}\frac{R_i^2 \pi^2 w_L \eta}{15 g_r n} \sin \alpha. \tag{5.36}$$

Chapter 6

Results of Deflection Calculations

For the calculation of loads and deflection the parameters from Tab. 4.1 are reused. As exponent $n = 2$ is chosen, due to the better compliance with the average pressure calculated in [25].

In this chapter the calculation starts with the static pressure distribution before the hydrodynamic forces are taken into account, due to the more uncertain nature of the later ones.

6.1 Load on the Leaves

The load on the leaves due to the static pressure distribution for the MHI design and Model 3 are shown in Fig. 6.1 and Fig. 6.2. Both have an almost triangular shaped distribution between the unloaded ends at the leaf base and the look-through area. Although Model 3 is the MHI design with exchanged side plate gaps, the load distributions are not mirrored. This is due to the asymmetric mixing loss on the downstream side. Model 1 has the anticipated behavior of a load indicating Blow Down also for symmetrical side plate gap width. Due to the model properties, the load at both ends of the leaf is zero. In Tab. 6.1 the mounting reactions for the MHI design and in Tab. 6.2 the mounting reactions for Model 3 are listed. For the MHI design

n	$0.5bar$		$3bar$	
	$A_z[N]$	$M_A[Nmm]$	$A_z[N]$	$M_A[Nmm]$
1	0.0087	-0.1632	0.0356	-0.6671
2	0.0081	-0.1714	0.0279	-0.5882
3	0.0075	-0.1691	0.0228	-0.5121
4	0.0069	-0.1624	0.0192	-0.4495
5	0.0064	-0.1541	0.0166	-0.3991
6	0.0059	-0.1455	0.0146	-0.3582

Table 6.1: Mounting forces and mounting momentum for MHI design

at $0.5bar$ as well as for $3bar$ the mounting reactions decrease with increasing exponent n. Model 3 shows a different behaviour. For $0.5bar$ the mounting reactions and the contact force increase with the exponent n. For a pressure difference of $3bar$ only the mounting force A_z increases, the mounting momentum M_A and the contact force N_z decrease with an increasing exponent.

In Fig. 6.3 and Fig. 6.4 loads for two other variants in side plate gap widths are shown.

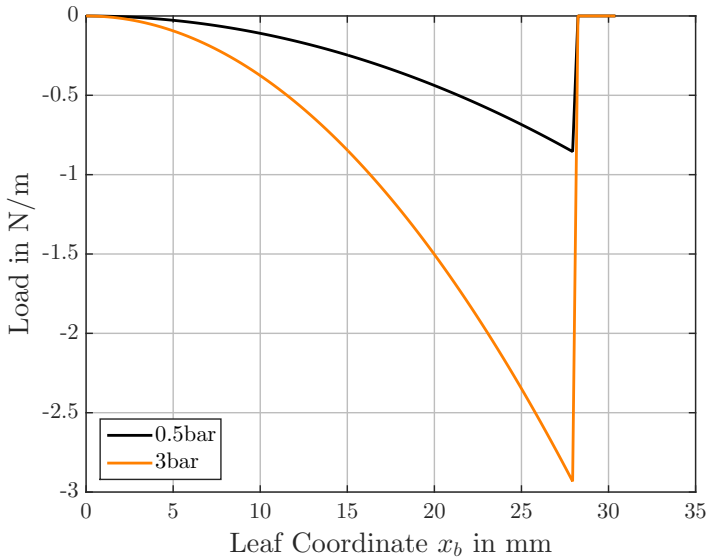

Figure 6.1: Load on a single leaf for $n = 2$ for the MHI design, $s_{HP} = 0.05mm$, $s_{LP} = 0.15mm$

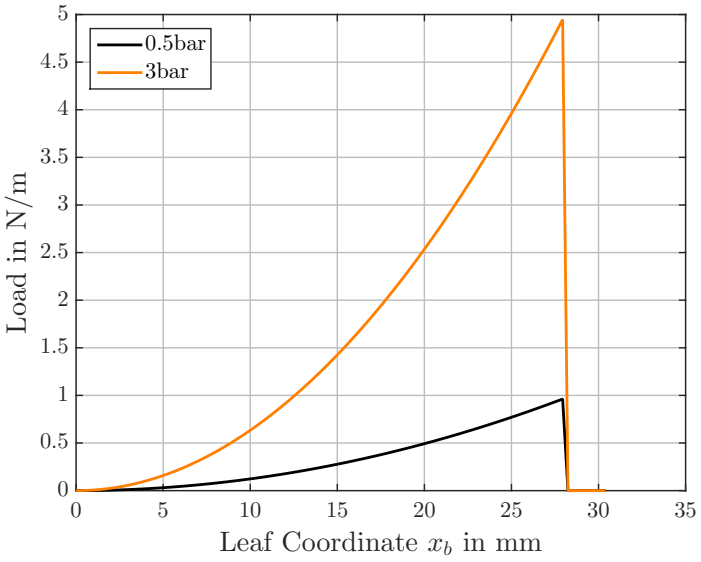

Figure 6.2: Load on a single leaf for $n = 2$ for Model 3, $s_{HP} = 0.15mm$, $s_{LP} = 0.05mm$

n	$0.5bar$			$3bar$		
	$A_z[N]$	$M_A[Nmm]$	$N_z[N]$	$A_z[N]$	$M_A[Nm]$	$N_z[N]$
1	0.0034	0.2103	0.0126	0.0188	0.0012	0.0699
2	0.0047	0.2266	0.0138	0.0239	0.0012	0.0710
3	0.0053	0.2334	0.0144	0.0253	0.0011	0.0682
4	0.0057	0.2356	0.0146	0.0251	0.0010	0.0641
5	0.0059	0.2351	0.0147	0.0243	0.0010	0.0599
6	0.0060	0.2330	0.0146	0.0231	0.0009	0.0559

Table 6.2: Mounting forces, mounting momentum and reacting forces for Model 3

Model 1 has the anticipated behaviour of a load indicating Blow Down also for symmetrical side

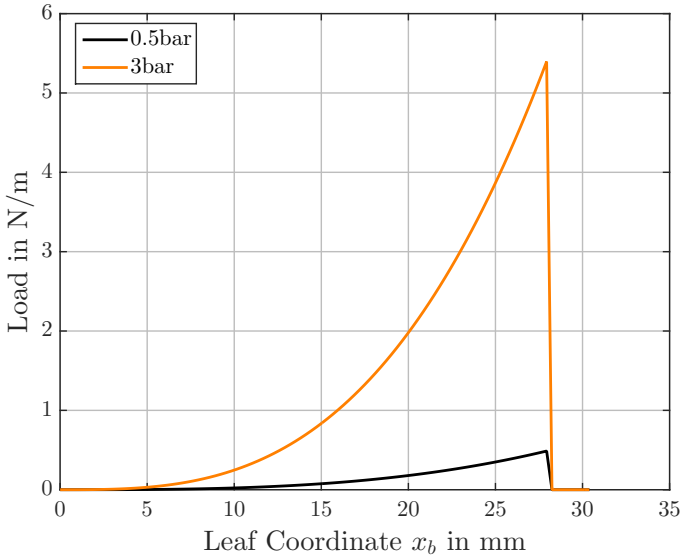

Figure 6.3: Load on a single leaf for $n = 2$ for Model 1, $s_{HP} = s_{LP} = 0.1mm$

plate gap width.

If the high pressure side plate gap width is reduced slightly to $s_{HP} = 0.07mm$, the load changes from Blown Down to Lift Up behaviour for a pressure difference of $0.5bar$. Therefore, even with this simple model, the change from Lift Up to Blow Down for increasing pressure differences as mentioned in [13] can be reproduced. However, the side plate gap widths have to be chosen accordingly.

6.2 Deflection

As Young's modulus a common value for stainless steel of $21GPa$ was chosen. The moment of inertia was calculated for a rectangular beam using the geometric values of the MHI seal. The results for the MHI design are shown in Fig. 6.5. In [23], the seal is contacting until the rotor reaches $n = 1500min^{-1}$. The deflection caused by the static pressure is of considerable amount. If these deflections would occur unchanged, the Euler-Bernoulli beam theory could not be used. Even at $0.5bar$ the lift is higher than the radial interference of $0.6mm$. Therefore the force

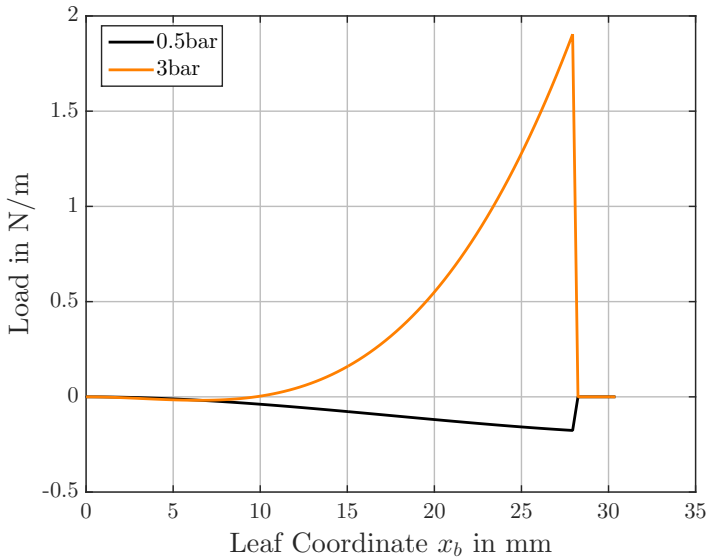

Figure 6.4: Load on a single leaf for $n = 2$ for $s_{HP} = 0.07mm,\ s_{LP} = 0.1mm$

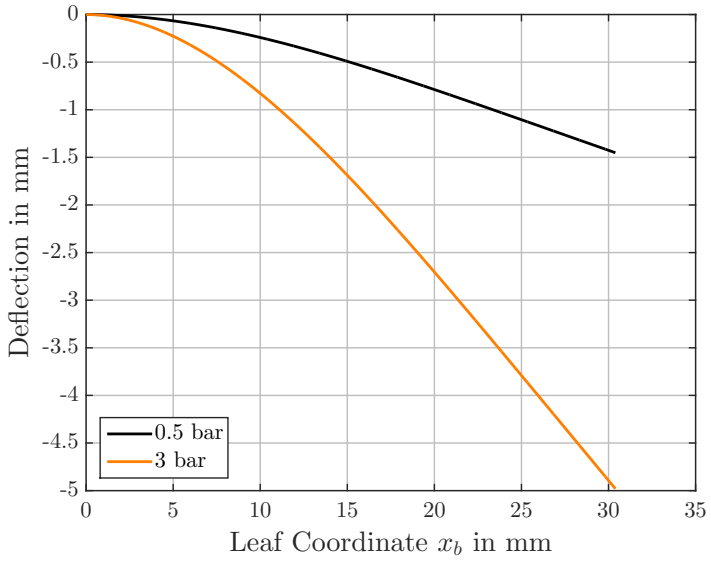

Figure 6.5: Deflection of a single leaf for $n = 2$ for the MHI design

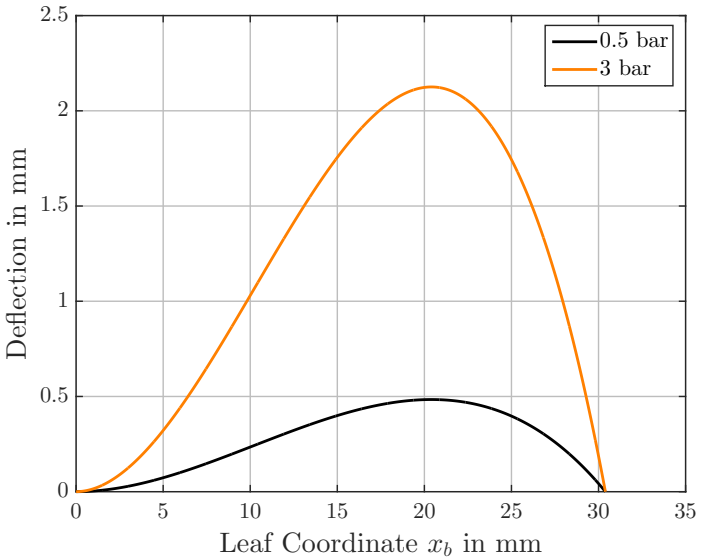

Figure 6.6: Deflection of a single leaf for $n = 2$ for Model 3

caused by the momentum change of the leakage flow when entering the leaf pack, discussed in [16], has to be responsible for the contacting operation.

Similar large deflections occur for Model 3, shown in Fig. 6.6. Again, these deflections are too big to allow the Euler-Bernoulli beam theory to be used. However, due to the Blow Down design, also rotor interference forces or hydrodynamic lift forces could counteract.

6.3 Eccentric Rotor

For assessment of the results of the eccentric rotor calculations, the side plate tip gap height i_{ex} is also shown. The value for the MHI seal is $i = 1.5mm$, therefore a larger side plate tip gap height is a displacement of the rotor away from the leaf pack and vice versa.

In Fig. 6.7 the tip deflections calculated for the MHI seal are shown. For the case of the rotor moving to the leaf pack, the side plate tip gap height decreases and the tip deflection increases. The explanation for this effect is the change in lay angle. The static pressure Lift Up or Blow Down increases with lesser lay angles. The same effect is shown in Fig. 6.8. Here, the contact force increases.

6.4 Couette Flow

The result of the deflection calculation for the Couette flow is shown in Fig. 6.9. The calculation was made for an unloaded leaf, $q(x_b) = 0$, due to the small force exerted. The gap is more than a magnitude to less compared to the blow down forces. This is compliant with the publication of Pekris et al. [11], which denied any significant force exerted by shear stress.

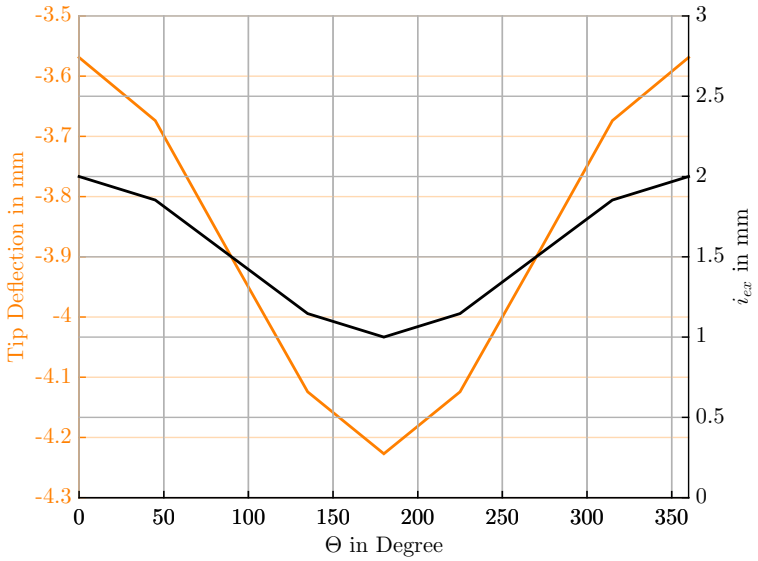

Figure 6.7: Tip deflection for eccentric rotor

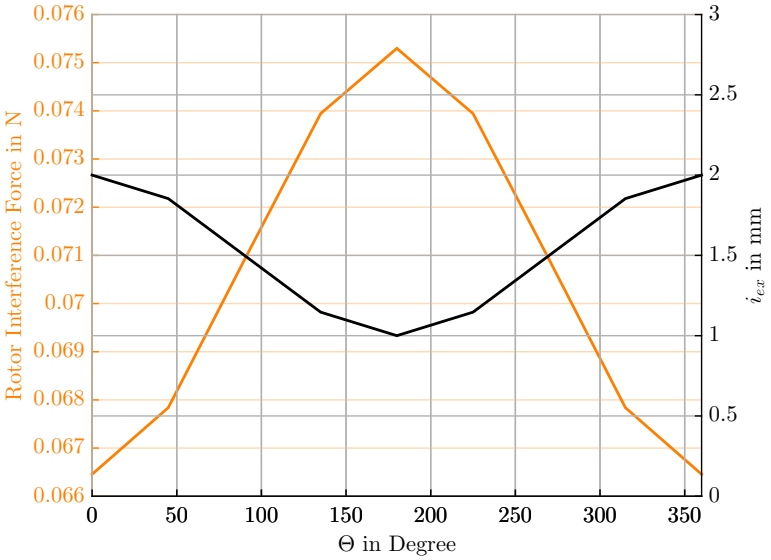

Figure 6.8: Rotor interference force for eccentric rotor

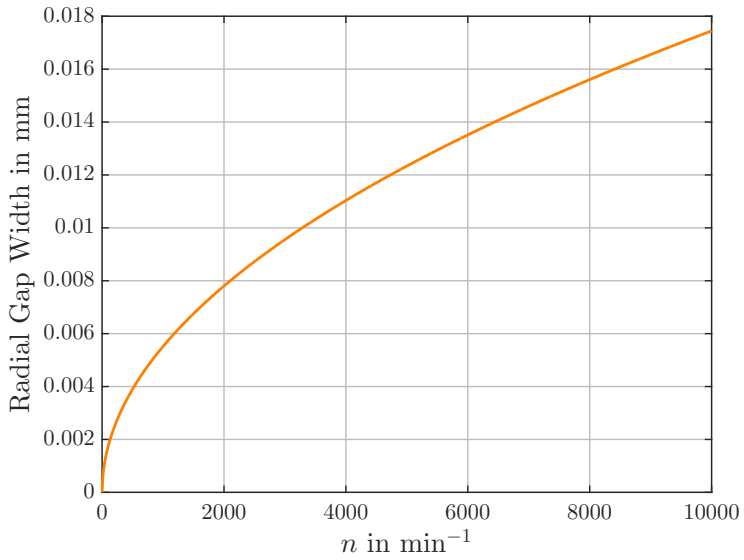

Figure 6.9: Radial gap caused by Couette flow on unloaded leaf

Chapter 7

Conclusion and Outlook

Almost two decades ago the research into leaf seals started. This seal design shows promising results for leakage reduction. However, the physical and operational behaviour has to be studied in depth before a usage in a power plant or an aircraft turbomachinery is possible. An introduction is provided summarizing all publications on the different topic regarding leaf seals.

In this thesis, an analytical pressure and flow model for leaf seals is presented. The seal is therefore split into different sections. Each one of them is modelled using pipe correlations. Therefore, the model is able to provide the static pressure distribution in the side plate gaps and on the leaves as well as the leakage mass flow rate and the distribution of the sealing mass flow rate along the sealing height. The static pressure distribution is coupled with deflection calculation for Lift Up and Blow Down configuration using Euler-Bernoulli beam theory. For the assessment of the model behaviour a parameter study is provided.

The last chapter will provide an overview of the results and difficulties of an analytical approach to leaf seal pressure and leakage flow properties. Unsuccessful attempts are mentioned as well as improvements for the model presented and recommendations for further research.

7.1 Conclusions

The model is able to provide static pressure distributions corresponding with the publication of Bischelmaier [25] for side plate gap width ratios with dominant Blow Down or Lift Up. This is achieved by modeling the side plate gaps using mass flow drain/influx and mixing losses on the low pressure side. Therefore, this effects are an important factor in the side plate gap flow for these configurations.

The leakage mass flow rate will be predicted right, when the exponent is set to $n = 4$ for the MHI design, although the pressure difference over the leaf pack is in this case less than the simulated one in [25]. For Model 3 the deviation is even greater, although the static pressure distributions are fitting well. Therefore, the assumption of unvarying axial flow seems to prohibit better results.

If the static pressure would act unopposed on the leaves, deflections will be of such magnitude, that Euler-Bernoulli beam theory is not applicable. It is shown, that Couette flow can not have an impact on hydrodynamic air riding, due to the small magnitude of force exerted.

To avoid further effort, the unsuccessful approaches have to be mentioned as well:

- *Expansion of one dimensional gas dynamics*
  Ortner [2] presented a model of the leaf seal using only one dimensional gas dynamics. Attempts were made to expand this model into two dimensions - however, to fully cover effects of axial, radial and circumferential flow, the mesh of flow resistances has to have the resolution of a coarse CFD mesh.

- *Plain bearing analogy*
  To model the hydrodynamic air riding an attempt was made using equations for the calculations of plain bearings. This idea is based upon the publication of Jahn et al. [14]. However, due to geometric properties of the leaf seal, large diameter compared to leaf width and thickness, common approaches of plain bearing theory can not be used.

7.2 Limitations of the Model

Due to the complex nature of leaf seal pressure distribution and flow field, simplifications have to be made for analytical modeling.

The calculations are made using the assumption of laminar flow. For the flow in the leaf pack, this seems applicable. However, control calculations show Reynolds numbers high enough for turbulent flow in the side plate gaps. The mixing of streams in the low-pressure side plate gap would favour turbulent flow as well. The assumption of unvarying axial flow through the leaf pack is a simplification. Especially for the leaf tip area it is questionable after comparison with [2]. The flow is also considered incompressible, therefore behaviour of compressible flow, which seem to occur even for low pressure differences [25], can not be reproduced.

The structure of the leaf seal is assumed to be static and "perfect", e.g. no rounded edges or imperfections due to manufacturing. Therefore, no coupled effects can be reproduced with this model.

The flows are modelled either axial or radial, any tangential components and therefore two and three dimensional flows are neglected. This leads to problems in predicting the leakage mass flow rate. It further prohibits calculations for forces acting on the leaves due to momentum change.

7.3 Recommendations for Further Research

- *Improvement of analytical flow model*
  A more detailed model could use variable fluid properties, in this case density and viscosity

instead of constant ones.
For pressure differences high enough to generate turbulent flow in the side plate areas other correlations have to be used.
If possible compressible flow models should be used, as the work of Bischelmaier [25] show effects of such flows even for low pressure differences.

- *Forces acting on leaves*
  Hydrodynamic forces caused by rotation as well as the force on the leaves due to momentum change of the leakage mass flow could be adequately modelled. For the later one the mass flow rate distribution over the sealing height is important. Therefore a CFD simulation would be advisable.

- *Fluid structure interaction*
  The forces acting on the leaves are changing the geometry of the leaf pack and therefore changing the flow field, resulting in a change of hydrodynamic forces. This system can have back coupling effects. This could lead to unstable operational behaviour, e. g. self exciting oscillations.
  During rotor excursions the circumferential leakage mass flow rate distribution can lead to effects on the rotor, e.g. Lomakin effect.

- *Large scale flow research*
  Similar to the experiments conducted by Franchescini et al. [15], the construction of a large scale test rig for leaf seals or filament seals in general could be useful. This would open the possibility to further investigate the flow properties and especially the influence of the high pressure and low pressure side plate gap on the interleaf flow and coupled effects such as aerodynamic forces on the leaves caused by a change in momentum.

- *Laboratory test rig*
  Another useful tool would be a sealing test rig. This would also allow not only further research into the flow properties, but also into leakage and operational behaviour. The structure could be similar to the Oxford test rig presented in [20]. However, adaptions are suitable to widen the array of possible experiments. Some key points should be:

  - A power unit to reach engine representative speeds.
  - Flow field, leakage, pressure and temperature measurements. The pressure measurements should especially include the side plates of the leaf seals.
  - Radial movability of the rotor to make research into rotor excursions.
  - Axial movability for the use of a staged rotor design. This would make the variation of radial clearances for the same seal design easier.
  - Implements to allow for a variation of the upstream flow field (inlet swirl).
  - Interchangable seal retainer

  At the same time, a corresponding FE/CFD model of the test rig and the flow channels should be made to allow for an evaluation of the results.

- *Leaf seal as imperfect labyrinth seal*
  In cross section the leaf seal looks very similar to a straight labyrinth seal with to tips. The only difference is the leaf pack in-between. Therefore it might be possible to use approaches for non-ideal labyrinth seal calculations to investigate similarities and differences.

- *Boundaries of continuum mechanics*
  Due to the small interleaf gap widths, especially at the leaf tip, the question arises, if continuum mechanics is still applicable.

Bibliography

[1] Pekris, M. J.; Franceschini, G.; Owen, A. K.; Jones, T. V.; Gillespie, D. R. H.: Analytical Modeling and Experimental Validation of Heating at the Leaf Seal/Rotor Interface. In: ASME Journal of Engineering for Gas Turbines and Power. Vol. 139 (2017)

[2] Ortner, H.: Berechnung des Leckageverhaltens von Lamellendichtungen für Fluggasturbinen. Diplomarbeit, Technische Universität Wien, 2009

[3] Fico, V.; Pekris, M. J.; Barnes, C. J.; Jha, R. K.; Gillespie, D.: CFD and Thermal Analysis of Leaf Seals for Aero-Engine Application. In: Proceedings of ASME Turbo Expo 2016, GT2016-56735, 2016

[4] Deo, H. V.; Rao, A.; Gedam, H.: Compliant Plate Seals: Design and Performance Simulations. In: Proceedings of ASME Turbo Expo 2012, GT2012-69348, 2012

[5] Deo. H. V.: Compliant Plate Seals for Turbomachinery Applications. In: Proceedings of ASME International Mechanical Engineering Congress & Exposition, IMECE2011-64871, 2011

[6] Deo, H. V.: Compliant Plate Seals: Testing and Validation. In: Proceedings of ASME Turbo Expo 2012, GT2012-69356, 2012

[7] Neef, M.; Sürken, N.; Sulda, E.; Walkenhorst, J.: Design Features and Performance Details of Brush Seals for Turbine Applications. In: Proceedings of ASME Turbo Expo 2006, GT2006-90404, 2006

[8] Watanabe, E.; Nakano, T.; Tanaka, K.; Tsutsumi, M.; Tanaka, Y.; Ohyama, H.; Miyawaki, T.; Shinohara, T.: Development Of New High Efficiency Steam Turbine. In: Mitsubishi heavy Industries, Ltd. Technical Review. Vol. 40, No. 4 (2003), pp. 1-6

[9] Pelegrin-Garcia, J. D.; Gillespie, D. R. H.; Pekris, M. J.; Franceschini, G.; Ganin, L.: Experimental Characterization of Rotor Convective Heat Transfer Coefficients in the Vincinity of a Leaf Seal. In: ASME Journal of Engineering for Gas Turbines and Power. Vol. 139 (2017)

[10] Jahn, I. H. J.; Franceschini, G.; Owen, A. K.; Jones, T. V.; Gillespie, D. R. H.: Experimental Characterisation of the Stiffness and Leakage of a Prototype Leaf Seal for Turbine Applications. In: Proceedings of ASME Turbo Expo 2008, GT2008-51206, 2008

[11] Pekris, M. J.; Franceschini, G.; Jahn, I. H. J.; Gillespie, D. R. H.: Experimental Investigation of a Leaf Seal Prototype at Engine-Representative Speeds and Pressures. In: ASME Journal of Engineering for Gas Turbines and Power. Vol. 138 (2016)

[12] Grondahl, C. M.; Dudley, J. C.: Film Riding Leaf Seals for Improved Shaft Sealing. In: Proceedings of ASME Turbo Expo 2010, GT2010-23629, 2010

[13] Pekris, M. J.; Nasti, A.; Franceschini, G.; Jahn, I. H. J.: High Speed Characterization of a Prototype Leaf Seal on an Advanced Seal Test Facility. In: Proceedings of ASME Turbo Expo 2015, GT2015-43465, 2015

[14] Jahn, I. H. J.; Gillespie, G.; Cooper, P.: Hydrodynamic Air-Riding in Leaf Seals. In: Proceedings of ASME Turbo Expo 2013, GT2013-95585, 2013

[15] Franchescini, G.; Jones, T. V.; Gillespie, D. R. H.: Improved Unterstanding of Blow-Down in Filament Seals. In: Proceedings of ASME Turbo Expo 2008, GT2008-51197, 2008

[16] Jahn, I. H. J.; Franceschini, G.; Owen, A. K.; Jones, T. V.; Gillespie, D. R. H.: Improved Unterstanding of Negative Stiffness in Filament Seals. In: ASME Journal for Turbomachinery. Vol. 138 (2016)

[17] Franceschini, G.; Jahn, I. H. J.; Owen, A. K.; Jones, T. V.; Gillespie, D. R. H.: Improved Unterstanding of Negative Stiffness in Filament Seals. In: Proceedings of ASME Turbo Expo 2012, GT2012-68899, 2012

[18] Greitzer, E. M.; Tan, C. S.; Graf, M. B.: Internal Flow. Cambridge University Press, 2004

[19] Pröstler, S.: Modellierung und numerische Berechnung von Wellendichtungen in Bürstenbauart. Dissertation. Ruhr-Universität Bochum, 2005

[20] Jahn, I. H. J.: Negative Stiffness in Gas Turbine Leaf Seals. In: Proceedings of ASME Turbo Expo 2011, GT2011-46483, 2011

[21] Gross, D., Hauger, W., Schröder J., Wall, W.: Technische Mechanik 2. Springer Verlag, 2009

[22] Bohl, W., Elmendorf, W.: Technische Strömungslehre. Vogel Buchverlag, 2014

[23] Nakane, H.; Maekawa, A.; Akita, E.; Akagi, K.; Nakano, T.; Nishimoto, S,; Hashimoto, S.; Shinohara, T.; Uehara, H.: The Development of High-Performance Leaf Seals. In: ASME Journal of Engineering for Gas Turbines and Power. Vol. 129 (2004), pp. 342-350

[24] Hendricks, R. C.; Griffin, T. A.; Kline, T. R.; Csavina, K. R.; Pancholi, A.; Sood, D.: Relative Performance Comparison Between Baseline Labyrinth and Dual-Brush Compressor Discharge Seals in a T-700 Engine Test. NASA Technical Memorandum 106360, 1994

[25] Bischelmaier, G.: Simulation des Strömungsverhaltens in einer Lamellendichtung mittels porösem Medium. Diplomarbeit, Technische Universität Wien, 2011

[26] Wright, C.: United States Patent, No.: US 6,267,382 B1. Jul. 31, 2001

[27] Eck, B.: Ventilatoren. Springer Verlag, 2003

[28] Kluwick, A.: Vorlesungsskriptum Grundlagen der Strömungslehre, 1998

Appendix A

Results and Comparison of Pressure and Leakage - Further Figures

A.1 Comparison of Radial Velocities

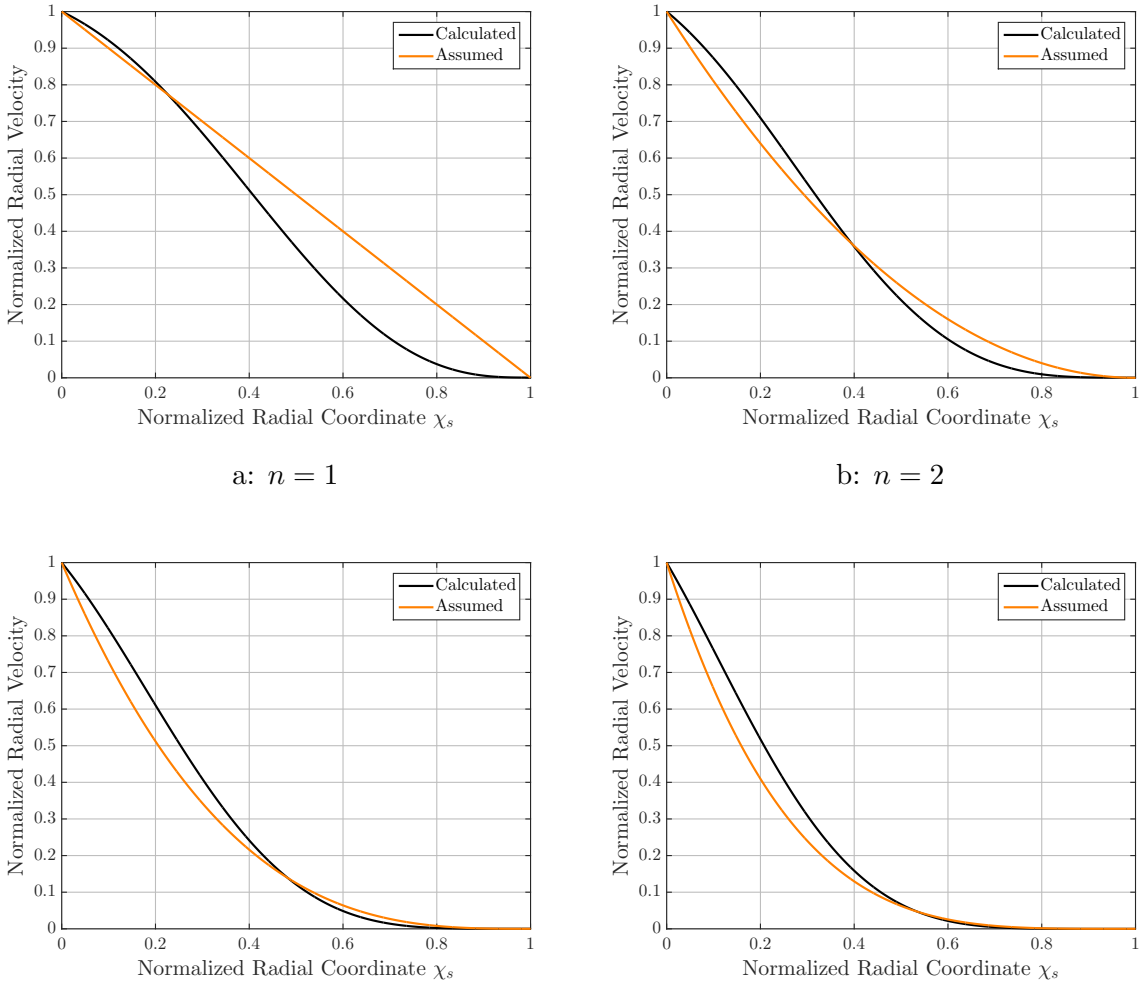

a: $n = 1$

b: $n = 2$

c: $n = 3$

d: $n = 4$

Figure A.1: Assumed and calculated normalized radial velocities for exponents $n = 1$ to 4

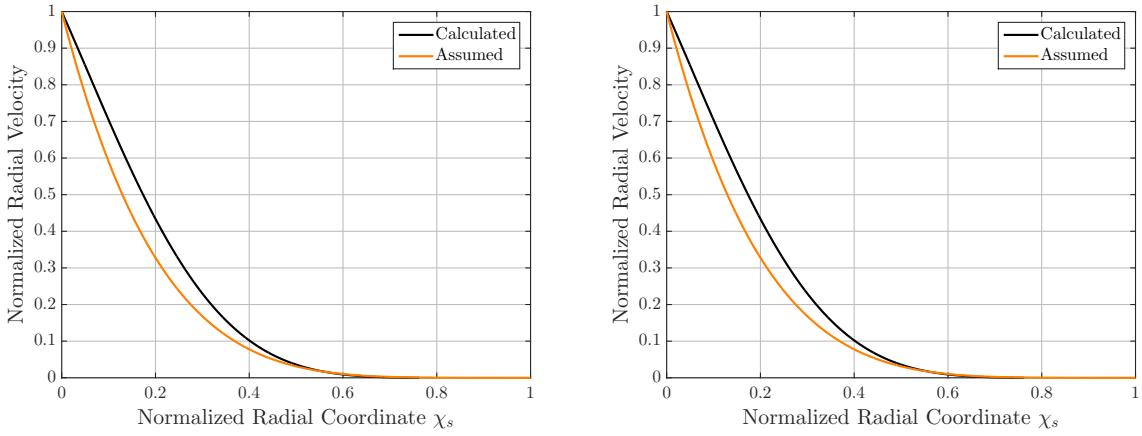

a: $n = 5$ b: $n = 6$

Figure A.2: Assumed and calculated normalized radial velocities for exponents $n = 5$ and 6

A.2 Comparison of Static Pressure Distributions

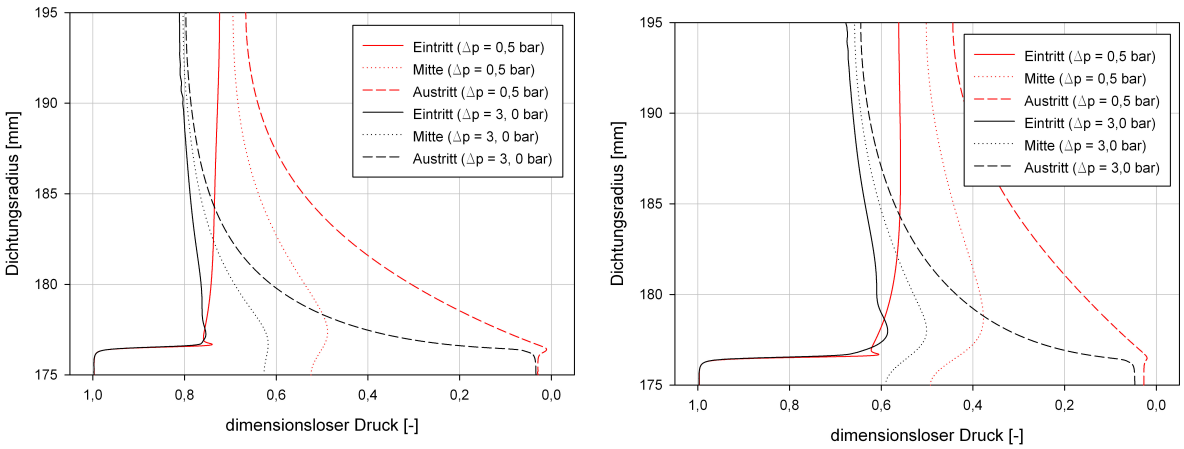

(a) Model 1 from [25] (b) Model 2 from [25]

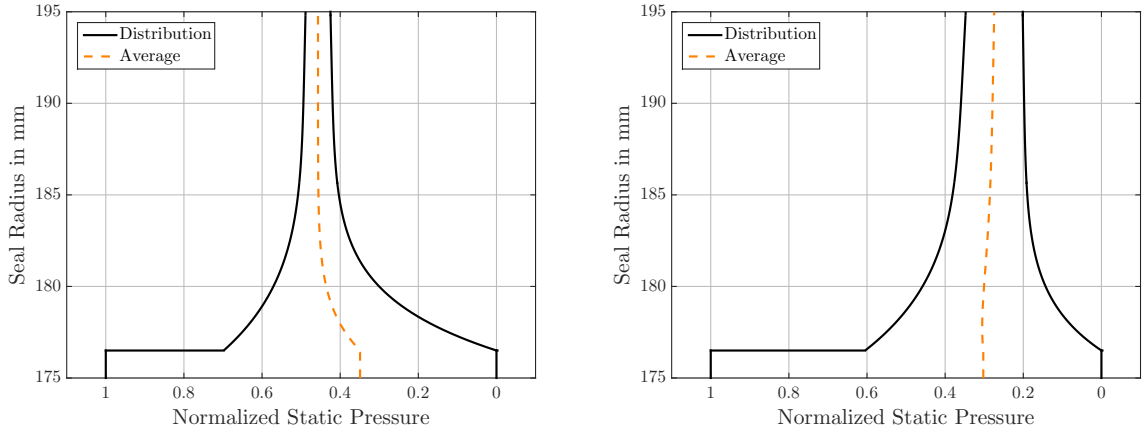

(c) Model 1, $n = 4$ and $f = 0.02$, $\Delta p = 0.5bar$ (d) Model 2, $n = 4$ and $f = 0.04$, $\Delta p = 0.5bar$

Figure A.3: Pressure distributions of Models 1-2

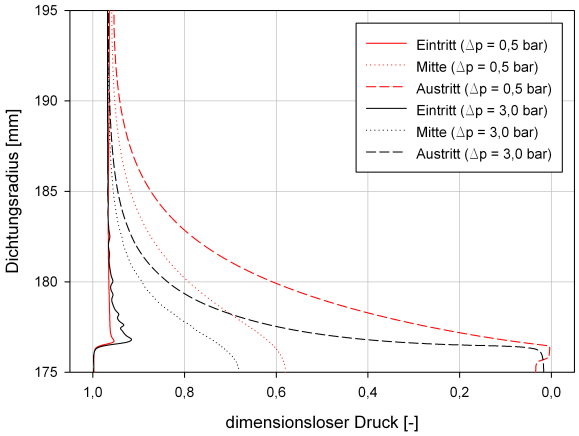

e: Model 3 from [25]

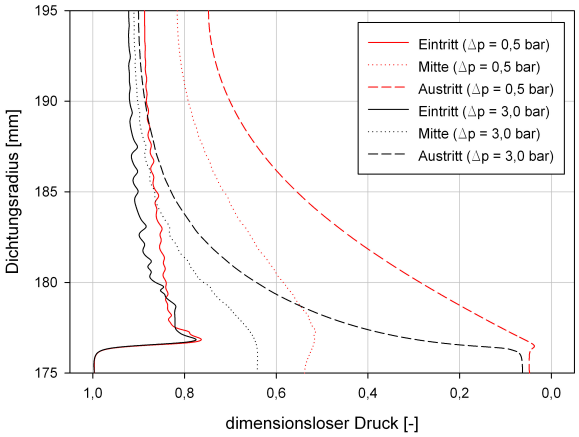

f: Model 4 from [25]

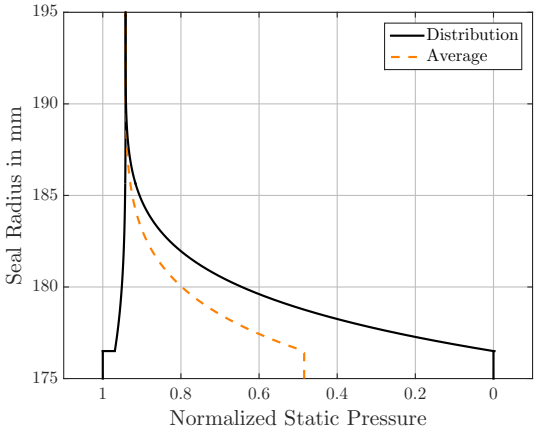

g: Model 3, $n = 4$ and $f = 0$, $\Delta p = 0.5bar$

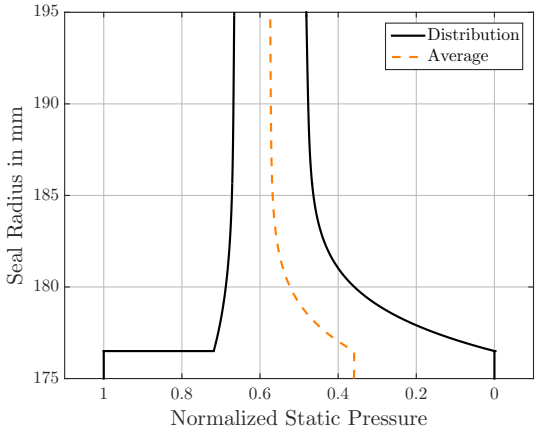

h: Model 4, $n = 4$ and $f = 0.03$, $\Delta p = 0.5bar$

Figure A.4: Pressure distributions of Models 3-4

A.3 Comparison of Radial Velocities for Seal Variations

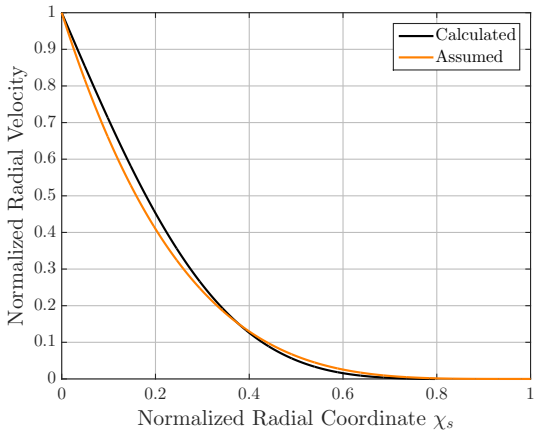

a: $n = 4,\ i = 0.5mm$

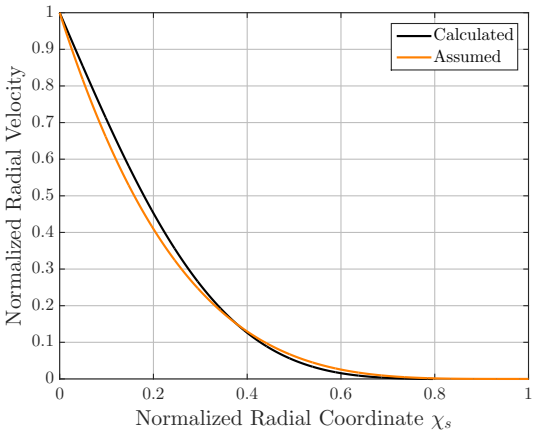

b: $n = 4,\ i = 2.5mm$

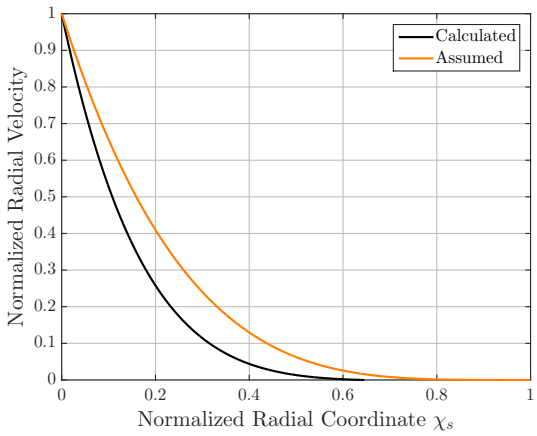

c: Constant interleaf gap

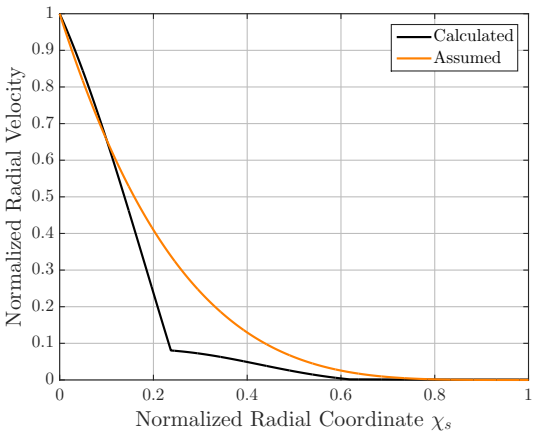

d: Saw tooth interleaf gap

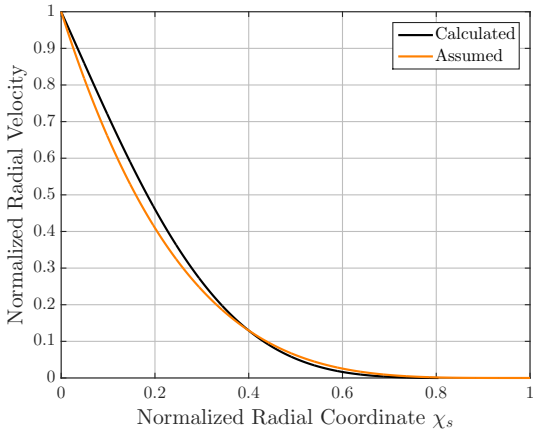

e: Model 3

Figure A.5: Comparison of radial velocities for seal variations